THE PACKING LANDSCAPES OF QUASI–ONE DIMENSIONAL HARD SPHERE SYSTEMS

A Thesis Submitted to the
College of Graduate Studies and Research
in Partial Fulfillment of the Requirements
for the degree of Doctor of Philosophy
in the Department of Chemistry
University of Saskatchewan
Saskatoon

By
Mahdi Zaeifi Yamchi

Permission to Use

In presenting this thesis in partial fulfilment of the requirements for a Postgraduate degree from the University of Saskatchewan, I agree that the Libraries of this University may make it freely available for inspection. I further agree that permission for copying of this thesis in any manner, in whole or in part, for scholarly purposes may be granted by the professor or professors who supervised my thesis work or, in their absence, by the Head of the Department or the Dean of the College in which my thesis work was done. It is understood that any copying or publication or use of this thesis or parts thereof for financial gain shall not be allowed without my written permission. It is also understood that due recognition shall be given to me and to the University of Saskatchewan in any scholarly use which may be made of any material in my thesis.

Requests for permission to copy or to make other use of material in this thesis in whole or part should be addressed to:

Head of the Department of Chemistry
165 Thorvaldson Building
110 Science Place
University of Saskatchewan
Saskatoon, Saskatchewan
Canada
S7N 5C9

Abstract

Packing Landscapes of Constrained Hard Sphere Fluids
By
Mahdi Zaeifi Yamchi

When a liquid is cooled below its equilibrium freezing temperature, it becomes supercooled and the molecular motions slow down until the system becomes kinetically arrested, forming a glass, at the glass transition temperature. These amorphous materials have the mechanical properties of a solid while retaining the structural properties of a liquid, but do not exhibit the usual features of a thermodynamic phase transition. As such, they present a number of important challenges to our understanding of the dynamics and thermodynamics of condensed phases. For example, supercooled liquids are classified on the basis of the temperature dependence of their transport properties and structural relaxations times. Strong liquids display an Arrhenius behavior, with the logarithm of their viscosity growing linearly with inverse temperature. Fragile liquids behave in a super–Arrhenius manner, where the viscosity appears to diverge at temperatures above absolute zero, suggesting the possibility of an underlying thermodynamic origin to the glass transition. Some complex, network forming liquids, such as water and silica have also been shown to have a dynamical crossover from fragile to strong liquid behavior as the temperature is decreased.

The potential energy landscape paradigm, combined with inherent structure formalism, provide a framework for connecting the way particles pack together with the thermodynamics and dynamics of the liquid and glassy phases. However, the complexity of this multi–dimensional surface makes it difficult to fully characterize, and find rigorous relationships between the nature of particle packings and glass forming properties have not been established.

The goal of this thesis is to study some of the general features of the glass transition and find the connection between the dynamics and the thermodynamics of glass forming liquids. To this end, the packing landscapes of quasi–one–dimensional hard discs and hard spheres are studied.

A two dimensional system of hard discs with diameter σ, confined between two hard walls (lines) of length L, separated by a distance $1 < H_d/\sigma < 1 + \sqrt{3/4}$, is studied by using the

Transfer Matrix (TM) method and Molecular Dynamics (MD) simulations. The complete packing landscape is characterized in terms of the density distribution of inherent structures and the number of local defect states. It is shown that this model exhibits a dynamic fragile–strong liquid crossover at the maximum in the constant pressure heat capacity (C_p) for the system, similar to that observed in anomalous network forming liquids such as water and silica. Furthermore, we find that rescaling the relaxation times of systems with different channel widths by the relaxation time at the C_p maximum causes all the data to collapse on a single master curve. The C_p maximum occurs at a critical value of the defect concentration. At high defect concentrations, where the defects interact, the fluid is fragile. When the defect concentration is low, relaxation appears to occur through the hopping of isolated defects, leading to Arrhenius dynamics. This suggests the thermodynamics associated with the C_p maximum is intimately related to the dynamic crossover.

A system of three dimensional hard spheres confined in a narrow channel was used to study the effect of a more complicated landscape on the dynamics of the system. For this system, the thermodynamic and dynamic properties of the system were studied for two different channel diameters, the $1 < H_d/\sigma < 1 + \sqrt{3/4}$ case, which only allows first neighbors contact for the spheres and, $1 + \sqrt{3/4} < H_d/\sigma < 1.98$, which allows second neighbor contacts to exist. For the first case, the TM method was implemented to obtain the thermodynamic properties and MD simulation was used to measure the dynamics. For the case that second neighbors contact is allowed $1 + \sqrt{3/4} < H_d/\sigma < 1.98$. The thermodynamic and dynamic properties were obtained using MD simulations. In this channel diameter range, the system creates chiral helical jammed packings and defect states appear where sections of helices with different local chiralities come into contact. The equation of state (EOS) shows the presence of two heat capacity maximum. The high density C_p maximum is linked to fragile strong crossover. Finite size scaling analysis shows that the low density C_p maximum is related to an orientational order transition stabilized by the presence of the defects. This type of transition has been shown to exist in bulk two dimensional systems but this work is the first study that provides strong evidence of the existence of this transition in a quasi–one dimensional system in a system with short–range interactions.

ACKNOWLEDGEMENTS

I am grateful to my advisor Richard Bowles for accepting me in his lab and introducing me to condensed matter physics and for his guidance during my time at U of S. I thank him for fostering an environment of hard work and excellence in his group. His ideas and vision have helped me shape my own philosophy in research, which is an invaluable asset for my future academic career. I could not have asked for a better advisor and mentor for my Ph.D study.

I would also like to thank my committee members from whom I have learned a lot. This dissertation would not have been possible without their thoughtful suggestions and comments. I would also thank the other faculty members that I have had the pleasure of interacting with.

Special thanks to S.S. Ashwin for his interesting conversations and mentoring, and for allowing me to collaborate on a fascinating project. It was such a great opportunity for me to work with him.

I thank my fellow labmates, Levent Inci, Cletus Asuquo, Surajith Wanasundara, Wikai Qi, Sheida Ahmadi and Louis Poon for all that they have taught me throughout our time working together. I thank all of the Bowles group members, past and present, for their friendships, many of which will last a lifetime.

Most of all, I thank my parents. Words can not express how grateful I am to you for all of the sacrifices you have done on my behalf. It is easy to reach for your goals when you know you will always have someone in your corner. Dear mom, although death has separated us physically, faith and love have bound us eternally. Your love have shaped my character, molded my spirit and touched my heart. I also thank my siblings for their admiration. It is such a great privilege to have them by my side.

For my parents.

Contents

Permission to Use i

Abstract ii

Acknowledgements iv

Contents vi

List of Figures ix

List of Abbreviations xiv

List of Symbols xv

1 Background 1
- 1.1 Introduction 1
- 1.2 What is a Glass? 2
  - 1.2.1 Dynamics 2
  - 1.2.2 Thermodynamics 6
  - 1.2.3 Structure 8
- 1.3 Theories of the Glass Transition 8
  - 1.3.1 The Potential Energy Landscape 9
  - 1.3.2 Adam–Gibbs Theory 11
  - 1.3.3 Mode–Coupling Theory 12
  - 1.3.4 Random First Order Transition Theory 13
  - 1.3.5 Kinetically Constrained Models and Dynamic Facilitation 14
- 1.4 Hard Sphere Systems 15
- 1.5 Particle Packing and Jamming Phase Transition 17
  - 1.5.1 Jamming Phase Diagram 19
  - 1.5.2 Replica Mean Field Theory 20
- 1.6 Fragile–Strong Crossover 21
- 1.7 Thesis Overview 22

2 A Binary Mixture of Non-Additive One-dimensional Hard Rods 25
- 2.1 Overview 25
- 2.2 Introduction 25
- 2.3 Model Description 26
- 2.4 Distribution of Glasses 28
- 2.5 Heat Capacity 31
- 2.6 Inherent Structure Pressure 31
- 2.7 Jamming Phase Diagram 32
- 2.8 Concluding Remarks 34

3 2d Hard Discs in Confined Geometry 35

3.1 Overview . . . 35
3.2 Introduction . . . 35
3.3 Model Description . . . 36
3.4 Transfer Matrix Method . . . 37
  3.4.1 The Inherent Structure Landscape (ISL) . . . 37
3.5 Thermodynamics of the Equilibrium Liquids . . . 41
  3.5.1 Transfer Matrix Method . . . 41
  3.5.2 Mapping Configurations to Inherent Structures . . . 42
  3.5.3 Defect–Defect Interactions . . . 45
  3.5.4 Heat Capacity . . . 48
  3.5.5 Inherent Structure Pressure . . . 48
3.6 Molecular Dynamics Simulations . . . 49
  3.6.1 Exploring the Packing Landscape . . . 50
  3.6.2 Free Volume Equation of State . . . 53
  3.6.3 Relaxation Times . . . 54
  3.6.4 Adam–Gibbs Relation . . . 60
3.7 Discussion . . . 61
3.8 Jamming Phase Diagram . . . 64
3.9 Conclusion . . . 64

4 3d Hard Spheres in Confined Geometry **67**
4.1 Overview . . . 67
4.2 Introduction . . . 68
  4.2.1 Model Description . . . 70
4.3 $1.0 < H_d/\sigma < 1 + \sqrt{3/4}$ . . . 70
  4.3.1 Thermodynamics of the Equilibrium Liquids . . . 71
  4.3.2 Simulation Methods . . . 73
  4.3.3 Relaxation Time . . . 74
4.4 $1 + \sqrt{3/4} < H_d/\sigma < 1.98$ . . . 75
  4.4.1 Inherent Structure Landscape Description . . . 76
  4.4.2 The Equilibrium Fluid . . . 89
  4.4.3 Relaxation Time . . . 91
  4.4.4 Orientational Order Parameter . . . 94
4.5 Discussion . . . 98
4.6 Conclusion . . . 101

5 Diffusion in confined geometry **102**
5.1 Overview . . . 102
5.2 Introduction . . . 102
5.3 Simulation Methods . . . 104
5.4 Results and Discussion . . . 104
  5.4.1 Transport in One Dimensional Systems . . . 104
  5.4.2 Excess Entropy Scaling . . . 107
5.5 Conclusion . . . 108

6 Conclusions and Outlook **110**
6.1 Discussion . . . 110

6.2 Conclusions . . . 114
    6.2.1 Inherent Structure Landscape . . . 114
    6.2.2 Fragile–Strong Crossover . . . 115
    6.2.3 Orientational Order Phase Transition . . . 115
6.3 Future Outlook . . . 116
    6.3.1 Inherent Structure Landscape in Wider Channels . . . 116
    6.3.2 Theoretical Studies in Confined Geometry . . . 117

References **119**

List of Figures

1.1 Cartoon representation of a) crystal and b) glassy structures. 1

1.2 Typical relaxation behavior of intermediate scattering function for normal liquids and supercooled liquids. Single exponential decay in case of normal liquids (red line) and supercooled liquids show two steps relaxation (blue line) [10]. . 4

1.3 Reprinted with permission from Nature Publishing group from [4]. T_g scaled Arrhenius representation of liquid viscosities showing Angell's strong–fragile pattern. 5

1.4 Temperature dependence of a liquids volume V or enthalpy H at constant pressure. 8

1.5 Reprinted with permission from Nature Publishing group from [4]. Schematic illustration for an energy landscape. The x$-$*axis* represents all configurational coordinates. 10

1.6 The pressure of hard spheres versus density near the transition region adopted from [62]. 15

1.7 Reprinted with permission from Nature Publishing group from [89]. Jamming phase diagrams proposed by Liu and Nagel [89] (a), and diagram obtained for attractive colloidal systems [90] (b). 19

2.1 Cartoon representation of the non–additive hard rod system. Top graph: positive non–additivity depicted using left–tilted rhombi. The small species (A) interact with σ_{AA} and large species (B) interact with length σ_{BB} with their own type and the length σ_{AB} is the interaction length between type A and B. Bottom: A similar situation for negative non–additivity illustrated using wedges (adapted from [135]). 27

2.2 Most dense ($\phi_{J\,\max}$ top) and least dense ($\phi_{J\,\min}$ bottom) structures for the binary hard rods systems with positive non–additivity. 28

2.3 The distribution of glasses with jammed density ϕ_J for different values of the non–additivity parameter, Δ. 29

2.4 The jammed state densities that the equilibrium fluid samples as a function of density, for different values of the non–additivity parameter, Δ. 29

2.5 Distribution of inherent structures (a) and how the equilibrium fluid samples the inherent structures (b) for the system with $\Delta = 1$. 30

2.6 S_c as a function of ϕ for the systems with different values of non–additivity . . 30

2.7 EOS for different non–additivity parameter as a function of density(ϕ). 32

2.8 C_P/Nk_{B} for different non–additivity parameter as a function of $(\phi PL/Nk_{\mathrm{B}}T)^{-1}$. 32

2.9 Inherent structure pressure as function of density for different values of non–additivity, Δ. 33

2.10 Vibrational pressure as function of density for different values of non–additivity, Δ. 33

2.11 The jamming phase diagram for the non–additive binary mixture of hard rods model, including $\phi_{J\,\max}$, $\phi_{J\,\min}$, and ϕ^*_J, as a function of Δ. 33

3.1 Local packing arrangements of discs. Dashed lines connect the centers of neighboring discs in contact, and the numbers identify different “bonds”. Bonds 1 and 3 are the locally most dense states. Bonds 2 and 4 represent the defect states. The $-4-4-$ arrangement results in an unjammed particle (dash filled). 38
3.2 S_J/Nk_{B} versus ϕ_J for $H_d/\sigma = 1+\sqrt{3/4}$. The thermodynamically accessible packings have occupied volume fractions between $\phi_J^* = 0.659$ (green square) and the most dense jammed state, $\phi_{J\,\mathrm{max}} = 0.842$, (blue square). The thermodynamically inaccessible exist below ϕ_J^* and the least dense state $\phi_{J\,\mathrm{min}} = 0.561$ (red square). 40
3.3 Top: most dense ($\phi_{J\,\mathrm{max}}$) Bottom: least dense ($\phi_{J\,\mathrm{min}}$) structures for the system. 40
3.4 The jamming phase diagram showing $\phi_{J\,\mathrm{max}}$, $\phi_{J\,\mathrm{min}}$ and ϕ_J^* as a function of H_d/σ. The ϕ of the maxima for the inherent structure pressure, P_{IS}, and the heat capacity, C_p, are included for comparison. The green area identifies the accessible jammed packings and the yellow area represents the inaccessible jammed packings. 41
3.5 The EOS for different values of channel diameters H_d/σ. 43
3.6 Analytical quench connecting equilibrium fluid configurations of discs i, m, n, j to the most dense (1, 3) and least dense (2, 4) local packing arrangements. Equilibrium configuration of four discs are initially mapped to a tangent disc configuration by compression in the x axis. The product of the kernel $K(y_i, y_j)$ and the dot product of vectors (Eq 3.16) maps the central discs to their jammed configuration. See text for more details. 44
3.7 The fraction of defect bonds in the inherent structures sampled by equilibrium fluid at ϕ. The solid line represents the transfer matrix results and the open circles were obtained from simulation (see Section 3.6.1) 46
3.8 The fraction of defect bonds in the inherent structures sampled by equilibrium fluid at ϕ for different values of channel diameters H_d/σ. 46
3.9 The configurational entropy of the equilibrium fluid for different values of channel diameters H_d/σ. 46
3.10 η as a function of ϕ. The solid line represents data calculated using the transfer matrix method. The dashed line is the linear extrapolation. 48
3.11 C_p/Nk_{B} as a function of $(\phi PV/Nk_{\mathrm{B}}T)^{-1}$. 49
3.12 C_p/Nk_{B} as a function of defect fraction θ. 49
3.13 The vibrational pressure of the system as a function of packing fraction. . . . 50
3.14 The inherent structure pressure of the system as a function of packing fraction. 50
3.15 EOS for $H/\sigma = 1+\sqrt{3/4}$. EOS for granular ensemble: $\beta P_L h_0$ as a function of ϕ_J (blue dot–dashed line). EOS for equilibrium thermal fluid: $\beta P_L h_0$ as a function of ϕ (black solid line). ϕ_J of basins sampled by equilibrium fluid (green dashed line). EOS for fluid compressed using LS method with different $\partial\sigma/\partial t$ (dotted lines). 51
3.16 The difference between the equilibrium EOS and the non-equilibrium EOS as a function of ϕ, with $H_d/\sigma = 1+\sqrt{3/4}$, for different compression rates. . . . 51
3.17 ϕ_J as a function of $\partial\sigma/\partial t$ 52
3.18 The transition state for motion of a defect: a disc in a stable defect state (a) moves through a transition state (b) as it hops to another stable state (c) (adapted from [154]). 53

3.19 The Free Volume EOS for the systems of jammed states. 54
3.20 Structure factor $S(\mathbf{k})$ for all ϕ investigated with $H_d/\sigma = 1+\sqrt{3/4}$. For clarity the individual curves have been displaced vertically by 1 with increasing ϕ. The red curve highlights the data for $\phi = 0.534$, corresponding to the ϕ of the C_p maximum. 55
3.21 The time dependance of the self intermediate structure factor,$F(\mathbf{k}_{\max}, t)$ for a system with $H_d/\sigma = 1+\sqrt{3/4}$, over a range of ϕ. 56
3.22 Arrhenius plot for the relaxation times obtained from self intermediate function for different values of H_d/σ. 56
3.23 The time dependance of the bond survival probability $R(t)$ for a system with $H_d/\sigma = 1+\sqrt{3/4}$, over a range of ϕ. 57
3.24 Arrhenius plot for the relaxation time for $H_d/\sigma = 1+\sqrt{3/4}$. The dashed and dashed–dotted lines represent fits to the data in the fragile region of the parabolic and VFT equations, respectively. The solid line is the Arrhenius fit to the strong fluid region. 57
3.25 The derivation of the logarithmic relaxation time τ is plotted against $1/T$ for $H_d/\sigma = 1+\sqrt{3/4}$. 58
3.26 Structural relaxations time for different H_d/σ as a function of $\phi PV/Nk_\mathrm{B}T$. . . 59
3.27 Structural relaxations time for different H_d/σ rescaled by the "glass transition" time and temperature (see text for definition). 59
3.28 Structural relaxations time for different H_d/σ rescaled by the time and temperature of the C_p maximum 59
3.29 Structural relaxations times for different H_d/σ as a function of the defect concentration relative to the defect concentration in the ideal gas, θ_∞.The solid black lines are the Arrhenius fit. 60
3.30 Structural relaxations times for different H_d/σ rescaled by the time and defect concentration of the C_p maximum as a function of the defect concentration relative to the defect concentration in the ideal gas, θ_∞. The solid black line is the Arrhenius fit. 60
3.31 Adam-Gibbs plot for $H_d/\sigma = 1+\sqrt{3/4}$. 61
3.32 Distribution of inherent structures (top) and how the equilibrium fluid samples the inherent structures (bottom). 65

4.1 Schematic of spheres inside a narrow channel. x and y define the transverse directions and z describes the longitudinal direction along the channel axis. The central axis is taken as $x = y = 0$. 70
4.2 Single jammed state for $H_d/\sigma < 1+\sqrt{3/4}$ ($H_d/\sigma = 1.80$). Two different colors are used to show the nature of the packings. 71
4.3 EOS for different values of channel widths as a function of density, ϕ. 73
4.4 C_p/Nk_B as a function of $(\phi PV/Nk_\mathrm{B}T)^{-1}$ for different values of channel widths. 73
4.5 Structure factor $S(\mathbf{k})$ for all densities investigated. For clarity the individual curves have been displaced vertically by 1 with increasing ϕ. The red curve highlights the data for $\phi = 0.234$, corresponding to the ϕ of the C_p maximum. 75
4.6 Time dependance of self–intermediate scattering function for $H_d = 1.80$ at different densities. 75

4.7 Arrhenius plot for the relaxation times obtained from self–intermediate scattering function for $H_d = 1.80$. 76
4.8 Two different enantiomers created because of the chiral nature of the structures. Two different colors are used to show the nature of the packings. 77
4.9 3d and 2d illustration of three particles in contact with each other inside a cylinder. 78
4.10 Contour plot of the solutions for eq. 4.19 as a function of α_1 and α_2 for the case of $H_d/\sigma = 1.95$. 79
4.11 The vertical separations between particles (Z_1, Z_2 and Z_d) as a function of α_1. 80
4.12 The length per particle for the jammed configurations as a function of α_1. . . 80
4.13 2d illustration of four particles used to describe the geometry of a defect. . . . 81
4.14 Perfect packing tile (a) and defect type tile (b). 81
4.15 The defect type structures will be created when two jammed states with different local chiralities come into contact. 81
4.16 Horizontal particle separation in the defect state, Z_d at different values of angular separations α_1. 83
4.17 Contour plot of ϕ_J as a function of α_1 and θ for the case of $H_d/\sigma = 1.95$. . . . 84
4.18 ϕ_J for the ordered defect configurations as a function of defect fraction, θ. . . 84
4.19 Distribution of jammed packings as a function of defect fraction. 85
4.20 Configuration with $\theta = 0$ (a) and configuration with $\theta = 0.5$. 85
4.21 The Free Volume EOS for the systems of jammed states. 86
4.22 Length analysis for Z_1, Z_2 and Z_d as a function of number of particles in the gaps between defects, N_{PDG}. The solid lines are the results from geometrical approach, big symbols are the values from simulation of ordered jammed configurations and small symbols show the values for amorphous packings from simulations. 87
4.23 Jammed density of the system at different compression rates (top figure) and the defect fraction of the jammed states at different compression rates (bottom figure). The dashed lines are guides to the eye. 88
4.24 $PV/Nk_{\mathrm{B}}T$ versus ϕ for $H_d/\sigma = 1.95$. The dashed line is a guide to the eye. . . 90
4.25 C_p/Nk_{B} versus ϕ for $H_d/\sigma = 1.95$. The dashed line is a guide to the eye. . . . 90
4.26 Fraction of defect states, θ, as a function of density, ϕ. 91
4.27 η as a function of ϕ. The solid line represents data measured from MD simulation. The dashed line is the linear extrapolation. 91
4.28 Representative trajectories in the system. The vertical axis is space measured in particle number, the horizontal one time. The six trajectories are for very low density, $\phi = 0.01$, before first heat capacity maximum, $\phi = 0.24$, after first heat capacity maximum, $\phi = 0.25$, before the second heat capacity maximum, $\phi = 0.37$, after the second heat capacity maximum, $\phi = 0.38$ and at glassy configuration, $\phi = 0.39$. Configurations with R local chirality are red, and configurations with S local chirality are blue and the defects are black. 92
4.29 Structure factor $S(\mathbf{k})$ for all densities investigated. For clarity the individual curves have been displaced vertically by 1. 94
4.30 Arrhenius plot for the relaxation times obtained from self intermediate function for $H_d/\sigma = 1.95$. 94

4.31 Arrhenius plot for the relaxation times for $H_d = 1.95$. The dashed lines represent parabolic equation fits to the data in the fragile region. The solid line is the Arrhenius fit to the strong fluid region. 95
4.32 The derivation of the logarithmic relaxation time τ is plotted against $1/T$ for $H_d = 1.95$. 95
4.33 Orientational order parameter ψ_6 as a function of density at different system sizes. 96
4.34 Orientational correlation function $g_6(z)$ as a function of $\mathbf{r}$ at different densities. 96
4.35 Orientational order susceptibility χ_6 as a function of density at different system sizes. 97
4.36 Finite size scaling of χ_{max} as a function of different system sizes. 97
4.37 Density of the peak in the orientational order susceptibility, χ_6, as function of system size. 98
4.38 Linear scaling of the position of the peak in the orientational order susceptibility. 98
4.39 Jammed densities obtained for different values of channel diameters using deferent compression rates. The solid line shows the analytical results for $\phi_{J\max}$. The values of C_p maxima at different values of channel diameters are also included (refer to text for more details). 100

5.1 The MSD along the direction of the pore axis, as a function of t for $H_d = 1.1$ at different densities. The short line segments have slopes as indicated and are included as a guide to the eye. 105
5.2 Slopes for MSD lines obtained using central difference method as a function of t for $H_d = 1.1$ at different densities. 105
5.3 Diffusivity, D, vs. occupied volume fraction, ϕ, for various values of channel width, symbols are simulation data. 106
5.4 Rescaled diffusivity data using Eq. 5.3 for different values of channel diameter. 106
5.5 Effective diameter in a system of: purely 1d system $\sigma_{\text{eff}} = \sigma_i$ (a), system with $H_d/\sigma = 1.8$ in low density and a broad distribution of diameters (b), and system with $H_d/\sigma = 1.8$ at high density with narrow distribution of diameter. 107
5.6 Scaled self–diffusion coefficient data using modified Jepson equation (eq. 5.8) for various values of channel widths. 108
5.7 Scaled self–diffusion coefficient data versus negative excess entropy calculated from integration over equilibrium liquid EOS for various values of channel widths.109
5.8 Scaled self–diffusion coefficient data versus negative excess entropy calculated using eq. 5.11 for various values of channel widths. 109

6.1 EOS for channel with $H_d/\sigma = 2.4$ as a function of density. 117
6.2 C_p for channel with $H_d/\sigma = 2.4$ as a function of density. 117

List of Abbreviations

AG	Adam–Gibbs
BLJM	Binary Lennard–Jones Mixture
CNT	Carbon Nano Tube
CRR	Cooperatively Rearranging Regions
d	Dimension
EDMD	Event–Driven Molecular Dynamics
EOS	Equation of State
FA	Fredrickson–Andersen
FCC	Face–Centered–Cubic
FD	Facilitated Dynamics
FS	Fragile–Strong
GCP	Glass Close Packed
HCP	Hexagonal–Closed–Packed
IS	Inherent Structure
ISL	Inherent Structure Landscape
ISF	Intermediate Scattering Function
JPD	Jamming Phase Diagram
HD	Hard Sphere
KA	Kob–Andersen
KCM	Kinetically Constrained Model
KTHNY	Kosterlitz, Thouless, Halperin, Nelson and Young
LS	Lubachevsky–Stillinger
MC	Monte Carlo
MCT	Mode Coupling Theory
MD	Molecular Dynamic
MSD	Mean Squared Displacement
PEL	Potential Energy Landscape
RCP	Random Close Packing
RFOT	Random First Order Theory
RMFT	Replica Mean Field Theory
RTN	Random Tetrahedral Network
SF	Structure Factor
SFD	Single–File Diffusion
TMM	Transfer Matrix Method
VFT	Vogel–Fulcher–Tammann
WHAM	Weighted Histogram Analysis Method

List of Symbols

T_m	Melting temperature
T_g	Glass transition temperature
$S\left(\mathbf{k}\right)$	Structure factor
N	Total number of particles
$\rho_{\mathbf{k}}$	Probability density
$\mathbf{k}$	Vector $\mathbf{k}$
$\mathbf{r}$	Position of particle
L	Length
$G\left(\mathbf{r},t\right)$	Van Hove function
$F\left(\mathbf{k},t\right)$	Intermediate scattering function
t	Time
τ	Relaxation time
k_B	Boltzmann's constant
T	Temperature
T_{VFT}	VFT divergence temperature
J	Energy parameter
$T_{\circ}$	Onset temperature
$T_{\times}$	Crossover temperature
γ	Power law exponent
$\Delta_c S$	Excess entropy
$\Delta_c C_p$	Relative heat capacity of supercooled liquid or glass
T_K	Kauzmann temperature
Z	Partition function of the system
Λ	de Broglie wavelength
U	Total energy
Q	Partition function of the basins
V	Volume
P	Pressure
e_{IS}	Energy of basins
$f_{\mathbf{basin}}$	Average basin free energy
Ω	Number of basins
S_c	Configurational entropy
T_{MCT}	MCT critical temperature
ϕ_{MCT}	MCT critical density
T_c	Critical temperature
ξ	Mosaic characteristic size
F	Free energy
d	Dimensionality
Υ	Surface tension
$H\left[\{n_i\}\right]$	Hamiltonian
J	Energy scale
σ	Diameter of particles
ϕ	Occupied volume

ϕ_J	Density of jammed structure
H_d	diameter of channel
ϕ_K	Kauzmann density
ϕ_d	Density of first appearance of glassy state
ϕ_{th}	Density of inherent structures that ϕ_d maps
ϕ_{GCP}	Density of glass close packed
ϕ_J^*	Density of the inherent structure that ideal gas samples
τ_{inter}	Inter–basin relaxation
τ_{intra}	Intra–basin relaxation
C_p	Isobaric heat capacity
N_A	Number of particles type A
N_B	Number of particles type B
x_A	Mole fraction of particles type A
x_B	Mole fraction of particles type B
x_{AB}	Mole fraction of AB interaction
σ_{AA}	Particles type A interaction length
σ_{BB}	Particles type B interaction length
σ_{AB}	Particles type A and B interaction length
Δ	Non–additivity parameter
$\phi_{J\,\min}$	Density of least dense jammed state
$\phi_{J\,\max}$	Density of most dense jammed state
S_J	Entropy of jammed states
H	Enthalpy
P_{IS}	Inherent structure pressure
P_{vib}	Vibrational pressure
h_0	Reduced channel diameter
l	Bond length
P_L	Longitudinal pressure
$\Delta\left(N,P,T\right)$	Isothermal–isobaric ensemble partition function
λ	Largest eigenvalue
θ	Defect mole fraction
K	Kernal
δ	Mesh size
g	Gibbs free energy
$\overrightarrow{\Delta}$	Triangle area vector
M	Number of defects
η	Saddle index
m	Mass
$F_s\left(\mathbf{k},t\right)$	Self part of intermediate scattering function
τ	Relaxation time
m_f	Fragility parameter
$T_{\max}$	Temperature of the C_p maximum
ω_i	Biased potential
K	Spring constant
$\alpha_i^{\mathbf{ref}}$	Reference torsion angle
a	Horizontal separation between particle i and $i+1$ in a helix

b	Horizontal separation between particle $i+1$ and $i+2$ in a helix
c	Horizontal separation between particle i and $i+2$ in a helix
Z_1	Vertical length between particle i and $i+1$ in a helix
Z_2	Vertical length between particle $i+1$ and $i+2$ in a helix
Z_d	Vertical length between particle i and $i+1$ in a defect
α_1	Angular separation between particle i and $i+1$ in a helix
α_2	Angular separation between particle i and $i+2$ in a helix
α_3	Angular separation between particle $i+1$ and $i+2$ in a helix
$N_{\mathbf{PDG}}$	Number of particles in the defects gap
ψ_6	Orientational bond order
g_6	Correlation function of orientational order
χ_6	Bond orientational order susceptibility
$\chi_6\left(\infty\right)$	χ_6 in the thermodynamics limit
$\chi_6\left(L\right)$	χ_6 for a systems size L
$\chi_{6(\max)}$	Bond orientational order susceptibility's maximum hight
z	Correlation length critical exponent
$\phi_c\left(L\right)$	Critical density at subsystem size L
$\phi_c\left(\infty\right)$	Critical density at thermodynamics limit
D	Diffusion coefficient
F	Mobility factor
D^*	Normalized diffusion coefficient
$\Gamma_{\mathbf{E}}$	Effective Enskog inter–particle frequency
$\phi_{\mathbf{e}ff}$	Effective occupied volume
ρ	Number density
$D_{\mathbf{R}}$	Rosenfeld diffusion coefficient
$D_{\mathbf{D}}$	Dzugutov diffusion coefficient

Chapter 1

Background

1.1 Introduction

A glass (or vitreous solid) is defined as an amorphous solid (Fig. 1.1) formed by quenching the liquid very quickly [1]. Today, the glassy state plays a key role in both nature and technology. For example, some insects employ glassy materials as protection against extreme cold or dry conditions [2], while the food industry uses the glassy state to stabilize fragile biochemical products [2]. Window glass, optical fibers, most engineered plastics and silicon are the best known examples of engineered amorphous solids [3]. However, despite the extensive use of glasses and glass technology, these materials are not well understood from a fundamental perspective and they present a number of important challenges to our understanding of the dynamics and thermodynamics of condensed phases.

This chapter is organized as follows: Section 1.2 describes the glass in terms of dynamics, thermodynamics and structure. Section 1.3 gives a brief introduction about the theories introduced to study the glass transition. Section 1.4 focuses on hard sphere systems and

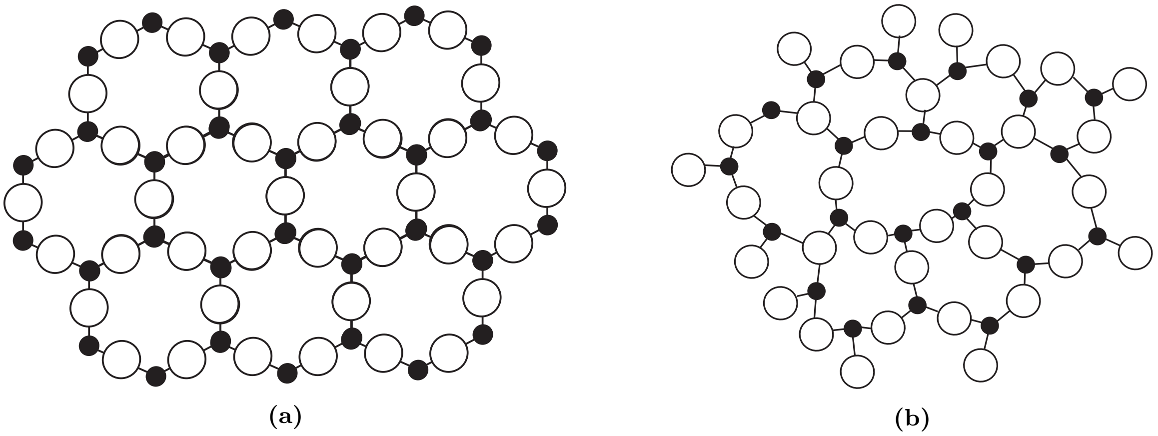
(a) (b)

Figure 1.1: Cartoon representation of a) crystal and b) glassy structures.

describes the phase diagram associated with them. Section 1.5 briefly introduces the particle packing in three dimensions and summarizes the jamming in the context of more general terms using jamming phase diagram. Section 1.6 explains the fragile–strong crossover in different systems. Finally, section 1.7 overviews the materials that will be covered in the rest of the thesis.

1.2 What is a Glass?

1.2.1 Dynamics

If the cooling of the liquid is fast in comparison to the time of crystallization then freezing is avoided and molecular motion below the freezing point T_m, becomes slow. Finally, with decreasing temperature, molecules rearrange so slowly that they cannot adequately sample configuration space in the available time allowed by the cooling rate (viscosity reaches 10^{13} Poise: experimental definition of T_g) and instead of forming a crystalline structure, the disordered atomic configuration of the supercooled liquid is frozen into the solid state at the glass transition temperature T_g [4]. A glass exists as a metastable state with respect to its crystalline form, although in certain conditions, for example in atactic polymers, there is no crystalline state.

Glassy materials behave like a solid below their glass transition temperature on short time scale. However, the glass on extremely long time scales, beyond the experimental time scale, behaves like a liquid. Recently, the pitch drop experiment demonstrates the high viscosity or low fluidity of pitch–also known as bitumen or asphalt–a material that appears to be solid at room temperature, but is in fact flowing, albeit extremely slowly. A drop formation takes about 13 years with estimated viscosity of 20 billion times the viscosity of water [5]. Despite the stability of most glasses, in some cases it can nucleate and go through first order phase transition and become a crystal.

The most common method of measuring structural relaxation time is the self (–incoherent) part of the intermediate scattering function (ISF). This quantity can be obtained experimentally using inelastic neutron scattering [6,7]. First, the structure factor of the system has to be defined. The structure factor (SF), which is a mathematical description of how a material scatters incident radiation, is the Fourier transform of the radial distribution function and can be defined as [8],

$$S\left(\mathbf{k}\right)=\frac{1}{N}\left\langle\rho_{\mathbf{k}}\rho_{-\mathbf{k}}\right\rangle, \tag{1.1}$$

where, N is the number of particles and,

$$\rho_{\mathbf{k}}=\sum_{j=1}^{N}\exp\left[-i\mathbf{k}\cdot\mathbf{r}_j(t)\right], \tag{1.2}$$

$\mathbf{r}_j$ is the position of particle j at time t, and the angular brackets denote an equilibrium ensemble average over multiple configurations at different t. The wave vector $\mathbf{k}$ is defined as multiples of $\mathbf{k}=2\pi/L$ and L is the system length. This means L is the largest vector length and $2\pi/L$ is the shortest vector length. Small $\mathbf{k}$ vectors are looking at long length scales, and large vectors, are probing very short scales. The first peak in the static structure factor of the system is associated with freezing or the glass transition of a supercooled liquid [9].

The intermediate scattering function (ISF) is then defined as the Fourier transform of the Van Hove function $G\left(\mathbf{r},t\right)$:

$$F\left(\mathbf{k},t\right)=\int G\left(\mathbf{r},t\right)\exp\left(-i\mathbf{k}\cdot\mathbf{r}\right)d\mathbf{r}. \tag{1.3}$$

The van Hove Function for a spatially uniform system containing N point particles is defined as:

$$G\left(\mathbf{r},t\right)=\frac{1}{\rho}\left\langle\rho(\mathbf{r},t)\rho(\mathbf{0},0)\right\rangle. \tag{1.4}$$

The van Hove function therefore describes the probability of observing a particle at $\mathbf{r}$ at a time t, given that a particle was at the origin at time $t=0$. The van Hove function separates into two terms, the “self” (s) and “distinct” (d) parts. The self part of the intermediate scattering function is defined as:

$$F_s\left(\mathbf{k},t\right)=\frac{1}{N}\left\langle\rho_{\mathbf{k}}(t)\rho_{-\mathbf{k}}(0)\right\rangle=\frac{1}{N}\left\langle\sum_{j}\exp\left[i\mathbf{k}\cdot\left(\mathbf{r}_j(t)-\mathbf{r}_j(0)\right)\right]\right\rangle. \tag{1.5}$$

The ISF is usually measured at the maximum of the first peak ($|\mathbf{k}|=\mathbf{k}_{\text{max}}$) at low $\mathbf{k}$ in order to capture the long range structural relaxation of the system and to maximize the signal to noise ratio. Figure 1.2 shows the self–ISF for a system of simple equilibrium liquid (red line) and a supercooled liquid (blue line). At higher temperatures, the system shows a simple exponential function of time, while supercooled liquids behave differently. At short times, the microscopic regime is governed by collisional events, which is common in both

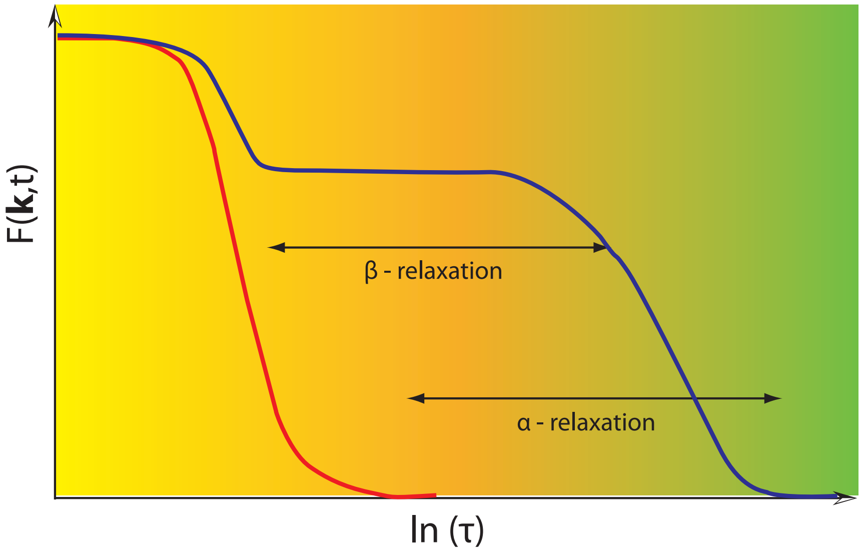

Figure 1.2: Typical relaxation behavior of intermediate scattering function for normal liquids and supercooled liquids. Single exponential decay in case of normal liquids (red line) and supercooled liquids show two steps relaxation (blue line) [10].

systems. In supercooled liquids, this regime is followed by a decay called β relaxation, which is associated with caging effects where the particles are trapped by their neighbors. At longer times, the particles are able to escape their cages, which leads to the α relaxation times that can be fitted with a stretched exponential function. As T_g is approached from above, the β relaxation plateau becomes longer as it becomes harder for the particles to escape the cages and below T_g no α relaxation is possible.

The temperature dependence of the transport properties is characterized by strong and fragile terminology which was defined by Angell [11]. The strong liquids follow the Arrhenius expression,

$$\tau\left(T\right) = \tau_0 \exp\left(\frac{E}{k_B T}\right), \tag{1.6}$$

where τ_0 and E are temperature–independent parameters and k_{B} is Boltzmann's constant. Strong liquids follow Arrhenius law above T_g and show a high resistance to structural changes. In these type of materials, the vibrational spectra and radial distribution functions show little reorganization over a wide range of temperatures with a small increase of specific heat (exception of where hydrogen bonds play a major role). Examples of these materials are silica, germanium dioxide ($\mathrm{GeO_2}$) and open network liquids such as boron trioxide ($\mathrm{B_2O_3}$).

In contrast, there are many examples of materials, including OTP(o–terphenyl), that ex-

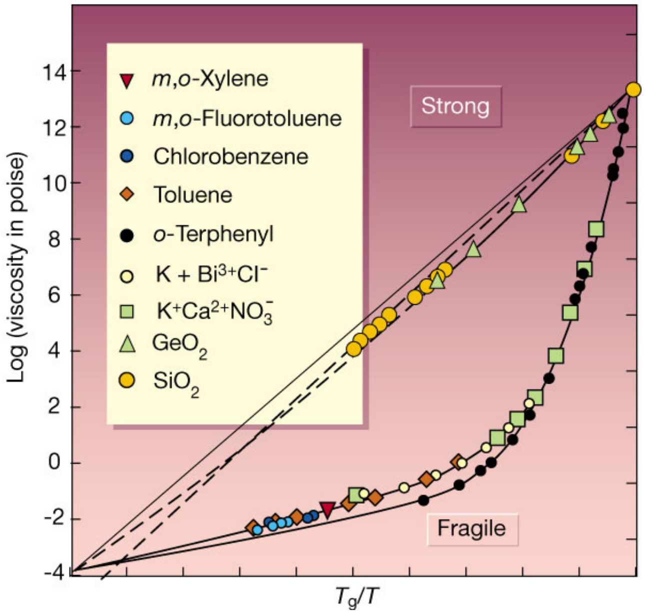

Figure 1.3: Reprinted with permission from Nature Publishing group from [4]. T_g scaled Arrhenius representation of liquid viscosities showing Angell's strong–fragile pattern.

hibit a super Arrhenius behavior, where their viscosity increases rapidly over a very short temperature range [4]. To express the relationship between transport properties and temperature, the most widely used function is the Vogel–Fulcher–Tammann (VFT) equation given by [12–14]:

$$\tau\left(T\right) = A \exp\left(\frac{B}{T - T_{VFT}}\right), \tag{1.7}$$

where A and B are temperature–independent constants and T_{VFT} is the VFT divergence temperature. This suggests that there is a divergence in the relaxation time at a finite temperature T_{VFT}, which is often used to argue for the existence of an underlying thermodynamic transition at T_{VFT}. The microscopic amorphous structure of a fragile glass can be made to collapse easily and they are able to reorganize their structure with different particle orientations and coordination states with little thermal excitation. The fragile (or strong) term does not refer to a particular brittleness of the material. Rather, the word qualifies how easily (respective difficulties) the system changes from one glassy state to another energetically degenerate glassy state. Figure 1.3 shows these two behaviors for experimental measurement of liquid viscosities. Strong liquids show a linear Arrhenius law behavior and fragile liquids show a large deviation from the Arrhenius law.

To quantify the fragile behavior, there is another popular fitting function that is known as the Avramov equation [15, 16]:

$$\tau(T) = \tau_\circ \exp\left(\frac{B}{T^n}\right), \tag{1.8}$$

where, n is a fitting parameter.

Like the VFT equation, the Avramov equation has two parameters in addition to the prefactor τ_0, but it has no dynamic divergence. Recently a quadratic equation, in reciprocal temperature [17], was introduced to fit relaxation data,

$$\log(\tau/\tau_\circ) \simeq \left(\frac{J}{T_\circ}\right)^2 \left(\frac{T_\circ}{T-1}\right)^2, \tag{1.9}$$

where J is an energy determining the growth rate of relaxation time as temperature decreased from a reference temperature, $T_\circ$. This temperature, $T_\circ$, is called the onset temperature, where the liquid dynamics crosses over from that of a simple liquid to that of a strongly correlated material like a glass former.

Finally, the power law [18],

$$\tau = \tau_0 \left[\frac{T - T_\times}{T_\times}\right]^{-\gamma}, \tag{1.10}$$

has been used in the same way to fit data in the fragile region [19]. Here γ is a non–universal exponent and $T_\times$ is defined as a temperature where the dynamics of the fluid is expected to crossover from the fragile regime to become a strong liquid. Fitting viscosity or relaxation data by using the power law equation is not very informative. The exponent γ strongly depends on the initial value chosen for $T_\times$ and $T_\times$ depends on the temperature range chosen for fitting. As $T \to T_\times$ or at low temperatures the power law becomes invalid and additional information is needed to eliminate arbitrariness [20].

1.2.2 Thermodynamics

Figure 1.4 contrasts the equilibrium freezing behavior of a liquid with that of glass formation. When a liquid is cooled to its equilibrium freezing transition point, it freezes through a first order transition where the volume, enthalpy and entropy all decrease discontinuously. As the crystal is cooled to the absolute zero temperature, the entropy also goes to zero for the perfect crystal according to the third law of thermodynamics. If crystallization is avoided, during cooling at a given rate, the thermodynamic properties of the system vary continuously until the system falls out of metastable equilibrium, forming glass "a". The intersection of the liquid and vitreous lines provides one definition of T_g, which usually occurs around 2/3 of the melting temperature, T_m. This behavior is not a first order phase transition because there is no discontinuous change in any physical property and no release of latent heat. If the liquid is cooled slower, at each temperature, there is more time available for configurational sampling, and hence the colder it can become before falling out of the liquid–state equilibrium and T_g decreases, forming glass "b". Glasses are non–equilibrium states because their properties depend on their history, *i.e.* the rate at which they were cooled.

The excess entropy $\Delta_c S$, of the supercooled liquid or glass, relative to the stable crystal, is calculated from,

$$\Delta_c S(T) = \Delta_c S(T_m) + \int_{T_m}^{T} \Delta_c C_p \mathrm{d}\ln T, \tag{1.11}$$

where $\Delta_c S(T_m)$ is the melting entropy at equilibrium and $\Delta_c C_p$ is the differences between heat capacity of supercooled liquid or glass relative to the stable crystal (excess heat capacity). $\Delta_c S$ calculated from the above equation varies continuously through the glass transition, but there is a discontinuity in the slope ($\Delta_c C_p/T$). Based on the thermodynamic rules, for calculating $\Delta_c S$, the path should be a reversible path but this may not be the case around the glass transition temperature [21]. Calculating the thermodynamic entropy of a glass at $T = 0K$ leads a nonzero value known as the residual entropy.

The entropy of a supercooled liquid decreases more rapidly as a function of temperature than that of the crystal. Kauzmann [22] pointed out that if the kinetic glass transition did not intervene then the entropy of the liquid would extrapolate to that of the crystal at a positive temperature. This temperature has been named the Kauzmann temperature, T_K. If a liquid could be supercooled below its Kauzmann temperature and it did indeed display a lower entropy than the crystal phase, the consequences would be paradoxical as $T \to 0K$. This has lead to the suggestion that there is an underlying thermodynamic phase transition to an ideal glass at T_K which avoids the violation of the third law of thermodynamics. This suggestion has lead to considerable debate and a search for the ideal glass state [23].

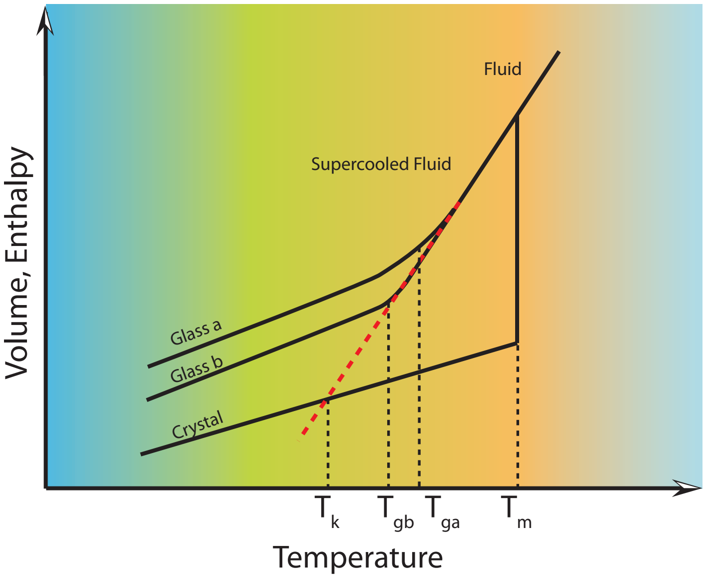

Figure 1.4: Temperature dependence of a liquids volume V or enthalpy H at constant pressure.

1.2.3 Structure

Glass, below its glass transition temperature behaves like a solid, but its atomic structure shares the characteristics structure of a supercooled liquid (for example, the radial distribution functions of a glass and a liquid are similar. [24]). The atomic structure of a glass has no long–range translational periodicity. However, due to chemical bonding and packing characteristics, glasses do possess a high degree of short–range order. Short–range order results in the formation of cages that slow down the dynamics of the particle. Therefore packing structures can be used to describe these cages. In glasses and in crystals, the rotational and translational motion is arrested and only the vibrational degrees of freedom remain active. This helps to explain why both crystalline and non–crystalline solids exhibit rigidity on most experimental time scales.

1.3 Theories of the Glass Transition

This section summarizes some of the main theories that are used to describe the underlying physics of the glass transition. The potential energy landscape, Adam–Gibbs theory, mode coupling theory, random first order theory, and facilitated dynamics will be highlighted here.

1.3.1 The Potential Energy Landscape

The potential energy landscape (PEL), which was originally introduced by Goldstein [25] and formalized and developed by Stillinger [26] in terms of inherent structure (IS), is a very useful way to study supercooled liquids, glasses and crystals. In this approach every configuration of the liquid can be mapped to the closest mechanically stable packing or potential energy minima (also called inherent structures). In a system with potential energy, any configuration can be mapped to its inherent structure by quenching the system using a steepest descent or conjugate gradient energy minimization. In a hard particle system, a configuration is ideally mapped to its inherent structure by continually expanding the particles, moving them apart on contact, until they become collectively jammed [27] in a local density maximum. Configurations that map to the same inherent structure are grouped together into basins (see Fig. 1.5). The dynamics and thermodynamics of the liquid can be described in terms of motion between basins on the landscape.

The PEL is a surface in $3N$–dimensional configurational space, where N is the number of particles, and can only be characterized on the statistical basis. The partition function Z of a system of N particles interacting via a two–body spherical potential is [25]

$$Z\left(T,V\right)=\frac{1}{N!\Lambda^{3N}}Q\left(V,T\right), \tag{1.12}$$

with

$$Q\left(V,T\right)=\int_V \mathrm{e}^{-\beta U\left(\mathbf{r}^{3N}\right)}\mathrm{d}\mathbf{r}^N, \tag{1.13}$$

where V is the volume and Λ is the de Broglie wavelength $h/\sqrt{2\pi m k_{\mathrm{B}}T}$, $\beta=1/k_{\mathrm{B}}T$, k_{B} is the Boltzmann constant and U is the total potential energy of the system.

The idea that the configuration space can be partitioned into basins allows to write the partition function as a sum over the partition functions of the individual distinct basins Q_i:

$$Q\left(T,V\right)=\sum_i{}' Q_i\left(T,V\right). \tag{1.14}$$

To model the thermodynamics of the supercooled state the sum has to exclude (and the sign $'$ in $\sum$ has this role) all basins which include a significant fraction of crystalline order [28]. Indicating by e_{IS} the value of the energy in the local minimum and with $\Delta U\left(\mathbf{r}^N\right)=U\left(\mathbf{r}^N\right)-e_{IS}$,

$$Q_i\left(T,V\right)=\mathrm{e}^{-\beta e_{IS_i}}\int_{\text{basin } i}\mathrm{e}^{-\beta\Delta U\left(\mathbf{r}^{3N}\right)}\mathrm{d}\mathbf{r}^N. \tag{1.15}$$

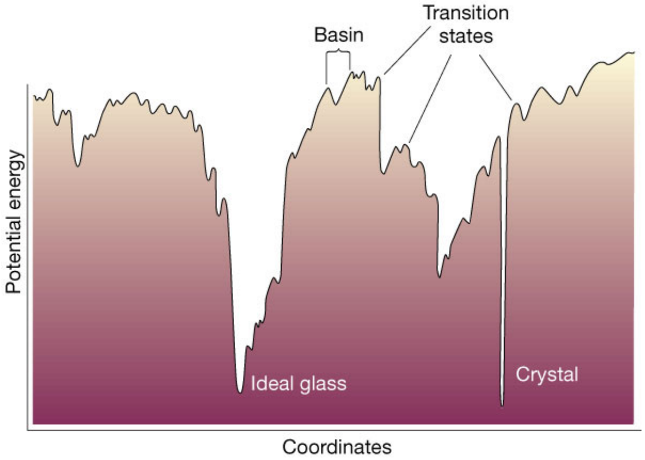

Figure 1.5: Reprinted with permission from Nature Publishing group from [4]. Schematic illustration for an energy landscape. The x$-axis$ represents all configurational coordinates.

Next a partition function is defined averaged over all distinct basins with the same e_{IS} value as

$$Q\left(e_{IS}, T, V\right) = \frac{\sum_i \delta_{e_{IS_i}, e_{IS}} Q_i\left(T, V\right)}{\sum_i \delta_{e_{IS_i}, e_{IS}}}, \tag{1.16}$$

and the associated average basin free energy as

$$-\beta f_{\text{basin}}\left(e_{IS}, T, V\right) = \ln \frac{Q_i\left(T, V\right)}{\Lambda^{3N}}. \tag{1.17}$$

The system partition function can be written as

$$Z\left(T, V\right) = \sum_{e_{IS}} \Omega\left(e_{IS}\right) \mathrm{e}^{-\beta f_{\text{basin}}\left(e_{IS}, T, V\right)}, \tag{1.18}$$

where $\Omega\left(e_{IS}\right) = \sum_i \delta_{e_{IS_i}, e_{IS}}$ counts the number of basins of depth e_{IS}. Note that the $N!$ term disappears since the sum is now over all distinct basins (i.e. an IS is invariant for permutation of identical particles). The configurational entropy, S_c is associated with the total number of inherent structures which the system samples.

The topological properties of the landscape can be related to the dynamics of a liquid. The potential energy landscape of strong glasses has few minima with high barriers whereas fragile ones had a high number of well–separated metabasins. In the context of the landscape description, the configuration entropy, S_c, of a system is the number of basins accessible to the supercooled liquid. The ideal glass transition would represent the point where $S_c \to 0$, and the system becomes trapped in a unique single basin.

The curvature of the energy landscape can be obtained from the second derivatives of the energy function. These second derivatives create a Hessian matrix and can be used to obtain the saddle points in the landscape. Saddle points are stationary points in a system with potential energy and can be classified on the basis of the number of negative eigenvalues (unstable directions) in the Hessian matrix of the potential energy of the configuration. When there are no negative eigenvalues, the saddle point is a stable inherent structure, otherwise the system contains one or more unstable, "soft" modes. At higher energies, the number of negative eigenvalues increases and on average more saddle points will exist. Similarly, in a system with a hard potential at lower densities saddle points are more abundant.

1.3.2 Adam–Gibbs Theory

One of the initial attempts to theoretically study the glass transition goes back to about 50 years ago, when Adam and Gibbs [29] proposed a theory of the glass transition. According to their proposal, supercooled liquids relax structurally through a sequence of individual events in which a subregion of a liquid relaxes to a new local minima. This structural relaxation occurs in "cooperatively rearranging regions" (CRRs), which grow larger in size as the temperature decreases. Adam–Gibbs (AG) suggested that by lowering the temperature the energy of the system decreases so that larger and larger regions have to act cooperatively in order for the liquid to relax. Eventually, at the Kauzmann temperature, T_K, the CRR becomes equivalent to the system size, which would require all the particles to cooperate.

Adam–Gibbs proposed the following equation as the connection between the structural relaxation time and the configurational entropy:

$$\tau \propto \exp\left(\frac{A}{TS_c}\right), \tag{1.19}$$

where A is a system dependent parameter related to the barrier to rearrangement. In the context of the PEL, the Adam–Gibbs relation suggests that the dynamics becomes slow as the system has access to fewer and fewer basins at low temperatures. If, S_c goes to zero, the relaxation time would diverge. This has been connected to the ideal glass transition and is expected to occur at T_K.

This theory provides a good connection between dynamics and thermodynamics of the glass transition and has been tested in both experimental [30,31] (where S_c is estimated from specific heat measurements) and numerical [32–38] (where S_c can be formally evaluated from an energy landscape approach) studies and the general picture proved in most of the cases, if not all systems studied.

One weakness regarding the AG theory is the fact that the size of CRRs is not known and this theory treats CRRs as indistinguishable especially in terms of heterogeneity that provides the stretched exponential behavior. In addition, recently in a study by Sengupta et al. they provided evidence that AG theory is not valid for 2D systems [39].

1.3.3 Mode–Coupling Theory

One of the well known attempts to theoretically study the glass transition is the Mode–Coupling Theory (MCT) introduced by Götze and collaborators [6,20]. This method requires the static structure factor, $S(\mathbf{k})$, as an input parameter and gives a correct quantitative description of the dynamics of dense simple liquids. In particular, the theoretical output of MCT captures the slow down of the structural relaxation caused by "caging" effects where particles are temporarily trapped by their neighbors. MCT predicts a critical temperature T_{MCT} (or density ϕ_{MCT}) which represents a transition from an ergodic to a non–ergodic state without any sign of a singularity in the thermodynamics of the system. This is modeled by:

$$\tau \propto \frac{1}{(T - T_{MCT})^{\gamma}}, \tag{1.20}$$

where, τ is the relaxation time. This equation shows a singularity in the dynamics at T_{MCT}, and the relaxation time diverges. From this point of view, MCT is able to predict a glass transition at a nonzero temperature. Debennedetti, Stillinger and coworkers have hypothesized that this crossover corresponds to a crossover from diffusion–dominated dynamics to energy–landscape–dominated dynamics [4, 40]. Moreover, MCT predicts a plateau and two scaling laws in time for relaxation time. The first scaling law describes the dynamics close to plateau and the second scaling shows the decay from plateau value to zero which obeys stretched relaxation function.

Despite the successful prediction of MCT about the general behavior of the systems it does not give any physical insight about these phenomena. An additional drawback of MCT, is that T_{MCT} always falls above the true glass transition temperature $T_{MCT} > T_g$ [10]. It should also be noted that the advanced theories of MCT suggest the possibility of an avoided transition [41].

1.3.4 Random First Order Transition Theory

Kirkpatrick, Thirumalai and Wolynes [42, 43] first used the concept of a random first order transition (RFOT) to describe glass formation in 1987, and since there has been many developments [6, 44–46]. RFOT is based upon the study of energy landscape of supercooled liquids and the rapid growth of relaxation time on cooling. As discussed in PEL section (1.3.1), understanding the energy landscape of a system is beneficial to understanding the behavior of the supercooled liquids, however it is too difficult to calculate for real systems. Therefore, RFOT was first studied for a simple system of the p–spin model [47–49]. Based on this theory, the configuration space of a supercooled liquid is decomposed into metastable regions called "entropic droplets", or "mosaics" with a characteristic size ξ, so the "configurational entropy" or "complexity" $S_c\left(T\right)$ can be defined:

$$S_c\left(T\right) = \frac{1}{N}\log N\left(f\right), \tag{1.21}$$

where $N(f)$ is the number of free–energy minima with a given free–energy density f (per unit of free-energy density).

According to RFOT, the driving force to reach equilibrium comes from the large number of regions with a specific length. Increasing the size of the regions means that the number of particles inside of each region will increase which provides an entropic energy favoring the the bigger regions. The energy gain from this is,

$$\Delta F_G = -TS_c\left(T\right)R^d, \tag{1.22}$$

where, d is the dimensionality of the system and R is the linear size of the regions. Here, the minus sign shows that this is an energy gain. However, dividing the system into different regions introduces an interface between the mosaics that is characterized by a surface tension. The surface tension is the free energy cost, per unit area, of creating the interface. Generally, for a region of size L, it requires an energy cost of L^{d-1} (d is the dimensionality). In the case of supercooled liquids the energy cost is usually defined as:

$$\Delta F_C = \Upsilon\left(T\right)R^{\gamma}, \tag{1.23}$$

where $\Upsilon\left(T\right)$ is the generalized surface tension and γ turns out to be much smaller than $d-1$. This is the cost that the system has to pay to create such regions.

The situation here is very similar to a nucleation process and there is a critical size for the regions, beyond which, the entropic term dominates so the net thermodynamic driving force favors the growth of the droplet. Balance of Eqs. 1.22 and 1.23 yields the size of rearranging region as:

$$\xi_M = \left(\frac{\Upsilon(T)}{TS_c(T)}\right)^{\frac{1}{d-\gamma}}, \tag{1.24}$$

where, ξ_M is a Mosaic correlation length. Notably, the Adam–Gibbs equation (Eq. 1.19) can be recovered from this equation.

Based on the analysis of RFOT, the configurational entropy of the system decreases by decreasing temperature and finally vanishes below T_K. This temperature is linked with the Kauzmann catastrophe discussed above. As T approaches T_K, the complexity, $S_c(T)$, behaves as

$$S_c(T) \sim (T - T_K)^{\alpha} \quad \text{where} \quad \alpha = 1. \tag{1.25}$$

RFOT does give a clear connection to the thermodynamics, but it is difficult to observe mosaics in the system directly.

1.3.5 Kinetically Constrained Models and Dynamic Facilitation

Another glass transition model that has got a great deal of attention is kinetically constrained models (KCMs). The core KCMs are the elementary spin–facilitated models such as East [50] and Fredrickson–Andersen [51] (FA) models and kinetically constrained lattice gases, Kob–Andersen [52] (KA) models.

The spin–facilitated models consist of chain states with occupations numbers, $n_i = 0, 1$ ($i = 1, ..., N$), with simple Hamiltonian $H[\{n_i\}] = J\sum_i n_i$ where J is an energy scale for creation of mobility. The dynamics of these models is subjected to local constraints. In case of FA model, a spin can flip if either of its neighbors is in the up state and in the East model, a spin can flip only if its nearest neighbor to the right is up. Whereas, for lattice gas model, Hamiltonian is $H[\{n_i\}] = 0$ and a particle can jump to a neighboring site only if both in the initial and final positions, at least m of its nearest neighboring sites are empty.

For a system of Kob–Andersen (80:20) binary Lennard–Jones mixture (BLJM), excitation defined as clusters of mobile particles. These crystals create string–like motions by motions of neighboring particles in local groups [53–55]. However, Chandler and Garrahan [56–60] define an excitation as a directional correlations between successive displacement events, of feasible particle displacements consistent with non–overlap constraints [57].

For all of these models, the thermodynamics plays a limited role, however, their dynamical behavior is a very powerful tool in capturing the glass transition fundamentals [60, 61]. The spatial constraints present in these models creates structural defects or empty space locally, and thus "facilitates" the subsequent motion of nearby particles. The relaxation time for these type of models follows the parabolic law (eq. 1.10) and the onset temperature, $T_\circ$, is the temperature below which the assumptions of facilitated dynamics hold.

Real glass forming liquids crystallize when cooled down sufficiently slowly through their melting point, however, KCMs can not capture this transition.

1.4 Hard Sphere Systems

The thermodynamic properties of hard–particle systems are solely a function of the density (occupied volume fraction). This represents the simplest model that can recreate the properties of a liquid, glass and crystal states.

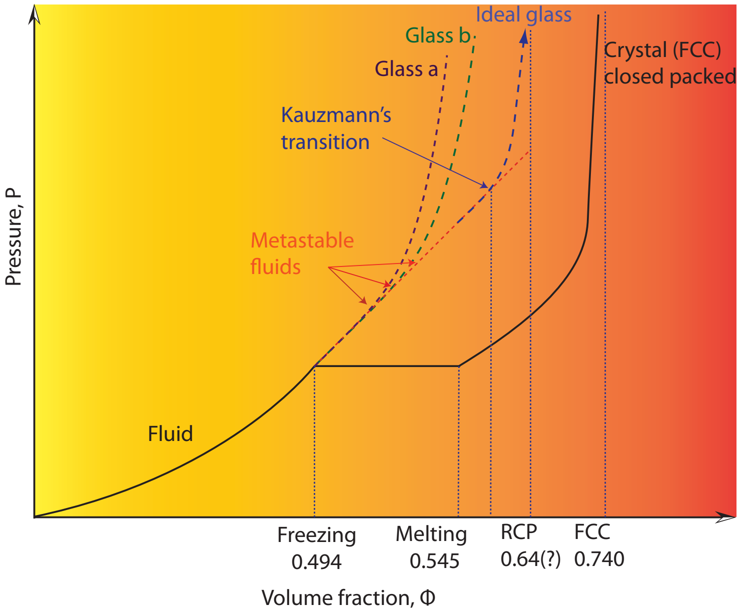

Figure 1.6: The pressure of hard spheres versus density near the transition region adopted from [62].

Figure 1.6 shows the schematic phase diagram of the three dimensional hard sphere system that is expected in the presence of a glass transition and plots the pressure as a function of the occupied free volume, $\phi = (N\pi\sigma^3)/(6V)$, where N, σ and V are the total number of particles, diameter of the spheres and total volume of the system respectively.

At $\phi = 0$, the hard sphere system is a set of points contained in a volume V, consistent with the ideal gas. As the system is compressed, by expanding the diameters of the particles, the pressure increases as the particles begin to exclude volume. Molecular dynamics simulations by Alder and Wainwright showed that the equilibrium system freezes to the face centered crystal (FCC) at $\phi = 0.4911$ [63, 64] before the pressure finally diverges at the close packed density $\phi = 0.74$.

However, if the fluid phase is compressed rapidly enough to avoid freezing, system enters a metastable state and by increasing the density, based on the compression rate the system goes through a glass transition and is stuck in one glassy state. In this figure, the compression rate for glass "a" is higher than glass "b". By very slow compression rate, the system may go through a transition to produce the ideal glass.

The pressure in the glass diverges as the particles become jammed in a mechanically stable packing at a density ϕ_J. Different glasses may have different ϕ_J so Speedy [32] argued that the partition function for the fluid could be constructed using the inherent structure formalism developed by Stillinger and Weber [26]. As expressed, the partition function of hard spheres as:

$$Q(\phi, \phi_J) = \sum_{\phi_J} \Omega(\phi_J) Q_\phi(\phi, \phi_J), \tag{1.26}$$

where Ω is the number of basins and $\mathrm{Q}_\phi(\phi, \phi_J)$ involve evaluating the mean vibrational partition function for basins as a function of their depth. The number of inherent structures for a hard potential system is expected to be given by [65],

$$\Omega(\phi_J) = \exp\left[N s_c(\phi_J)\right], \tag{1.27}$$

where N is the number of particles and s_c is the configurational entropy per particle. This suggests that the thermodynamics of the system can be understood in terms of the properties of the the basins and how fluid explores the inherent structure landscape. In equation 1.26, the $\mathrm{Q}_i(\phi, \phi_J)$ term is an increasing function of ϕ_J, at fixed ϕ, which means higher density basins have more vibrational free volume, but Ω is decreasing function of ϕ_J, i.e., at high densities the number of available basin is less than at low densities. The maximization in Q, results from the competition between these two parameters.

1.5 Particle Packing and Jamming Phase Transition

Studies of particle packing begin with Kepler [66] who in 1611 suggest the densest packing of identical spheres could be achieved by two common examples being the face–centered–cubic lattice (FCC) and the hexagonal–closed–packed (HCP) arrangements, with packing fraction of $\phi = \frac{\pi}{\sqrt{18}} = 0.74$. This is known as Kepler's conjecture and was recently proved by Hales [67] with aid of computer programming. This class of dense layered packings are known as Barlow packings [68, 69].

Bernal [70] used random packings of ball bearings to study the structure of liquids and coined the term random close packing (RCP) to describe the most dense random arrangement of spheres. When spherical grains are randomly thrown into a box and shaken, they form an amorphous arrangement with random close packing, which has significantly lower packing fraction than the densest crystalline packings. The packing fraction associated with RCP in hard sphere system is $\phi_{RCP} \approx 0.64$ and this value is a highly reproducible value.

Torquato and Stillinger [27] classified jammed packings into hierarchical categories of locally, collectively and strictly jammed configurations.

1. *"Locally jammed configuration*: Each particle in the system is locally trapped by its neighbors, i.e., it cannot be translated while fixing the positions of all other particles."

2. *"Collectively jammed configuration*: Any locally jammed configuration in which no subset of particles can simultaneously be continuously displaced so that its members move out of contact with one another and with the remainder set."

3. *"Strictly jammed configuration*: Any collectively jammed configuration that disallows all globally uniform volume–nonincreasing deformations of the system boundary."

Locally jammed condition requires at least $d + 1$ (d is dimensionality of the system) contacting particles, not all in the same hemisphere.

Computer simulation has been used extensively to study packing, but different protocols often lead to different conclusions regarding the density distribution of inherent structures for both hard disc mixtures [71–73] and hard spheres [74]. A recent study [75] of jammed packings also raised questions concerning the relationship between the structure of a packing and its density. Lubachevsky and Stillinger [76] introduced an algorithm (LS scheme) for producing jammed packing. In this algorithm the particles start with random positions and velocities. As the particles move during the event driven molecular dynamics (EDMD) simulation, the density is increased by expanding the diameters of particles at a constant rate, while keeping the volume of the system fixed. The system eventually becomes jammed as the pressure diverges and the particle diameters can no longer expand without causing overlap. It should be noted that this method does not map a starting configuration to its local inherent structure because the MD allows the system to relax and explore configuration space as the system is compressed. Simulations show that packing of different densities can be formed by compressing the system at different rates. However, if the system is compressed slow enough, it will follow the equilibrium equations of state and allow the particles to freeze at high densities.

This algorithm is the most frequent algorithm to produce hard sphere packing, which is collision–driven molecular dynamics (EDMD). Donev *et.al.*, have modified the collision driven MD algorithm to use for non–spherical hard particle system [77] and also, they described a practical algorithm to assess whether a hard sphere packing in two and three dimensions is jammed or not [78]. Meanwhile, they demonstrate jamming at ellipsoid packings [79], and studied disordered jammed hard sphere packing in four and five dimensions [80]. Recently, Anikeenko *et.al.* [74,81] used Delaunay simplexes decomposition to analyze amorphous packings of hard sphere systems and proposed "quasiperfect tetrahedra" as unit cells.

The number of collectively jammed states grows rapidly with number of particles. Bowles and Speedy [82] for five mono–disperse discs in a box, analytically found one crystalline and four amorphous inherent structures. Xu *et.al.* [72] used simulation to find all of the jammed structures for systems containing 10 or less bi–disperse particles. More recently Arkus et al. [83–85] used graph theory and geometry to enumerate all of the jammed configurations for a system of mono–disperse hard spheres with short–ranged attraction in a system of $N \leqslant 10$. In other work, Bowles and Saika-Voivod [86] enumerated the inherent structures of a confined hard disc system with channel to sphere diameter ratio $H_d/\sigma < 1 + \sqrt{3/4}$ using a combinatorial approach. Ashwin and Bowles [87] developed a tiling approach to counting inherent structures in jammed systems and they provide exact description of the complete jamming landscape for hard discs confined between two lines of $H_d/\sigma = 1.95$ by using the transfer matrix method [88].

1.5.1 Jamming Phase Diagram

Many different types of systems exhibit jamming phenomena, where the particles locked in place and can sustain an external stress or strain without flowing. Athermal systems, such as foams and emulsions jam as the shear stress decreases, and colloidal glasses jam as their packing density increases. Granular systems, including grains and sand exhibit jamming when vibrated. Many of these systems also share similar dynamic properties as the jamming transition is approached. This led Liu and Nagel [89] to propose a diagram that combines all jamming behaviors of these materials into a single graph. Figure 1.7 shows the jamming phase diagram (JPD) proposed by Liu and Nagel for granular material (figure on the left). The axes in this figure describes the parameters that control the transition to jamming for each of the three systems, namely temperature, density, and shear stress. For liquids, the temperature and density are the parameters that control the transition to jamming into a glass. Loose grains, bubbles, droplets etc. jam under shear stress or an increase with density. For systems with thermal motion temperature and load are the control parameters. Trappe et.al. [90] verified the general features of this unified concept experimentally for three different types of attractive colloidal systems (Fig. 1.7 figure on the right), but suggested different curvatures to the boundary lines.

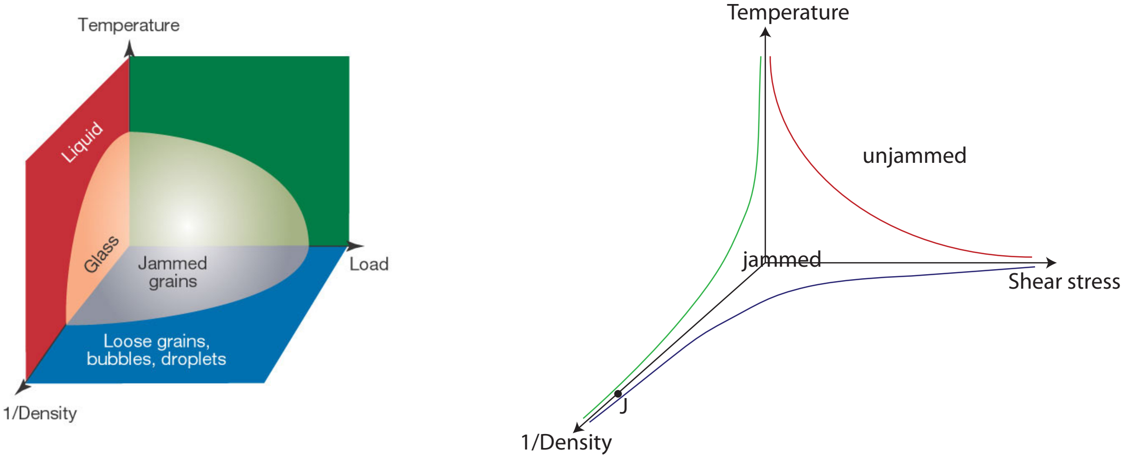

(a) (b)

Figure 1.7: Reprinted with permission from Nature Publishing group from [89]. Jamming phase diagrams proposed by Liu and Nagel [89] (a), and diagram obtained for attractive colloidal systems [90] (b).

Despite the success of the JPD, some fundamental questions remain. The "*J*–Point" represents the boundary between the jammed and unjammed states along the density axis at zero T. At lower densities, there are no jammed configurations and at higher densities, there are not meant to be any unjammed configurations. Many studies have argued that the RCP density of $\phi_J = 0.64$ is the "J–Point", but simulations of hard sphere packings suggest there are many different jamming densities [91–94], leading to the suggestion there is a jamming line ("J–line"). Furthermore, it is not clear how crystalline, or poly–crystalline configurations, fit into the jamming phase diagram. Since the crystal density is much higher than the RCP density, there must be unjammed configurations related to the vibrational modes of the crystal that exist beyond the J–point. Similarly, glasses are not truly jammed states and have vibrational degrees of freedom.

One of the theoretical approaches dedicated to phase diagram of glasses is replica mean field theory (RMFT). Following has some basic description regarding this theory.

1.5.2 Replica Mean Field Theory

Recent developments of the replica mean field theory (RMFT) [95–101], building on an earlier theory of the thermodynamic glass transition [102, 103], have made significant advances in the understanding of the jamming phase diagram by studying a class of jammed matter that can be approximated as the infinite pressure glassy states of a liquid. By focusing on a region of the metastable liquid where the caging of the particles by their neighbors localizes their dynamics, RMFT employs a replica version of equilibrium liquid methodologies as a starting point and has been shown to successfully describe thermodynamics of this class of jammed states. Most importantly, the theory predicts that jamming, in some idealized models [94, 104] and hard spheres [96, 105], does not occur at a single transition J–Point, as originally suggested, but occurs over a set of points constituting a segment on the density axis referred to as the J–line. The existence of the J–line in the hard sphere model has been subsequently verified by simulations [106, 107].

Within RMFT, the mean field relations describing the metastable state with volume fraction, ϕ, are mapped to relations describing the mechanically jammed states with volume fraction, ϕ_J, by considering a cage that momentarily traps the particles. The cage size is then systematically taken to zero under the mean field constraints. Physically, this amounts to an artificial quench, that renders the particles immobile due to their local neighborhood.

The long lived glassy states first appear in the fluid at ϕ_d and artificially quenching these states locates the lowest density bound of the J–line as ϕ_{th}. For hard spheres in three dimensions [101], $\phi_d = 0.58$, which coincides with the mode–coupling density for the system, and $\phi_{th} = 0.64$. The upper bound of the J–line, which occurs at the glass close packed density, ϕ_{GCP}, is obtained by artificially quenching the fluid at the Kauzmann density, ϕ_K, where the number of fluid states becomes subexponential and the system is expected to go through an ideal glass transition [4, 108]. Again, for 3d hard spheres, RMFT finds ϕ_K and ϕ_{GCP} to be approximately 0.62 and 0.68, respectively. However, despite the success of RMFT, it does not capture the complete picture of jamming because the glassy states of the metastable fluid only represent a subset of all possible inherent structures [26,32,71,109,110], which are the mechanically stable packings formed from infinitely fast quenches of any equilibrium fluid configuration, at any ϕ. The density of the J–point, ϕ_J^*, is defined as the ϕ_J of inherent structures obtained from ideal gas configurations, and while many jamming protocols [75,111–113] do find $\phi_J^* \sim \phi_{th}$, such quenches are not accessible within RMFT. Other protocols [107, 114] produce packing at much lower densities than 0.64 in hard spheres suggesting the existence of a wider range of packing densities than that predicted by RMFT.

1.6 Fragile–Strong Crossover

According to Goldstein's picture of the potential energy landscape [25], at high temperatures, where average thermal energy of the system is comparable to the heights of potential barriers, the system has access to a large portion of the landscape and can move between the basins easily. With decreasing temperature (or increasing the density in case of hard potential systems), diffusion becomes hindered and less phase space will be accessible. At low temperatures, but above the glass transition temperature, the system has two different types of diffusion processes: the thermal relaxation inside the basins (intra–basin relaxation, τ_{intra}) and the hopping between different basins in the potential–energy landscape by passing the barriers between basins (inter–basin relaxation, τ_{inter}). τ_{intra} corresponds to the time required for thermalization inside the minimum and τ_{inter} corresponds to the time for hopping among different minima.

At low T the two relaxation times (τ_{intra} and τ_{inter}) become well separated and $\tau_{inter} \gg \tau_{intra}$ [115]. Goldstein suggested there is a crossover temperature, $T_\times$, when the diffusivity of the system changes from a simple diffusive mode to a "solid"–like behavior as the temperature is decreased. $T_\times$ is in general higher than the glass transition temperature T_g. At temperatures below $T_\times$, barrier hopping dynamics will be dominant process. Above $T_\times$, the system is no longer spending most of the time vibrating around a single minima. Instead, it spends more time moving between basins, and is located in the saddle point regions of the landscape. These points are described as the connecting states between stable minima in the landscape and system visits these states more often at higher temperatures. The effect of saddles in the dynamics of glassy systems has been described using mean field theory [116–118].

The dynamics of fragile and strong liquids has been linked to these different regions of the landscape. The super–Arrhenius relaxation of a fragile liquid occurs when the system is in the saddle regions, where the particles move cooperatively. When the system is moving between basins through activated dynamics, it behaves like a strong liquid. This suggest $T_\times$ is the temperature of a fragile–strong crossover.

Remarkably, experimental and simulation results for silica [119, 120], silicon [121] and supercooled water [122–125] show evidence of dynamical crossover from fragile liquid to a strong liquid. The crossover temperature for these systems coincides with the Widom line which is marked by the heat capacity maximum of the system. A fragile–strong crossover has also been observed in a simple binary Lenard Jones system [126].

1.7 Thesis Overview

The primary goal of the current thesis is to study simple model systems for which the complete distribution of inherent structures can be calculated and explore the relationships between the properties of resulting landscape and the thermodynamics and dynamics of the fluid. To this end, hard disks and hard sphere systems in confined quasi–one–dimensional geometries are studied. The preliminary results of the analysis of the hard discs system described in Chapter 3 have been published in references [127–129] and here more details and new work are included. The coauthors of these papers have agreed to the inclusion of this material in the current thesis.

Chapter 2 introduces the concept of the packing landscape using a simple non–additive hard rod system. It provides an analytical description highlighting the connection between the equilibrium fluid and the inherent structures sampled by fluid and how the system moves between different basins on the landscape as the density is varied.

In chapter 3, the thermodynamics properties of a system of hard discs confined into a narrow channel is obtained using Transfer Matrix (TM) method. The equilibrium fluid then is mapped to its jammed state using a triangular mapping technique and the jamming phase diagram is developed as a result. The dynamics of the fluid is studied by measuring the relaxation time of the system. This is achieved using two independent methods, the survival probability method and the intermediate scattering function (ISF) method. The results obtained from these dynamics measurements show that fluid exhibits a fragile to strong dynamic crossover. The analysis shows that the crossover is located at the maximum of the isobaric heat capacity, which suggests an underlying connection between the thermodynamics of a fluid and its dynamics. This connection is explored in terms of the way particles pack together and the resulting inherent structure landscape.

In Chapter 4, a system of hard spheres confined in a narrow pore will be discussed. This chapter is divided into two sections: one examining pore diameters that only allows first neighbors contact and the second covers pores with diameters that also allow second neighbors contact.

By confining hard sphere in a channel with a diameter $1 < H_d/\sigma < 1 + \sqrt{3/4}$, the system only allow contacts between first nearest neighbor. As a result, there is only one inherent structure consisting of a linear, zig–zag chain of particles. The exact thermodynamics of the system are calculated using the TM method and the dynamics is measured using the ISF method. For the case $1 + \sqrt{3/4} < H_d/\sigma < 1.98$, the spheres can contact their second nearest neighbors as well, leading to a more complex packing landscape involving the formation of chiral helical packings. The thermodynamics and dynamics of the system are studied using molecular dynamics simulations. These reveal the existence of an orientational phase transition from a disordered fluid at low densities, to an orientationally ordered, but translationally disordered, fluid at high densities. The existence of the transition is confirmed through a finite system size analysis. The properties of the packing landscape are studied in relation to the phase transition.

In chapter 5, molecular dynamic simulation is used to study the dynamics of two–dimensional hard discs, confined to long, narrow, structureless channels with hard walls. This chapter shows that the value of the diffusion coefficient as a function of density in a quasi–one dimensional system can be rescaled to fit diffusion in a purely one dimensional system, using the exact equation of state. In addition, this study suggests that the self–diffusivity data of the quasi–1d system can be collapsed onto a single curve with the 1d data using an effective packing density.

The concluding remarks and proposals for future studies are presented in Chapter 6.

Chapter 2

A Binary Mixture of Non-Additive One-dimensional Hard Rods

2.1 Overview

In this Chapter, the theoretical description of the packing landscape will be introduced using a simple system of binary non–additive hard rods. In particular, the results will focus on exploring the connection between the thermodynamics of the fluid and how it samples the inherent structure landscape. The results of this Chapter will provide a basis for comparison of the more complex systems discussed in later chapters. Section 2.2 gives a brief introduction to the importance of the study of the hard rod systems. Section 2.3 describes the binary non–additive hard rod model. Section 2.4 focuses on the form of the distribution of the glasses obtained by analytical approach. Section 2.5 briefly introduces the formalism of heat capacity measurements for the system. Section 2.6 introduces the inherent structure and vibrational pressures. Finally, section 2.7 summarizes the results in the context of the jamming phase diagram.

2.2 Introduction

Despite the simplicity and lack of certain thermodynamic properties, the availability of exact results for the one–dimensional hard rod makes this system a valuable tool for the analysis of phenomena observed in more complex systems. Prigogine [130] introduced the general derivation of the thermodynamic properties of a one–dimensional mixture and Percus obtained the analytical free energy functional for both pure [131] and binary [132] systems. The non–additive hard rod system has been a subject of studies from a number of different aspects [133–135]. A detailed investigation of the inherent structure and glass transition was performed [136], but still some key points in relation to the jamming phase diagram and how the fluid samples the landscape have yet to be explored.

Formulating the inherent structure paradigm for a system of one dimensional hard rods on a line is straight forward because the particles are unable to pass each other and they only interact with their immediate neighbors. Compressing the system will map a fluid configuration to its inherent structure where all the particles contact their two nearest neighbors to satisfy the local jamming criteria. Since the particles cannot pass, there are also no collective motions that can lead to unjamming, so the structures are collectively jammed. The partition function for a glass is then given by all the configurations of the particles in a fixed order and the full partition function of the fluid is formed summing over all the possible arrangements of the particles. For a single component system of additive hard rods, there is just a single inherent structure with jammed occupied volume, $\phi_J = 1$. The thermodynamic properties are the result of free volume only and can be calculated exactly [137]. For example, the isobaric heat capacity (C_p) of an additive one dimensional system is a constant value and has no C_p maximum. The additive binary mixture has many different inherent structures arising from the distinguishable particle arrangements, but they all have the same ϕ_J and the same free volume as a function of density, so the inherent structure landscape plays no role in the thermodynamics. However, when the rods in the binary mixture become non–additive, the density of the jammed structure becomes dependent on the arrangement of the rods and the inherent structures with a distribution of jamming densities can be seen. This gives rise to a more interesting landscape that can still be studied exactly.

2.3 Model Description

The one dimensional, binary mixture of non–additive hard rods has been previously described in Ref. [136], but here will include its main features here for the sake of completeness as well as introducing some new analysis. The model consists of N_A rods of component A that interact with each other with a particle diameter of σ_{AA}, and N_B rods of component B that interact with each other with a particle diameter σ_{BB}. The total number of particles is then $N = N_A + N_B$ and the occupied volume is $\phi = N\left(x_A\sigma_{AA} + x_B\sigma_{BB}\right)/L$, where x_A and x_B are the fraction of each component and L is the one dimensional volume of the system. This study focuses on the equimolar system with $x_A = x_B$. The interaction diameter between

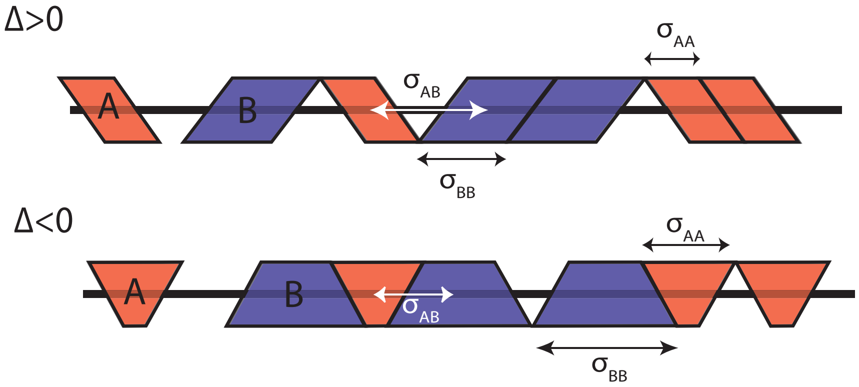

Figure 2.1: Cartoon representation of the non–additive hard rod system. Top graph: positive non–additivity depicted using left–tilted rhombi. The small species (A) interact with σ_{AA} and large species (B) interact with length σ_{BB} with their own type and the length σ_{AB} is the interaction length between type A and B. Bottom: A similar situation for negative non–additivity illustrated using wedges (adapted from [135]).

particles of component A and B is defined as,

$$\sigma_{AB} = (1/2)\left(\sigma_{AA} + \sigma_{BB}\right) + \Delta, \tag{2.1}$$

where Δ is the non–additivity parameter. It should be noted that there is a limit to the value of Δ. If it is too negative, it allows second nearest neighbors to interact. The idea of non–additivity in one dimension is shown in the Fig. 2.1 using rhombi and wedge systems. When $\Delta = 0$, one recovers the additive binary mixture of hard rod system where all possible arrangements of the rods yield the same jamming density $\phi_J = 1$. However, when $\Delta \neq 0$, ϕ_J depends on the arrangements of the particles and is given by,

$$\phi_J = \left[1 + 2\Delta x_{AB}/\left(\sigma_{AA} + \sigma_{BB}\right)\right]^{-1}, \tag{2.2}$$

where x_{AB} is the mole fraction of AB interactions. This gives rise to inherent structures with a range of jamming densities. When $\Delta > 0$, which is the focus of the current discussion, the most dense jammed state, $\phi_{J\,\mathrm{max}}$, is achieved when the system is completely phase separated so $x_{AB} = 0$ (Fig. 2.2 top sketch). The least dense jammed state, $\phi_{J\,\mathrm{min}}$, occurs when the A and B rods alternate so that $x_{AB} = 1$ (Fig. 2.2 bottom sketch). The situation is reversed with $\Delta < 0$.

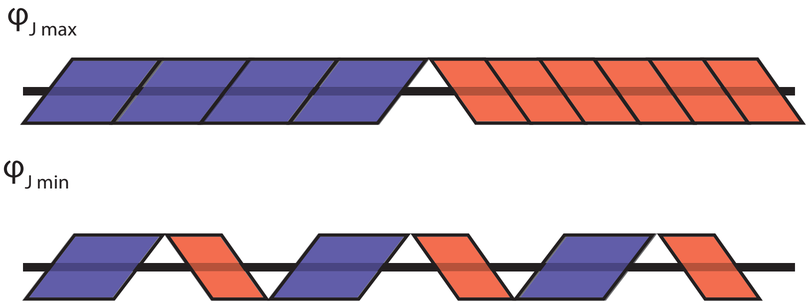

Figure 2.2: Most dense ($\phi_{J\,\text{max}}$ top) and least dense ($\phi_{J\,\text{min}}$ bottom) structures for the binary hard rods systems with positive non–additivity.

2.4 Distribution of Glasses

The number of jammed states, N_J, with the density ϕ_J can be obtained by considering the number of different ways the particles can be arranged on the line such that there are x_{AB} interactions [130, 136]. Then the entropy of the jammed states can be defined as $S_J/Nk_\text{B} = \ln N_J$, which is given by

$$\frac{S_J(\phi_J)}{Nk_\text{B}} = -\left(1 - x_{AB}\right)\ln\left(1 - x_{AA}\right) + x_{AB}\ln x_{AB}. \tag{2.3}$$

Within the inherent structure paradigm the vibrational (free volume) entropy of a single glass, relative to the ideal gas at the same temperature and density, $\Delta_{ig}S_g\left(\phi, \phi_J\right)$, can be obtained from the partition function of the rods constrained to remain in the same order on the line. A fluid can sample all possible inherent structures but at a given ϕ, it will generally sample the set of basins with the ϕ_J that maximize its total entropy, $\Delta_{ig}S_f\left(\phi\right)$. This gives,

$$\Delta_{ig}S_f\left(\phi\right) = S_J\left(\phi_J\right) + \Delta_{ig}S_g\left(\phi, \phi_J\right), \tag{2.4}$$

where the equilibrium ϕ_J is found using the condition $\left(\partial\Delta_{ig}S_f\left(\phi\right)/\partial\phi_J\right)_\phi = 0$ and the configurational entropy of the fluid $S_c\left(\phi\right) = S_J\left(\phi_J\right)$.

Figure 2.3 shows the distribution of inherent structures in terms of $S_J\left(\phi_J\right)$ for different values of the non–additivity parameter. The width of the distribution as a function of Δ decreases and in the limit of $\Delta \to 0$ the system becomes additive with a single jammed state. Figure 2.4 shows how the equilibrium liquid samples the basins in the landscape. It can be seen that the system samples the deeper basins as the fluid quenches from higher densities.

By considering Figs. 2.3 and 2.4 together, it reveals some insight about the entire landscape

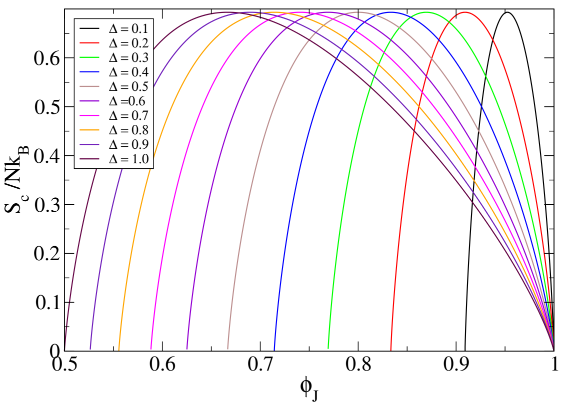

Figure 2.3: The distribution of glasses with jammed density ϕ_J for different values of the non–additivity parameter, Δ.

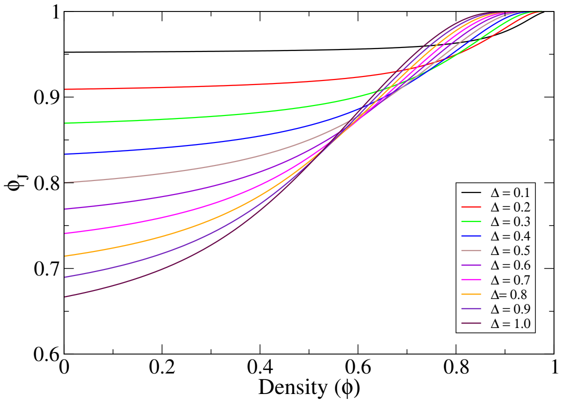

Figure 2.4: The jammed state densities that the equilibrium fluid samples as a function of density, for different values of the non–additivity parameter, Δ.

of the system. Figure 2.5 combines these two figures and shows the connection between them more explicitly. There is only one configuration at $\phi_{J\,\mathrm{max}}$ ($S_J = 0$) and at $\phi_{J\,\mathrm{min}}$, while the distribution goes through a maximum at an intermediate density, ϕ_J^*, when $x_{AB} = 0.5$ (Fig. 2.5a). There are inherent structures all the way down to $\phi_{J\,\mathrm{min}}$, but it be can seen from Fig. 2.5b that the equilibrium fluid only samples inherent structure basins above ϕ_J^*. This implies that any compression of an ideal gas configuration, that does not allow the system to escape its local basin, would end up jamming at ϕ_J^*. The equilibrium properties of the fluid are determined by the competition between free volume entropy and configurational entropy. Basins with denser inherent structures have more free volume, but there are fewer of them, so the equilibrium fluid samples deeper basins on the landscape as it is compressed until the system eventually becomes unavoidably jammed as $\phi \to \phi_{J\,\mathrm{max}}$. At densities below $\phi_{J\,\mathrm{min}}$, there are no configurations of the particles that are jammed.

Figure 2.6 shows S_c as a function of ϕ for the systems with different values of non–additivity. Here, it can be seen that the ideal gas samples the inherent structures at the maximum of the distribution, ϕ_J^*, then the fluid moves to basins with a higher ϕ_J with increasing density. The basins with $\phi_J < \phi_J^*$ are never sampled by the equilibrium fluid. At low ϕ, the configurational entropy of the fluid decreases slowly before it begins a rapid decrease at intermediate occupied volume fractions. An extrapolation of the S_c to higher ϕ, based on its behavior in this intermediate regime, would suggest the system exhibits a

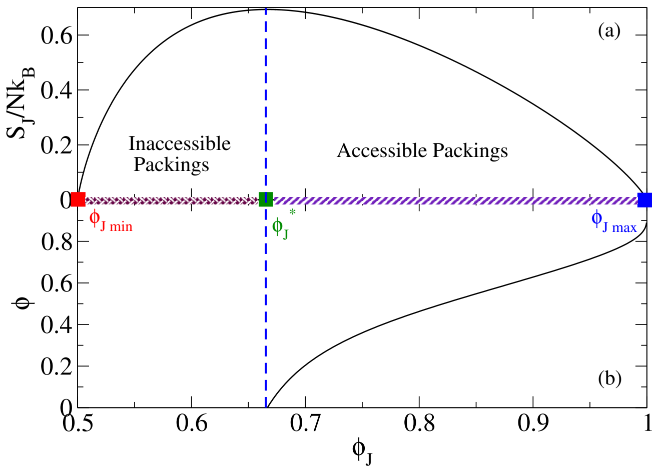

Figure 2.5: Distribution of inherent structures (a) and how the equilibrium fluid samples the inherent structures (b) for the system with $\Delta = 1$.

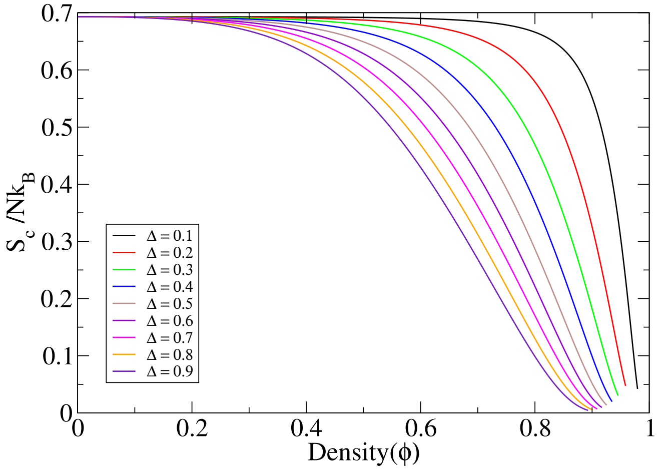

Figure 2.6: S_c as a function of ϕ for the systems with different values of non–additivity

Kauzmann catastrophe where the configurational entropy goes to zero at a ϕ well below $\phi_{J\,\mathrm{max}}$. However, S_c plateaus at high ϕ and only approaches zero in the limit $\phi \to 1$. As a result, there is no ideal glass transition in this system.

2.5 Heat Capacity

This model also can be used to study how features of the landscape influence the thermodynamic properties of the system, such as the heat capacity and the equation of state (EOS). The isobaric heat capacity, $C_p = \left(\partial H/\partial T\right)_p$, where for the hard rods model, the enthalpy is $H = (1/2)\, N k_\mathrm{B} T + PL$, with the compressibility factor $PL/Nk_\mathrm{B}T = 1 + \phi/\left(\phi_J - \phi\right)$. Note that here, P is the 1d pressure and the equivalent to the pressure to the bulk systems and ϕ_J is the jammed density that the equilibrium fluid samples and not the most dense configuration's density, $\phi_{J\,\mathrm{max}}$. Therefore, the heat capacity is given by

$$C_p/Nk_\mathrm{B} = 1/2 + \frac{\left(PL/Nk_\mathrm{B}T\right)^2}{\left(PL/Nk_\mathrm{B}T + \left(PL/Nk_\mathrm{B}T - 1\right)\left\{1 + \left(PL/Nk_\mathrm{B}T - 1\right)\left(1 - d\phi_J/d\phi\right)\right\}\right)}. \tag{2.5}$$

Figure 2.7 represents the inverse of compressibility factor as a function of density for different non–additivities. Figure 2.8 shows that C_p as a function of $\left(\phi PL/Nk_\mathrm{B}T\right)^{-1}$ goes through a maximum as a result of the maximum in the term $d\phi_J/d\phi$ (See Fig. 2.5). The peak also sharpens and moves to lower temperatures as $\Delta \to 0$, in a manner that is somewhat similar to a system approaching a critical point. This coincides with the narrowing of the inherent structure distribution which collapses to a single state at $\Delta = 0$. It is also interesting to note that the density of the fluid at the C_P maximum is equal to ϕ_J^* as this seems to connect the properties of the fluid at high densities to the ideal gas, through the inherent structure landscape.

2.6 Inherent Structure Pressure

Shell and Debenedetti [23] showed that the properties of the EOS of a fluid could be related to the inherent structure landscape by separating the equilibrium pressure into contributions from the inherent structure pressure, P_{IS}, and vibrational pressure, P_{vib}, so that,

$$P = \left(P_{IS} + P_{vib}\right). \tag{2.6}$$

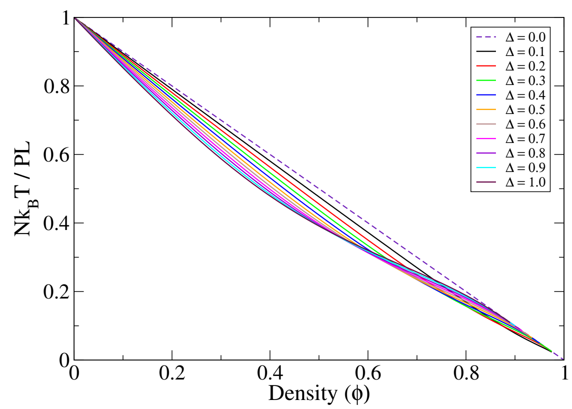

Figure 2.7: EOS for different non–additivity parameter as a function of density(ϕ).

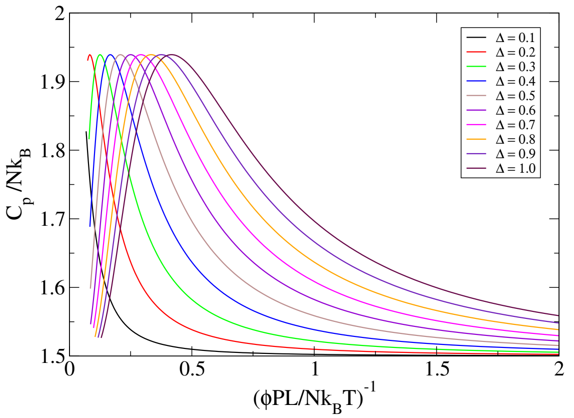

Figure 2.8: C_P/Nk_B for different non–additivity parameter as a function of $(\phi PL/Nk_\mathrm{B}T)^{-1}$.

Making use of the general relation $P = T(\partial S/\partial V)_U$, the inherent structure pressure can be calculated as

$$\beta P_{IS} = -\phi^2 \left(\frac{\partial S_c/Nk_\mathrm{B}}{\partial \phi} \right)_U , \tag{2.7}$$

and then obtain P_{vib} from Eq. 2.6. Both contributions to the pressure are shown in Figs. 2.9 and 2.10. The vibrational pressure increases monotonically as a function of ϕ while P_{IS} exhibits a maximum at densities that are slightly higher than where the C_p maximum appears.

2.7 Jamming Phase Diagram

The key elements of this model can be summarized in the form of the jamming phase diagram (see Fig. 2.11). $\phi_{J\,\mathrm{max}} = 1$ for all Δ. The jammed packings above ϕ_J^* are all accessible in the sense they can be reached by compressing the fluid from an equilibrium configuration at the appropriate density. The jammed states below ϕ_J^* are inaccessible and there are no jammed configurations below $\phi_{J\,\mathrm{min}}$. The figure also identifies the density of fluid at the maxima in C_p and P_{IS}, highlighting the connection between the inherent structure landscape and the thermodynamic properties of the fluid.

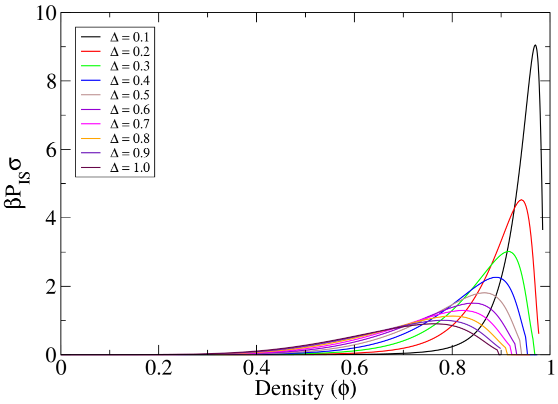

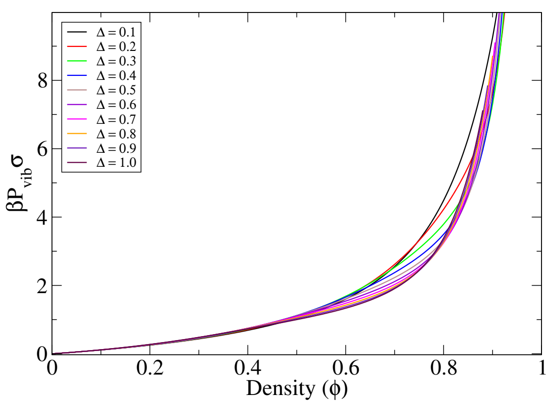

Figure 2.9: Inherent structure pressure as function of density for different values of non–additivity, Δ.

Figure 2.10: Vibrational pressure as function of density for different values of non–additivity, Δ.

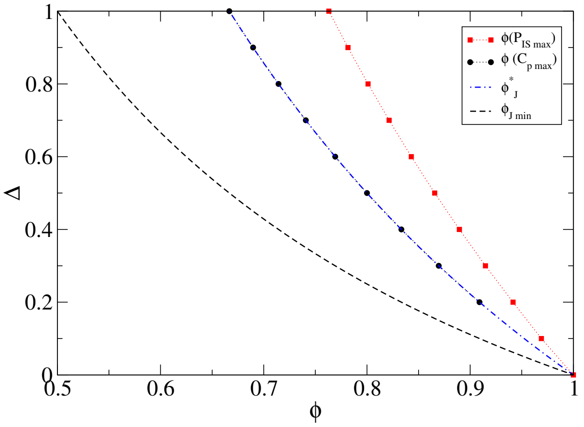

Figure 2.11: The jamming phase diagram for the non–additive binary mixture of hard rods model, including $\phi_{J\,\max}$, $\phi_{J\,\min}$, and ϕ^*_J, as a function of Δ.

2.8 Concluding Remarks

The properties of liquids, glasses and jamming phenomena have always been an interesting and challenging topics in the field of soft and condensed matter, and after decades of research, many of their features are still not well understood. The potential energy landscape, or its hard particle equivalent, was introduced to provide a framework for describing the properties of these systems. However, the complexity of landscape and the challenges associated with mapping configurations to their local inherent structures make it difficult to determine exactly how the thermodynamics and dynamics are related to the features of the landscape. In this Chapter, a system of binary non–additive hard rods was studied to give some insight into the relationships between these quantities. The distribution of jammed states was calculated and the equilibrium fluids were mapped to their inherent structures by taking an analytical approach. This allowed the connections between the thermodynamic properties of fluid and the inherent structure landscape to be explored.

The materials in this Chapter provide the guideline for the rest of the thesis and the next two Chapters will follow the same terminology. The inherent structure landscape and the connection of the dynamics and thermodynamics will be discussed in quasi–one dimensional confined hard discs and hard sphere systems in Chapters 3 and 4 respectively.

mo

Chapter 3

2D Hard Discs in Confined Geometry

3.1 Overview

This chapter examines the jamming phase diagram in a two dimensional system of hard discs confined to a narrow, quasi–one–dimensional, channel. The complete distribution of inherent structures is calculated and the relationships between the properties of resulting landscape and the thermodynamics and dynamics of the fluid will be discussed. In addition, the role of defects and soft modes on the dynamics of the fluid will be explored. The chapter is organized as follows: Section 3.2 gives a brief introduction to hard discs in confined geometries. Section 3.3 introduces the model. Section 3.4 describes the analysis of the inherent structure landscape and Section 3.5 discuss the thermodynamics of the model obtained using the transfer matrix method. Section 3.6 describes the molecular dynamics simulations used to confirm the analytical results and study the dynamics. Finally the discussion is contained in Section 3.7.

3.2 Introduction

Recent advances in technology, especially at the nano scale, have lead to an increased interest in confined systems. For example, porous media such as zeolites [138–142], micro– and nano–fluidic devices [143, 144], transport in narrow tubes such as carbon nano tubes (CNT) [145–148], biological ion–channels [149] and pores in biological membranes [150] are just a few of the applications of these systems. To understand the properties of confined fluids, it has been useful to study simple model systems such as hard discs and hard spheres confined to narrow channels. If the channel is quasi–one–dimensional and sufficiently narrow that the particles can only interact with their first nearest neighbors, then the transfer matrix method (TMM) can be used to analytically study the equilibrium properties of the system. Kofke and Post [151] used TMM to calculate the equation of state for the hard discs and spheres confined in narrow tubes and showed these systems exhibits a continuous transformation from a one–dimensional gas–like behavior, at low densities, to a zigzag solid–like structure at high densities [152]. The effect of the longitudinal and the transverse pressure on the structural correlation function has also been studied using transfer matrix method [153].

The confined hard disc model provides a simple system that can be used to study the inherent structure landscape. In this regard, combinatorial approach [86] and tiling [87, 88] approaches were taken to study the packing landscapes in these confined systems. In particular, the hard discs systems allows the study of the dynamics as the particles can move between different inherent structure basins. This was not possible in the purely one–dimensional system studied in Chapter 2. For example, Godfrey and Moore [154] recently developed a transition state theory to described the dynamics of the fluid at high densities. The dynamic properties of this confined system, such as hopping time [155–161] and mean squared displacements [162] have been studied. Furthermore, a knowledge of the ensemble of jammed states is of considerable interest to the development of a granular statistical mechanics [163] and the confined hard disc model has been used to test ideas relating to temperature–like thermodynamic quantities such as the compactivity [164,165] and the effects of a gravitational field on packings [166].

Despite the diverse studies on this model, still there is a lack of knowledge in some of the key areas for the system. In the following, the complete packing landscape of this model will be discussed using the TMM. How the equilibrium fluid samples the landscape will be examined and how the features of this landscape influence the dynamic properties of the system will be studied.

3.3 Model Description

The model consists of N two–dimensional (2d) hard discs, with diameter σ, confined between two hard walls (lines) of length L separated by a distance $1 < H_d/\sigma < 1 + \sqrt{3/4}$, where H_d is the channel width. The particle–particle and particle–wall interaction potentials are given by,

$$U(r_{ij}) = \begin{cases} 0 & r_{ij} \geq \sigma \\ \infty & r_{ij} < \sigma \end{cases} , \tag{3.1}$$

and

$$U_w(r_i) = \begin{cases} 0 & r_y \leq |h_0/2| \\ \infty & \text{otherwise} \end{cases} , \tag{3.2}$$

respectively, where $r_{ij} = |\mathbf{r_j} - \mathbf{r_i}|$ is the distance between particles, r_y is the component of the position vector for a particle perpendicular to the wall and $h_0 = H_d - \sigma$ is the reduced channel diameter. The two dimensional volume accessible to the particle centers is then $h_0 L$ and the occupied volume is $\phi = N\pi\sigma^2/(4LH_d)$.

3.4 Transfer Matrix Method

3.4.1 The Inherent Structure Landscape (ISL)

Hard discs in two–dimensions are locally jammed if they have at least three contacts that are not all in the same semicircle [27]. By confining the discs to a channel width $H_d/\sigma < 1+\sqrt{3/4}$, the particles can only contact their nearest neighbors on each side and the wall. As a result, there are only four local particle configurations that can be combined to form to configurations that satisfy the local jamming constraints in 2d, two dense configurations (denoted 1 and 3), and two open defect type configurations (denoted 2 and 4). Configurations 1 and 3 are mirror images of each other, with the mirror plane located along the central axis of the channel. Similarly, configurations 2 and 4 are also mirror images of each other (see Fig. 3.1). These configurations can be combined to create locally jammed configuration of N particles that can be described by an ordered list of the bond types joining particle centers. However, not all bond arrangements result in a jammed state because some of the local environments are incompatible with each other. Neighboring $-1-1-$ and $-3-3-$ configurations are incompatible because they start and finish on opposite side of the channel and need to be bridged by a $-3-$ or $-1-$ respectively to join particle centers. Configurations of neighboring defects ($-2-2-$ and $-4-4-$) are also incompatible as they result in local configurations where the central disc has three contacts all in the same hemisphere, allowing it to move laterally and unjam. For example, see the grey disc in the $-4-4-$ arrangement pictured in Fig. 3.1. If all the particles in a configuration satisfy the local jamming conditions, then the configuration is also collectively jammed because the particles are unable to pass each other.

The quasi–one dimensional nature of this system makes it possible to use the transfer matrix method to construct the ensemble of inherent structures [88]. The length added to

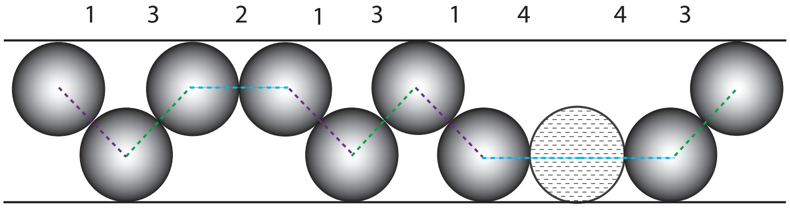

Figure 3.1: Local packing arrangements of discs. Dashed lines connect the centers of neighboring discs in contact, and the numbers identify different "bonds". Bonds 1 and 3 are the locally most dense states. Bonds 2 and 4 represent the defect states. The $-4-4-$ arrangement results in an unjammed particle (dash filled).

the system along the axis of the channel when a bond of type j follows a bond of type i is l_{ij}, with $l_{i,1} = l_{i,3} = \left[H_d\left(2\sigma - H_d\right)\right]^{1/2}$ and $l_{i,2} = l_{i,4} = \sigma$. For fixed N, the volume of the system will fluctuate depending on the number of type 2 and 4 bonds in the configuration so the longitudinal pressure P_L, is introduced as a conjugate variable to the volume and the system is fixed at a constant temperature, T. The transfer matrix then takes the form:

$$M = \begin{bmatrix} 0 & 0 & M_{1,3} & M_{1,4} \\ M_{2,1} & 0 & 0 & 0 \\ M_{3,1} & M_{3,2} & 0 & 0 \\ 0 & 0 & M_{4,3} & 0 \end{bmatrix}, \tag{3.3}$$

where $M_{i,j} = C_{i,j}\exp\left(-\beta P_L h_0 l_{i,j}\right)$. The exponential term is the Gibbs measure appropriate for the N, P_L, T ensemble and $C_{i,j}$ is zero when the two bonds are incompatible and one otherwise. In the thermodynamic limit, the partition function for the system is given by,

$$\Delta\left(N, P_L, T\right) = \left(\lambda\right)^N, \tag{3.4}$$

where λ is the largest eigenvalue of M. The jamming density, ϕ_J, is then given by,

$$\phi_J = \frac{N\pi\sigma^2}{4H_d L_J} = -\frac{\pi\sigma^2}{4k_{\mathrm{B}}TH_d\partial\left(\ln\lambda\right)/\partial P_L}, \tag{3.5}$$

where L_J is the length of the system in the jammed state. The entropy of jammed states $S_J = k_{\mathrm{B}}\ln N_J$, where N_J is the number of jammed configurations with ϕ_J, can be written as,

$$S_J/Nk_{\mathrm{B}} = \ln\lambda + T\partial\left(\ln\lambda\right)/\partial T. \tag{3.6}$$

The resulting eigenvalues are necessarily functions of N, P_L and T. The factors associated with N were dealt with by considering the system in the thermodynamic limit and calculating quantities on a per particle basis. T plays no direct role in the hard particle system, except to provide the velocity distribution of the particles. Here the system just deals with jammed structures where there is no free volume and the particles are unable to move, which implies that $T = 0$. The equilibrium fluid, including free volume, is described in Section 3.5. In the absence of temperature, there is no internal pressure caused by the collision between particles. However, it is still necessary for the system to do work against the pressure P_L when it expands so the equation of state for the ensemble of jammed configurations results from the connection between the work required to expand the volume of the system and S_J. The full distribution of states can be obtained by varying the pressure from $-\infty \to \infty$.

Figure 3.2 shows that the distribution of jammed states has a similar form to that obtained for the 1d model (Fig. 2.3 and ref. [136]), but with a lower entropy because of the need to eliminate states with neighboring defects. The results obtained using the transfer matrix method are identical to those obtained using a combinatorial approach [86].

Using the combinatorial method, the number of jammed states, $N_J(\phi_J)$, can be defined as [86]:

$$N_J(\phi_J) = \frac{(N-M)!}{M!\,(N-2M)!}, \tag{3.7}$$

where N is the total number of bonds and M counts the number of defect type bonds (2 and 4). By defining the fraction of defect bonds as $\theta = M/N$, the configurational entropy will be ($S_J = k_\mathrm{B} \ln N_J(\phi_J)$):

$$S_J/Nk_\mathrm{B} = (1/N)\ln(N_J(\phi_J)) = (1-\theta)\ln(1-\theta) - \theta\ln\theta - (1-2\theta)\ln(1-2\theta), \tag{3.8}$$

and the density of jammed states is given by:

$$\phi_J = \frac{\pi}{4H_d\left(\theta + (1-\theta)\sqrt{H_d(2\sigma - H_d)}\right)}. \tag{3.9}$$

The most dense and least dense states occur when $\theta = 0$ and $\theta = 0.5$ respectively, and both have $S_J = 0$. The most dense state is obtained in the limit $P_L \to \infty$ and the least dense state is obtained as $P_L \to -\infty$. Figure 3.3 shows the configurations representing these two jammed states. The density distribution of inherent structures goes through a maximum at an intermediate density, ϕ_J^*, when $\theta = 1/2 - \sqrt{5}/10$ and $P_L = 0$. The jamming phase diagram for the model (Fig. 3.4) shows that while the functional form of the distribution of inherent structures remains the same over the range of channel diameters $1 < H_d/\sigma \le 1 + \sqrt{3/4}$, the

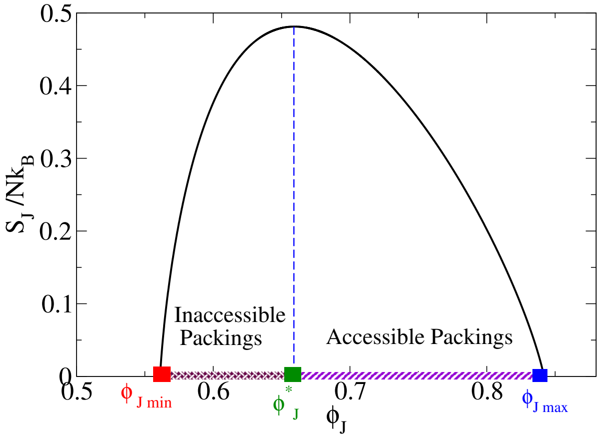

Figure 3.2: S_J/Nk_B versus ϕ_J for $H_d/\sigma = 1 + \sqrt{3/4}$. The thermodynamically accessible packings have occupied volume fractions between $\phi^*_J = 0.659$ (green square) and the most dense jammed state, $\phi_{J\,\mathrm{max}} = 0.842$, (blue square). The thermodynamically inaccessible exist below ϕ^*_J and the least dense state $\phi_{J\,\mathrm{min}} = 0.561$ (red square).

width of the distribution collapses to a single state, in the limit $H_d/\sigma \to 1$, when the system effectively becomes one–dimensional. The distribution broadens as H_d increases, but $\phi_{J\,\mathrm{max}}$ and $\phi_{J\,\mathrm{min}}$ go through minima due to the varying lengths l_{i1} and l_{i3}. The range of jammed states from $\phi_{J\,\mathrm{max}} - \phi_{J\,\mathrm{min}}$ represents the J–line.

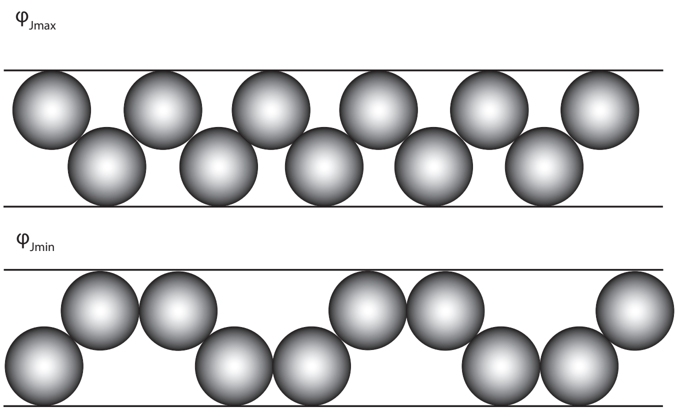

Figure 3.3: Top: most dense ($\phi_{J\,\mathrm{max}}$) Bottom: least dense ($\phi_{J\,\mathrm{min}}$) structures for the system.

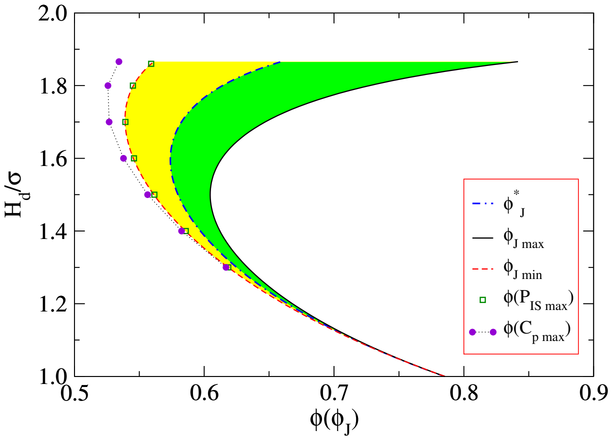

Figure 3.4: The jamming phase diagram showing $\phi_{J\,\max}$, $\phi_{J\,\min}$ and ϕ_J^* as a function of H_d/σ. The ϕ of the maxima for the inherent structure pressure, P_{IS}, and the heat capacity, C_p, are included for comparison. The green area identifies the accessible jammed packings and the yellow area represents the inaccessible jammed packings.

3.5 Thermodynamics of the Equilibrium Liquids

The goal of this section is to investigate how the thermodynamics of the equilibrium fluid are related to the underlying inherent structure landscape.

3.5.1 Transfer Matrix Method

Barker [167] originally provided an exact solution for the partition function of quasi–one dimensional systems. Kofke *et al.* [151] then developed a transfer matrix method for solving the partition function of a system of hard particles in a channel, where second nearest neighbor interactions are excluded. In this approach, the y positions of the particles are fixed so the system becomes a 1d mixture of additive hard rods with different contact lengths. This allows the integration over the x coordinates of the particles to be performed independently of the integration of the y coordinates. The solution to the partition function can then be represented as an eigenvalue problem where the largest eigenvalue is used in the thermodynamic limit. The partition function in the N, P_L, T ensemble can be written as a transfer integral,

$$Z = \frac{1}{\Lambda^{dN}\left(\beta P_L\right)^{N+1}} \int dy K^N\left(y_1, y_2\right). \tag{3.10}$$

Here, Λ is the thermal wavelength, P_L is the longitudinal pressure and the kernel K is defined as:

$$K(y_1, y_2) = \exp\left[-P_L h_0 L_x(y_1, y_2)\right], \tag{3.11}$$

with y_1 and y_2 being the y–coordinates of two adjacent discs in contact. L_x is the projection of the distance between the two contacting discs along the x–axis and is a function of y_1, y_2. In principal, $K(y_1, y_2)$ is an indefinite matrix because y_1 and y_2 are continuous variables but at the thermodynamics limit it is only the largest eigenvalue, λ, which is important and satisfies,

$$\int dy K(y_1, y)\,\psi(y) = \lambda\psi(y_1), \tag{3.12}$$

where ψ is an eigenfunction. This is solved numerically by constructing a mesh in the y–coordinate with unit size $\delta = (H_d - \sigma)/N_d$ where $N_d = 500$ is the number of divisions used in this analysis. Eq. 3.12 then becomes,

$$K(y_i, y_j) = \exp\left[-\beta P_L L_x(y_i, y_j)\right], \tag{3.13}$$

where $L_x(y_i, y_j) = \sqrt{[\sigma^2 - L_y(y_i, y_j)^2]}$ and $L_y(y_i, y_j) = (i - j)\,\delta$. The Gibbs free energy, g, is then given by,

$$\beta g = \ln \Lambda + \ln(\beta P_L) - \ln(\lambda), \tag{3.14}$$

and for a given pressure, the volume of the system can be obtained from,

$$V = (\partial g / \partial P_L)_{N,T}, \tag{3.15}$$

where it should be noted that the eigenvalue is a function of P_L. Figure 3.5 shows the results obtained using this method for different values of channel widths. The EOS obtained from this method shows a very good agreement with simulated results.

3.5.2 Mapping Configurations to Inherent Structures

The information contained within the matrix K regarding the geometry of adjacent tangent discs can be used to determine which inherent structures are sampled by the equilibrium fluid as a function of density. Starting from an equilibrium configuration, the discs needed to be translated along the x axis, keeping the y–coordinate fixed, so that the discs are in contact with their nearest neighbors. Figure 3.6 shows that the type of bond formed between the two central discs (mn) as the result of further compression can be determined from the sign of the

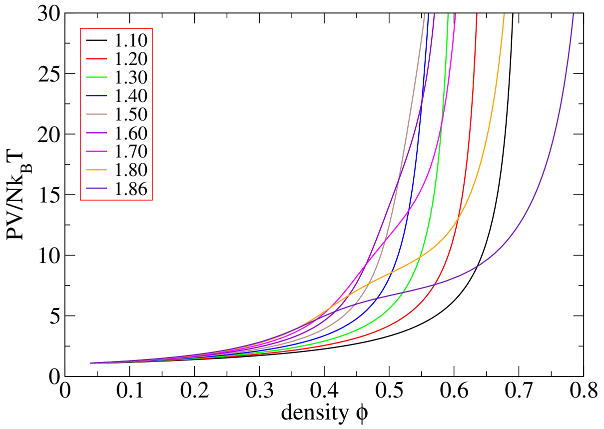

Figure 3.5: The EOS for different values of channel diameters H_d/σ.

product of areas made from the triangles created by particles i, m, n and m, n, j. The geometry of the four discs is contained in the chain product matrix $K(y_i, y_m)\,K(y_m, y_n)\,K(y_n, y_j)$. The product *area–vector–product* rule, for triangles $\overrightarrow{\Delta}_{imn}$ and $\overrightarrow{\Delta}_{mnj}$, that determine the nature of the bonds is

$$\begin{array}{ll} \overrightarrow{\Delta}_{imn} \cdot \overrightarrow{\Delta}_{mnj} > 0 & \text{bond mn } \Delta^{x}_{ij}(mn) = l_{k,1} \\ \overrightarrow{\Delta}_{imn} \cdot \overrightarrow{\Delta}_{mnj} < 0 & \text{bond mn } \Delta^{x}_{ij}(mn) = \sigma \end{array}. \tag{3.16}$$

The four particle transfer matrix can be defined then as,

$$G_4(i_1, i_4) = \sum\nolimits_{i=i_2,i_3} K(i_1, i_2)\,K(i_2, i_3)\,K(i_3, i_4)\exp\left[\gamma \Delta^{ij}_{x}(mn)\right], \tag{3.17}$$

whose elements are weighted by the bonds they would form when jammed. In this equation, γ is the thermodynamics conjugate variable for Δ^{ij}_{x}. For a system with periodic boundary conditions and $N-2$ particles, the volume of the inherent structure formed when the equilibrium fluid is at P_L, is given by,

$$V^{inh}_{N-2} = \lim\nolimits_{\gamma\to 0} \partial \log\left[\mathrm{Tr}\left(G_4\right)\right]/\partial\gamma. \tag{3.18}$$

The same approach can be used to obtain the fraction of defects in the inherent structure sampled by the fluid, $\theta(\phi)$, by setting $\Delta^{x}_{ij}(mn)$ equal to 1 and 0 for the defect states and dense states respectively and then using Eq. 3.18. Figure 3.7 shows θ as a function of ϕ for a system with $H_d/\sigma = 1 + \sqrt{3/4}$. The analytical results matche perfectly with the simulation

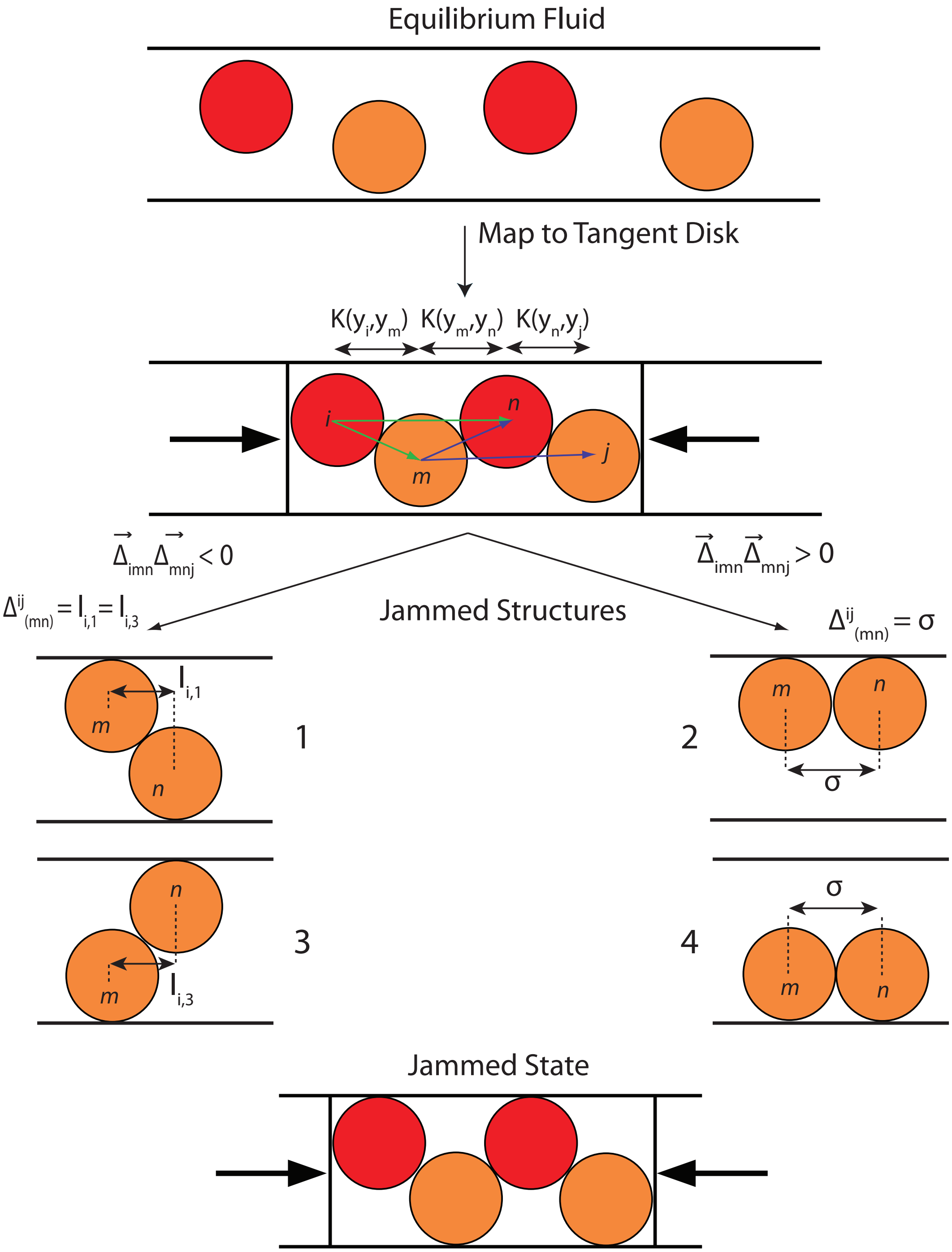

Figure 3.6: Analytical quench connecting equilibrium fluid configurations of discs i, m, n, j to the most dense (1, 3) and least dense (2, 4) local packing arrangements. Equilibrium configuration of four discs are initially mapped to a tangent disc configuration by compression in the x axis. The product of the kernel $K(y_i, y_j)$ and the dot product of vectors (Eq 3.16) maps the central discs to their jammed configuration. See text for more details.

which is described later in section 3.6.1. Figure 3.8 shows θ for different channel diameters. The configurational entropy of the equilibrium fluid, $S_c(\phi)$, is then obtained by using $\theta(\phi)$ in Eq. 3.8. Figure 3.9 shows the S_c as a function of ϕ for different values of H_d/σ. In particular, it can be seen that the ideal gas samples the inherent structures at the maximum of the distribution, ϕ_J^*, then the fluid moves to basins with a higher ϕ_J with increasing density. The basins with $\phi_J < \phi_J^*$ are never sampled by the equilibrium fluid. At low ϕ, the configurational entropy of the fluid decreases slowly before it begins a rapid decrease at intermediate occupied volume fractions. An extrapolation of the S_c to higher ϕ, based on its behavior in this intermediate regime, would suggest the system exhibits a Kauzmann catastrophe where the configurational entropy goes to zero at a ϕ well below $\phi_{J\,\mathrm{max}}$. However, S_c plateaus at high ϕ and only approaches zero in the limit $\phi \to \phi_{J\,\mathrm{max}}$. As a result, there is no ideal glass transition in this system.

3.5.3 Defect–Defect Interactions

There is considerable evidence to suggest that the higher order saddle points, connecting the basins of the stable states, also play an important role in the dynamics and structural relaxation of the supercooled fluids [168, 169]. In a system with potential energy, saddle points can be classified on the basis of the number of negative eigenvalues in the Hessian matrix of the potential energy of the configuration. When there are no negative eigenvalues, the saddle point is a stable inherent structure, otherwise the system contains one or more unstable, "soft" modes. A statistical measure of these saddle points is captured by the saddle point index, which is the average number of negative eigenvalues in the liquid [170,171]. The saddle point index has been shown to decrease with temperature below the onset temperature for the Kob–Andersen binary Lennard–Jones mixture (KA BLJM) [172], and go to zero at a finite temperature, T_d, very close to the mode coupling critical temperature. A crossover from fragile to strong liquid behavior also occurs at T_d [126] in the KA BMLJ model.

The Hessian matrix cannot be calculated in a hard particle system. However, the local unstable modes in this models can be identified as those associated with neighboring defects, i.e. with $-1-4-4-3-$ and $-3-2-2-1-$ bond configurations. Building on the method for mapping configurations to their local inherent structures, one can use the transfer matrix approach to map clusters of five discs to their local structure and calculate the probability

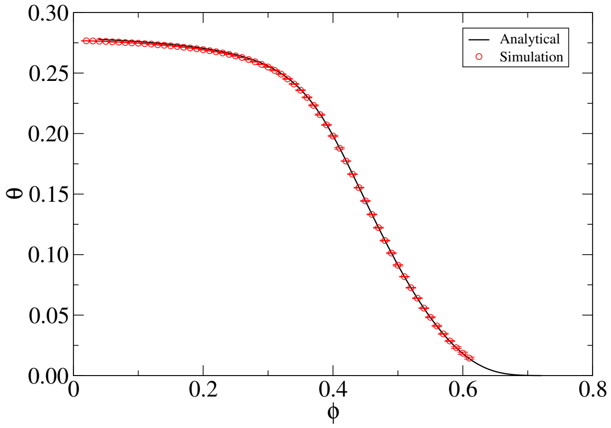

Figure 3.7: The fraction of defect bonds in the inherent structures sampled by equilibrium fluid at ϕ. The solid line represents the transfer matrix results and the open circles were obtained from simulation (see Section 3.6.1)

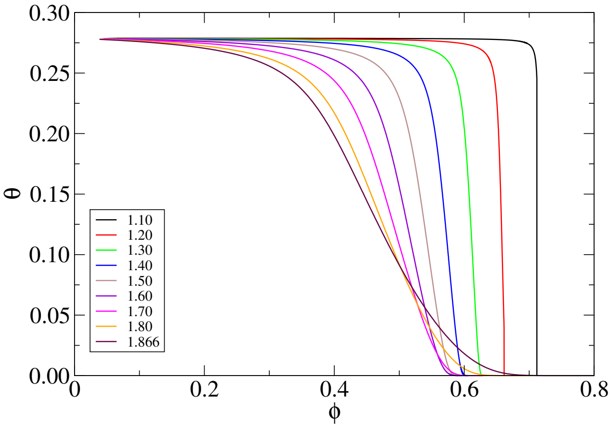

Figure 3.8: The fraction of defect bonds in the inherent structures sampled by equilibrium fluid at ϕ for different values of channel diameters H_d/σ.

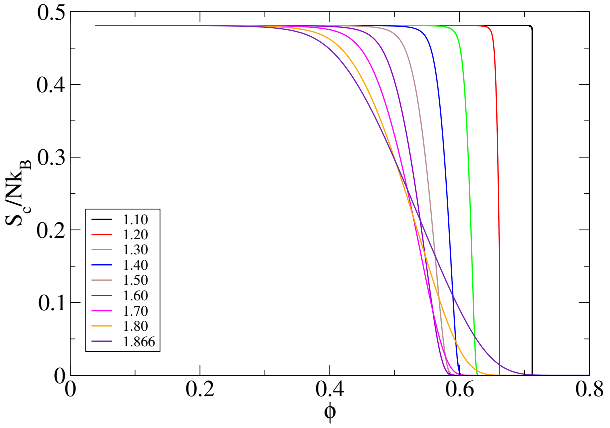

Figure 3.9: The configurational entropy of the equilibrium fluid for different values of channel diameters H_d/σ.

of finding the unstable states. A configuration of five discs is initially compressed along the x–axis, with y–coordinates held fixed, until all the discs are in contact with their neighbors. The unstable states are then can identified using the triangle rules for neighboring particles to define Δ_5 as

$$\begin{aligned}
&\vec{\Delta}_{123} \cdot \vec{\Delta}_{234} < 0 \quad \vec{\Delta}_{234} \cdot \vec{\Delta}_{345} < 0 \quad \Rightarrow \Delta_5 = 1, \\
&\vec{\Delta}_{123} \cdot \vec{\Delta}_{234} > 0 \quad \vec{\Delta}_{234} \cdot \vec{\Delta}_{345} < 0 \quad \Rightarrow \Delta_5 = 0, \\
&\vec{\Delta}_{123} \cdot \vec{\Delta}_{234} < 0 \quad \vec{\Delta}_{234} \cdot \vec{\Delta}_{345} > 0 \quad \Rightarrow \Delta_5 = 0, \\
&\vec{\Delta}_{123} \cdot \vec{\Delta}_{234} > 0 \quad \vec{\Delta}_{234} \cdot \vec{\Delta}_{345} > 0 \quad \Rightarrow \Delta_5 = 0.
\end{aligned} \tag{3.19}$$

Once the five particle transfer matrix is defined,

$$G_5(y_1, y_5) = \sum_{y_2, y_3, y_4} K\left(y_1, y_2\right) K\left(y_2, y_3\right) K\left(y_3, y_4\right) K\left(y_4, y_5\right) \exp\left[\omega \Delta_5\right], \tag{3.20}$$

the fraction of configuration space associated with the unstable states ($\Delta_5 = 1$) is given by,

$$\eta = \lim_{\omega \to 0} \partial \left[\log \mathrm{Tr}(G_5\right] / \partial \omega. \tag{3.21}$$

Here, ω is the thermodynamics conjugate variable for Δ_5. RMFT identifies ϕ_d as the occupied volume fraction where long lasting glassy states first appear, causing the dynamics to become activated. In the bulk, three dimensional hard sphere system, $\phi_d \sim 0.58$, which coincides with the mode coupling transition. Godfrey and Moore [154] found the correlation length for the confined discs model increased rapidly at intermediate ϕ and would appear to diverge near $\phi = \phi_d \sim 0.48$ based on an extrapolation. However, the transition is avoided and the growth of the correlation length slows down at higher ϕ. Figure 3.10 shows that the analysis of η essentially follows that of the inverse correlation length obtained by Godfrey and Moore, decreasing rapidly before plateauing at very low values ($\eta \sim 0$). A linear extrapolation from lower ϕ would locate $\phi_d \sim 0.5$. This suggests a change in the nature of the dynamics may occur when defects becomes rare, such they do not interact to produce soft modes. In principle, the analysis of higher order saddle point that include states $-2-2-2-$, $-2-2-2-2-$ and etc should be included, but these are even more rare and their inclusion would not change the qualitative features described here.

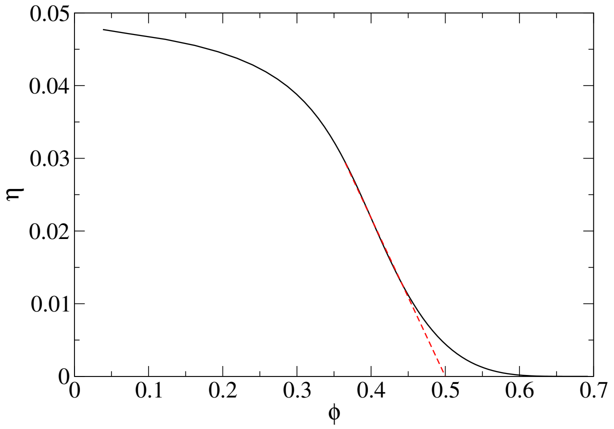

Figure 3.10: η as a function of ϕ. The solid line represents data calculated using the transfer matrix method. The dashed line is the linear extrapolation.

3.5.4 Heat Capacity

The isobaric heat capacity is $C_p = (\partial H/\partial T)_P$. For hard discs, the enthalpy is $H = Nk_\mathrm{B}T + PV$ and,

$$C_p/Nk_\mathrm{B} = 1 + (PV/Nk_\mathrm{B}T) / (1 + d\ln\{PV/Nk_\mathrm{B}T\} / d\ln\{\phi\}), \tag{3.22}$$

where V is the thermodynamic volume accessible to the centers of the particles. Figure 3.11 shows that the fluid exhibits a maximum in the heat capacity that sharpens and moves to lower T as the distribution of inherent structures narrows with decreasing H_d, before collapsing to a single structure at $H_d/\sigma = 1$. For the system with $H_d/\sigma = 1 + \sqrt{3/4}$, the maximum is located at $\phi = 0.534$, which is only just above ϕ_d. If C_p is replotted as a function of equilibrium number of defects in the fluid (see Fig. 3.12), it can be seen that the maximum occurs at the same value, $\theta = 0.044 \pm 0.002$ for all H_d, suggesting the concentration of defects is the key feature controlling the behavior of the heat capacity maximum.

3.5.5 Inherent Structure Pressure

Shell and Debenedetti [173] showed that the properties of the EOS of a fluid could be related to the inherent structure landscape by separating the equilibrium pressure into contributions

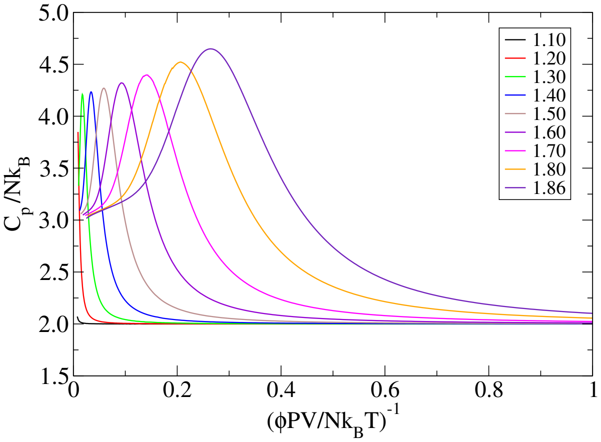

Figure 3.11: C_p/Nk_B as a function of $(\phi PV/Nk_\mathrm{B}T)^{-1}$.

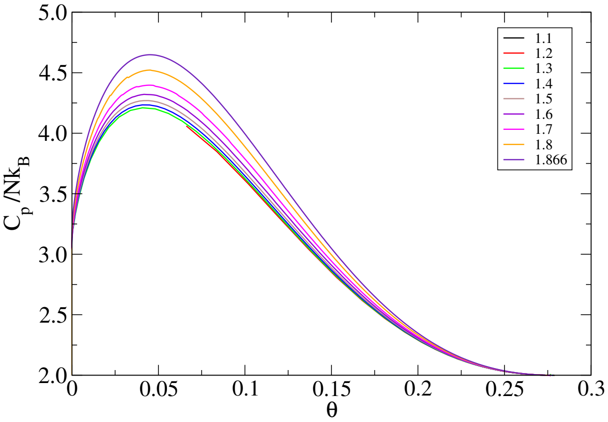

Figure 3.12: C_p/Nk_B as a function of defect fraction θ.

from the inherent structure pressure, P_{IS}, and vibrational pressure, P_{vib}, so that,

$$P = (P_{IS} + P_{vib})\,. \tag{3.23}$$

Making use of the general relation $P = T(\partial S/\partial V)_U$, the inherent structure pressure can be calculated as,

$$\beta P_{IS} h_0 \sigma^2 = -\frac{4H_d\phi^2}{\pi}\left(\frac{\partial S_c/Nk_\mathrm{B}}{\partial \phi}\right)_U, \tag{3.24}$$

and then P_{vib} can be obtained from Eq. 3.23. The vibrational and inherent structure contributions to the pressure are shown in Figs. 3.13 and 3.14 respectively. The vibrational pressure increases monotonically as a function of ϕ while P_{IS} exhibits a maximum at densities that are slightly higher than the where the C_p maximum appears. The location of the maxima in the heat capacity and the inherent structure pressure have been included on the jamming phase diagram for the model (Fig. 3.4).

3.6 Molecular Dynamics Simulations

In this section, a series of event driven molecular dynamics simulations carried out in the canonical (N, V, T) ensemble will be described. They help verify the transfer matrix analysis and provide measurements of the dynamic properties of the system. $N = 10^4$ particles were initially placed in a linear lattice at $\phi = 0.01$, and were assigned random velocities that were then scaled to ensure $k_\mathrm{B}T = 1$. The units of time in the simulation are $\sigma\sqrt{m/k_\mathrm{B}T}$, where m

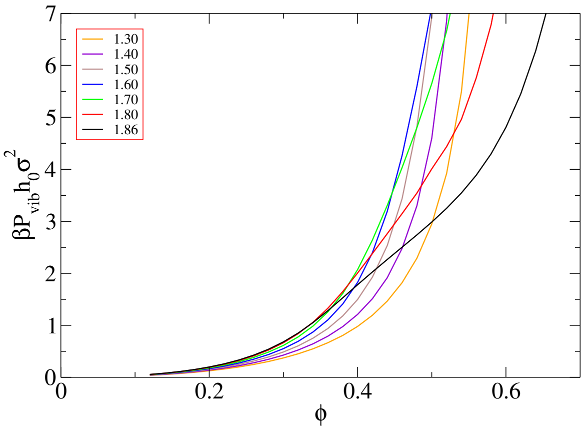

Figure 3.13: The vibrational pressure of the system as a function of packing fraction.

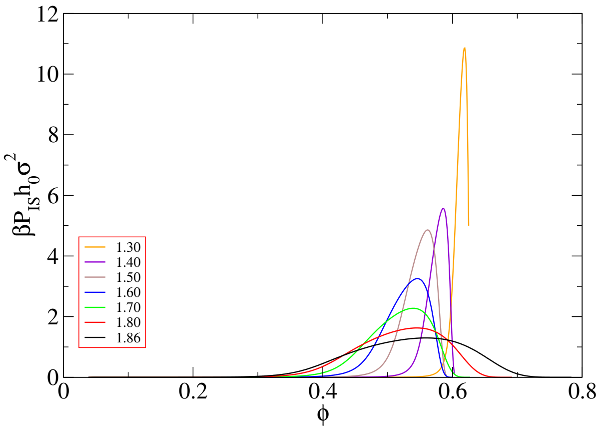

Figure 3.14: The inherent structure pressure of the system as a function of packing fraction.

is the mass of the particles, which was taken to be unity. At each density studied, the system was equilibrated for $200N - 10^6 N$ collisions before sampling over the next $400N - 10^7 N$ collisions, with the longer run times being used at high densities. A modified version of the Lubachevsky and Stillinger [76] (LS) algorithm that ensures H_d/σ remains constant as the diameter of the discs is changed (L fixed) was used to compress the system to higher occupied volume fractions, with a compression rate of $d\sigma/dt = 0.001$.

3.6.1 Exploring the Packing Landscape

The EOS obtained from the simulations matches the exact result within simulation error up to very high occupied volume fractions where finally the system falls out of equilibrium at the longest time scales used in the simulations. This occurred near $\phi \sim 0.8$ with $H_d/\sigma = 1 + \sqrt{3/4}$.

To follow how the equilibrium liquid moves through the packing landscape as a function of ϕ and compare the simulations with the transfer matrix inherent structure mapping, the defect concentration in the fluid was measured using the triangular method introduced by Speedy [71]. In this method, the position of each disc is considered relative to its two neighbors. If the central disc is located below the line connecting its two neighbors, it will pack at the bottom of the channel, otherwise it will pack at the top. The configuration is then assigned bond numbers, equivalent to those described in Fig. 3.1, allowing to identify

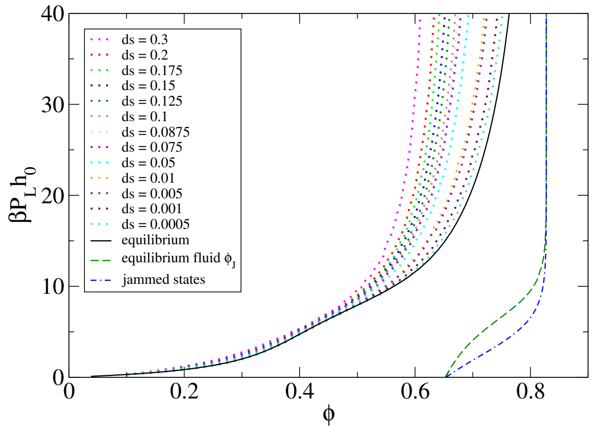

Figure 3.15: EOS for $H/\sigma = 1 + \sqrt{3/4}$. EOS for granular ensemble: $\beta P_L h_0$ as a function of ϕ_J (blue dot–dashed line). EOS for equilibrium thermal fluid: $\beta P_L h_0$ as a function of ϕ (black solid line). ϕ_J of basins sampled by equilibrium fluid (green dashed line). EOS for fluid compressed using LS method with different $\partial\sigma/\partial t$ (dotted lines).

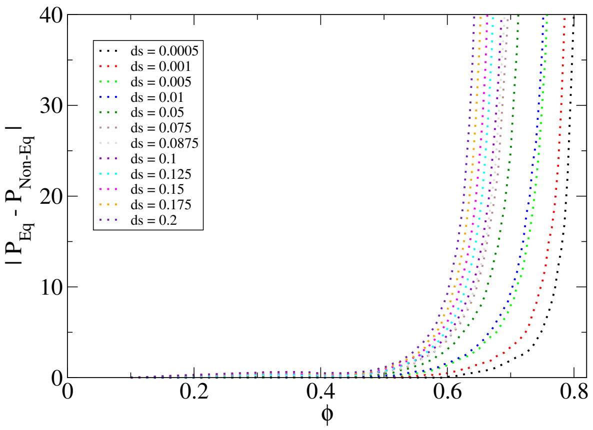

Figure 3.16: The difference between the equilibrium EOS and the non-equilibrium EOS as a function of ϕ, with $H_d/\sigma = 1 + \sqrt{3/4}$, for different compression rates.

defects in liquid state without having to compress the system to a jammed state. Figure 3.7 shows that the defect concentration obtained from simulations is the same as that obtained using the transfer matrix inherent structure mapping.

MD simulations are used to explore how the fluid falls out of equilibrium by following the non–equilibrium EOS of the fluid as it is continually compressed. The simulations started at $\phi = 0.05$ and the system was compressed to its jammed configuration using the LS method, with different compression rates in the range $d\sigma/dt = 0.0005 - 0.3$. The non–equilibrium pressure, at a given density, was obtained by measuring the disc–disc and disc–wall momentum transfer over $10N$ collisions, as the system was still being compressed. Figure 3.15 shows the non–equilibrium pressures and the equilibrium pressure obtained from the transfer matrix method for the case with $H_d/\sigma = 1 + \sqrt{3/4}$. Figure 3.16 shows the difference between the non–equilibrium EOS and the equilibrium EOS, dotted lines and black solid line in Fig. 3.15 respectively. At low ϕ, the non–equilibrium EOS essentially follows that of the equilibrium system because the motion of the particles allows it to move between basins and relax as the fluid is compressed. The small positive differences result from the continual increase in ϕ as the pressure measurement is made, and this occurs more rapidly at faster compression

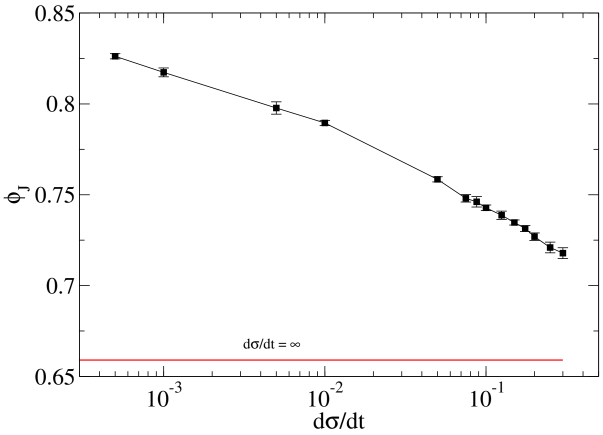

Figure 3.17: ϕ_J as a function of $\partial\sigma/\partial t$

rates. At the fastest compression rates considered here, the system falls out of equilibrium at $\phi \sim 0.5$, as the non–equilibrium EOS begins to diverge, leading to a jammed state with $\phi_J \sim 0.72$ (see Fig. 3.17). It is interesting to note that the system first shows signs of falling out of equilibrium at a ϕ close to the ϕ_d identified using the saddle point index. As the compression rate is decreased, the fluid remains in equilibrium longer and becomes trapped in a glass with a higher ϕ_J. In principle, if the system was compressed infinitely slowly, it would remain in equilibrium and become jammed at $\phi_{J\,\mathrm{max}}$. Godfrey and Moore [154] were able to predict the compression rate dependence of ϕ_J on the basis of a transition state theory that estimates the time for two defects to diffuse together and annihilate each other through one of the unstable saddle points. Once the rate of compression is faster than than of the rate of annihilation, the total number of defects becomes fixed and system falls out of equilibrium. The transition state theory was also able to predict the time associated with particles hopping in defects obtained from molecular dynamics simulations [86].

Based on the transition state picture by Godfrey and Moore [154], in this system the defect state is stable and there is a barrier which system has to pass to go into different configuration (Fig. 3.18). In this figure, the defect can move when one disc crosses the channel by squeezing between its neighbors: the system passes through the transition state shown in the middle diagram to reach the defect state shown in the bottom diagram.

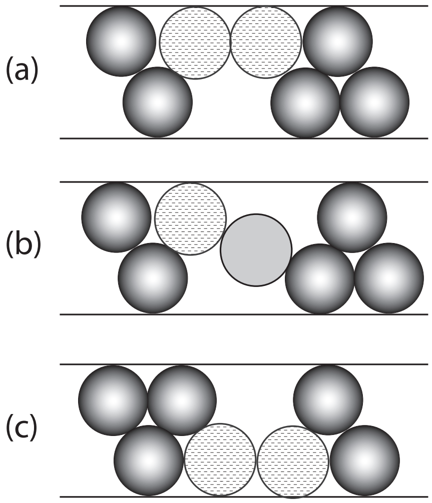

Figure 3.18: The transition state for motion of a defect: a disc in a stable defect state (a) moves through a transition state (b) as it hops to another stable state (c) (adapted from [154]).

3.6.2 Free Volume Equation of State

Near the jamming density, the particles are caged by neighbors and remain trapped in local inherent structure basins. As a result, the EOS of the glass should be described by a free volume equation of state [174] that diverges at the ϕ_J of the inherent structure. This can be tested and the free volume EOS can be used to obtain ϕ_J.

This is especially important for those jammed states below ϕ_J^*, since the system is not able to sample them from equilibrium fluid. The free volume EOS is defined as:

$$p = \frac{PV}{Nk_{\mathrm{B}}T} = \frac{1}{\delta} = \frac{d}{1-\phi/\phi_J}, \tag{3.25}$$

where d is the dimensionality of the system and ϕ_J is the density of the inherent structure which the system samples. This equation can be used to give an estimate of $\phi_J \simeq \phi/\left(1-d/p\right)$ of the jamming density. Configurations were prepared in their jammed state with a known number of defects randomly distributed throughout the configuration, but such that there are no defect pairs. The ϕ_J for these configurations is then known from equation 3.9. Figure 3.19 shows relation 3.25 for some of the jammed configurations were obtained while the systems decompressed slowly from the densities below their actual jammed point until an unjamming particle rearrangement occurs. The slope of the lines reproduces the dimensionality of the system.

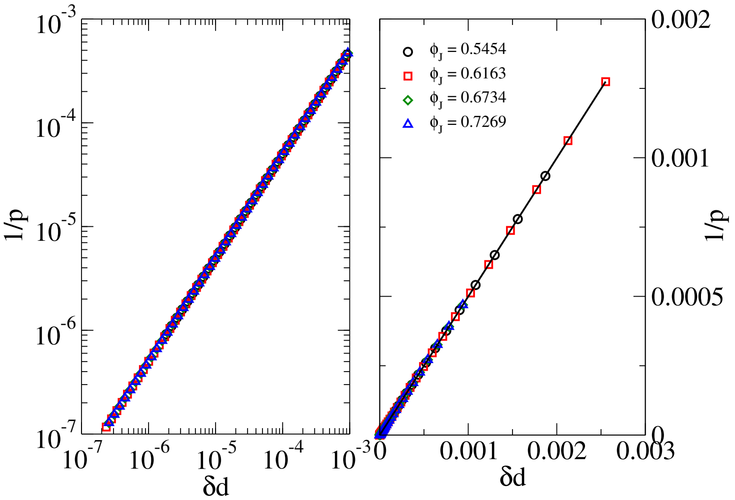

Figure 3.19: The Free Volume EOS for the systems of jammed states.

3.6.3 Relaxation Times

To study the relationship between the packing landscape and the dynamics of the fluid, the structural relaxation time was calculated for the system over a range of ϕ, using two different methods. All simulations used $N = 2000$ particles. Starting from $\phi = 0.01$, between $400N - 10^6 N$ collisions were used to reach equilibrium, then the relaxation times were measured with simulation lengths that varied from $200N$ up to $10^6 N$, depending on the occupied volume fraction. 8×10^4 equally spaced configurations were sampled at each ϕ.

First the measurement of the relaxation time defined in terms of the intermediate scattering function will be explained. The longitudinal structure factor for the system can be defined as,

$$S(\mathbf{k}) = \frac{1}{N} \langle \rho_{\mathbf{k}} \rho_{-\mathbf{k}} \rangle \,, \tag{3.26}$$

where

$$\rho_{\mathbf{k}} = \sum_{j=1}^{N} \exp\left[-i\mathbf{k} \cdot \mathbf{r}_{xj}(t)\right], \tag{3.27}$$

$\mathbf{r}_{xj}$ is the position of particle j along the x–coordinate, at time t, and the angular brackets denotes an equilibrium ensemble average over multiple configurations at different t. The wave vectors $\mathbf{k}$ were defined along the x–axis, as $\mathbf{k} = 2\pi n/L_x$ and the integers n were chosen in the

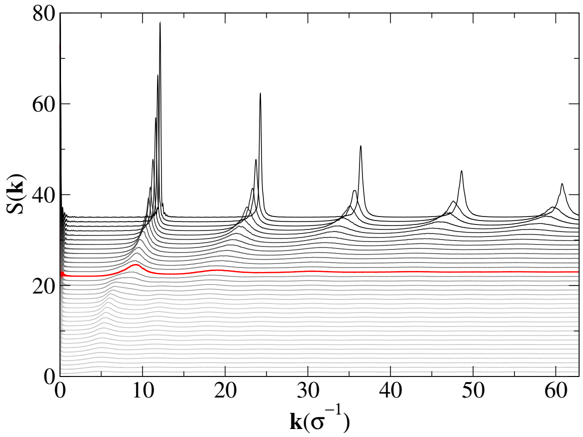

Figure 3.20: Structure factor $S(\mathbf{k})$ for all ϕ investigated with $H_d/\sigma = 1 + \sqrt{3/4}$. For clarity the individual curves have been displaced vertically by 1 with increasing ϕ. The red curve highlights the data for $\phi = 0.534$, corresponding to the ϕ of the C_p maximum.

range $1-60$. Figure 3.20 shows the evolution of $S(\mathbf{k})$ as a function of ϕ. The emergence of the first peak, at small $\mathbf{k}$, reflects the growth in real space of the regular zig–zag arrangements of the particles associated with the most dense packing. In particular, a rapid but still continuous, shift of the peak to larger $\mathbf{k}$ can be seen at ϕ near the C_p maximum. Significant structural changes from a fluid–like to a solid–like structure have also been observed in the pair correlation function at these ϕ [152, 153].

The structural relaxation time for the system was then obtained by measuring the self part of the intermediate scattering function,

$$F_s\left(\mathbf{k},t\right) = \frac{1}{N}\left\langle \rho_{\mathbf{k}}(t)\rho_{-\mathbf{k}}(0)\right\rangle , \tag{3.28}$$

at the wave vector, $\mathbf{k}_{\mathrm{max}}$, corresponding to the peak of the first maximum in S($\mathbf{k}$). Figure 3.21 shows that the decay of $F(\mathbf{k}_{\mathrm{max}}, t)$ is missing the shoulder characteristic of supercooled liquids, and the decay of this quantity to zero suggests the system behaves like an equilibrium fluid for all ϕ studied. The structural relaxation time, τ_F, was then defined as the time required for $F(\mathbf{k}_{\mathrm{max}}, t)$ to fall to e^{-1} of its initial value. For a hard particle system, ϕPV is a constant along an isobar and the Arrhenius law would predict that $\ln \tau_F$ varies linearly with $\phi PV/Nk_{\mathrm{B}}T$. Figure 3.22 shows τ_F is linear in $1/T$, at high ϕ, which is the behavior expected for a strong fluid, but at lower ϕ, the temperature dependence becomes less clear. In particular, with

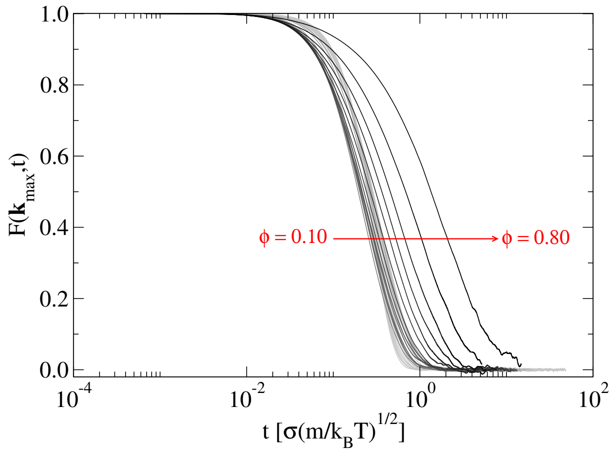

Figure 3.21: The time dependance of the self intermediate structure factor,$F(\mathbf{k}_{\mathrm{max}}, t)$ for a system with $H_d/\sigma = 1 + \sqrt{3/4}$, over a range of ϕ.

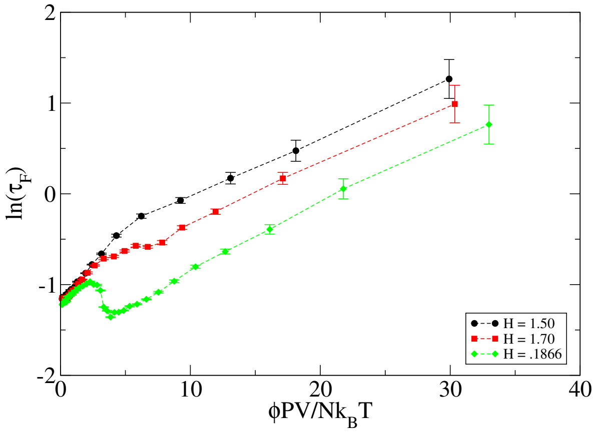

Figure 3.22: Arrhenius plot for the relaxation times obtained from self intermediate function for different values of H_d/σ.

$H_d/\sigma = 1 + \sqrt{3/4}$, an unusual decrease in the relaxation times can be seen. This may be caused by the rapid structural evolution of the system at these ϕ and is complicated by the corresponding variation of $\mathbf{k}_{\mathrm{max}}$.

As an alternative, a relaxation time was also measured based on the the survival probability of the bond types used to describe the local packing in the inherent structures. At $t = 0$, Speedy's triangular method, described earlier, was used to identify the local bond types throughout the configuration. The fluid remains within the basin of a single inherent structure for a short time before a local rearrangement of the discs changes the identity of some of the bonds and moves the system to a new inherent structure. $R(t)$, the fraction of bonds that have not changed at least once in time t as a function of t was measured. The relaxation time was then defined as,

$$\tau = \int_0^\infty R(t)\, dt. \tag{3.29}$$

$R(t)$ decays the same fashion as $F(\mathbf{k}_{\mathrm{max}}, t)$ (see Fig. 3.23), but τ now is well behaved over the full range of ϕ studied (see Fig. 3.24). The linear behavior in $1/T$ at high ϕ remains, but it can be seen the fluid exhibits a super–Arrhenius behavior at low ϕ, suggesting the system has a fragile–strong fluid crossover. It is also shows fits of the data from the fragile region to the Vogel–Fulcher–Tammann (VFT) equation [12–14], which predicts a divergence of the relaxation times at a temperature $T_{VFT} > 0$ K, along with the parabolic law developed by

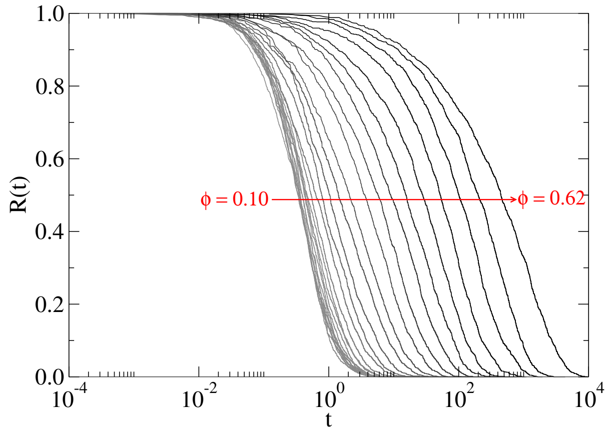

Figure 3.23: The time dependance of the bond survival probability $R(t)$ for a system with $H_d/\sigma = 1 + \sqrt{3/4}$, over a range of ϕ.

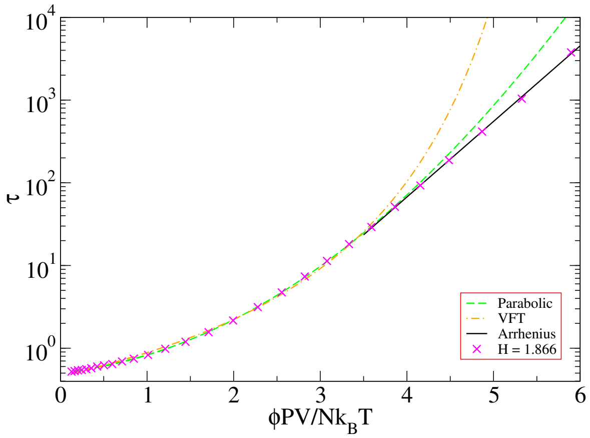

Figure 3.24: Arrhenius plot for the relaxation time for $H_d/\sigma = 1 + \sqrt{3/4}$. The dashed and dashed–dotted lines represent fits to the data in the fragile region of the parabolic and VFT equations, respectively. The solid line is the Arrhenius fit to the strong fluid region.

Elmatad, Chandler, and Garrahan [17, 175], which predicts no singularity and is derived on the basis of the facilitated dynamics model [57]. Both equations fit well when restricted to the fragile fluid data (as shown), but the fits become worse when extended over full range of data. The Arrhenius equation provides the best fit for τ above the crossover. Good fits of the VFT equation to a wide range of experimental and simulation data for supercooled liquids have been used as evidence for the presence of a thermodynamic singularity underlying the experimentally observed glass transition. However, its been already shown that this model does not exhibit an ideal glass transition, which suggests that T_{VFT} is simply a fit parameter with no physical significance.

To further confirm the existence of the fragile–strong crossover, the fragility parameter [11] is also calculated,

$$m_f = \left(\frac{d \log \tau}{d \left(\frac{1}{T} \right)} \right), \tag{3.30}$$

where the derivatives were obtained directly from the data points, without any curve fitting, using a centered differences scheme. Figure 3.25 shows m_f increases linearly at high temperatures but then plateaus to a constant value when the fluid becomes strong. The crossover point occurs at the C_p maximum.

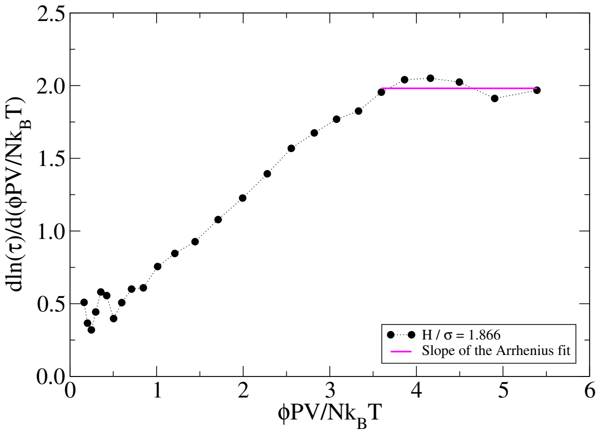

Figure 3.25: The derivation of the logarithmic relaxation time τ is plotted against $1/T$ for $H_d/\sigma = 1 + \sqrt{3/4}$.

Figure 3.26 shows the relaxation time measured for different channel diameters. A comparison of the glass forming properties of different systems is usually achieved by the rescaling of the temperature of the system by the glass transition temperature, T_g, which is defined as the temperature where the relaxation time of the system reaches a given value, τ_g. To compare the relaxation times of systems with different channel diameters, $\tau_g = 40.2$ was defined, by choosing the longest relaxation time accessible to all the systems studied, then the temperature of each system is rescaled by the corresponding T_g (Figure 3.27). With such a scaling, all the systems appear to have different fragilities. However, the FS crossover occurs at the same value of ϕ as the maximum in the C_p, for all channel diameters, which suggests there is an alternative scaling temperature. For each H_d/σ, the temperature of the C_p maximum was located, $T_{\max}$, using the thermodynamic analysis, and defining τ_0 as the relaxation time at $T_{\max}$. By rescaling the temperatures and relaxation times by $T_{\max}$ and τ_0 respectively, it is found that all the data now collapses onto a single master curve (see Fig. 3.28). This suggests that the temperature at the C_p maximum provides a more meaningful, and physically motivated, scaling temperature for this model than an arbitrarily selected glass transition transition temperature.

The FD model suggests that the fragile–strong crossover should be related to the concentration of excited regions. In this system, these excited regions can be identified as the

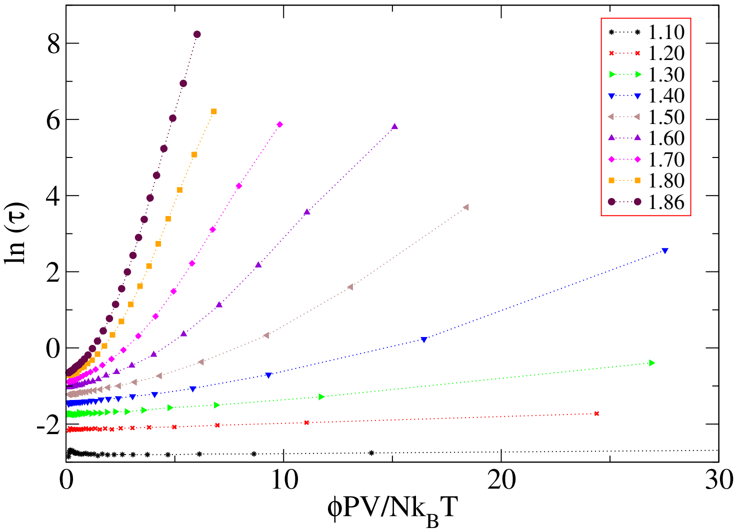

Figure 3.26: Structural relaxations time for different H_d/σ as a function of $\phi PV/Nk_\mathrm{B}T$.

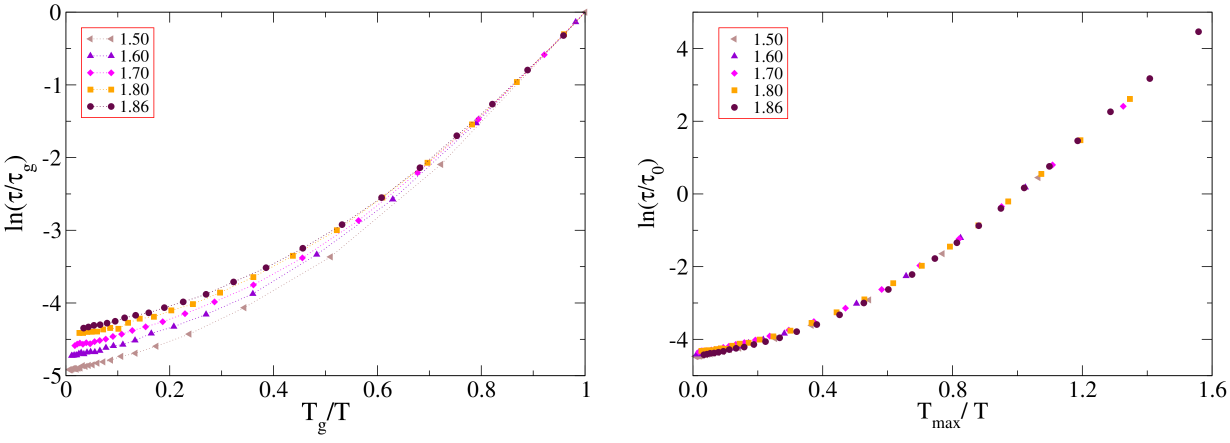

Figure 3.27: Structural relaxations time for different H_d/σ rescaled by the "glass transition" time and temperature (see text for definition).

Figure 3.28: Structural relaxations time for different H_d/σ rescaled by the time and temperature of the C_p maximum

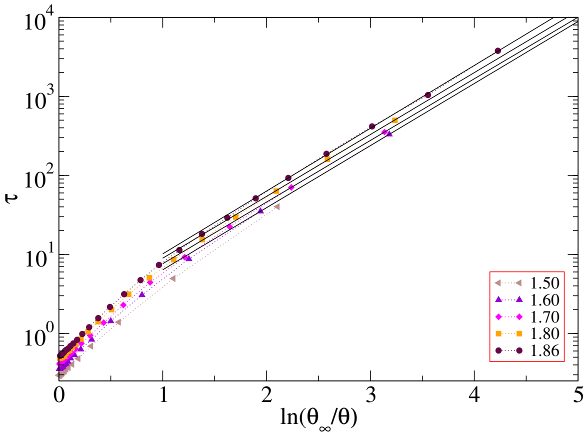

Figure 3.29: Structural relaxations times for different H_d/σ as a function of the defect concentration relative to the defect concentration in the ideal gas, θ_∞.The solid black lines are the Arrhenius fit.

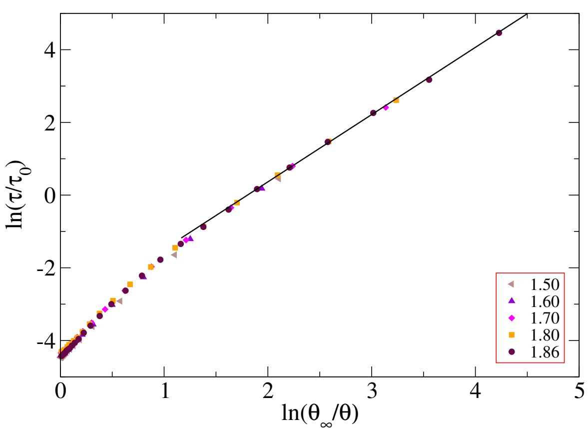

Figure 3.30: Structural relaxations times for different H_d/σ rescaled by the time and defect concentration of the C_p maximum as a function of the defect concentration relative to the defect concentration in the ideal gas, θ_∞. The solid black line is the Arrhenius fit.

defects because discs in the dense fluid regime can only move by hopping into the "vacancy" associated with a type 2 or type 4 local packing arrangements. At low ϕ, there is a high concentration of defects that can interact. When two defects are located next to each other, in a $-1-4-4-3-$ or $-3-2-2-1-$ arrangement, the local packing becomes unstable, which leads to directed, spontaneous and irreversible particle motions that annihilate the defects to form the stable $-1-3-1-3-$ arrangement. This cooperative particle motion is characteristic of a fragile fluid. Once the defect concentration drops below a critical concentration, structural relaxation occurs through the directionally independent, activated hopping of particles located in isolated defects, which is characteristic of a strong fluid. In the strong fluid regime $\ln\tau \sim \ln\theta$ which is confirmed in Fig. 3.29, at ϕ, above the C_p maximum. Figure 3.30 shows the rescaling the data by the C_p maximum makes them to collapse into single line.

3.6.4 Adam–Gibbs Relation

Having been able to calculate the configurational entropy for the system exactly and measure the relaxation times, the Adam–Gibbs relation can be checked for this model. A recent analysis [39, 176] of the Adam–Gibbs relation, in terms of the random first order transition

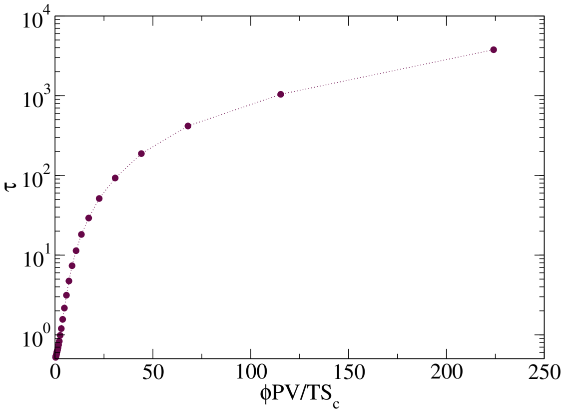

Figure 3.31: Adam-Gibbs plot for $H_d/\sigma = 1 + \sqrt{3/4}$.

theory [44, 177], suggests it has the general form,

$$\ln \tau \sim \left(\frac{\phi PV}{TS_c} \right)^{\alpha}, \tag{3.31}$$

where the value of α is dependent on the dimensionality of the system. The usual form of the Adam–Gibbs relation for three dimensions is recovered with $\alpha = 1$. Unfortunately, the Eq. 3.31 was not able to fit to the data, over any region, and Fig. 3.31 shows the results for the standard Adam–Gibbs relation. This is consistent with the work of Sengupta et al. [39, 176] who also found that the Adams–Gibbs relation did not work in two dimensions.

3.7 Discussion

The potential energy landscape, and its hard particle equivalent, provide one of the main paradigms used to understand the properties of liquids, glasses and jamming phenomena. However, the complexity of the landscape and the challenges associated with mapping configurations to their local inherent structures make it difficult to determine exactly how the thermodynamics and dynamics are related to the features of the landscape. The current work develops a comprehensive picture of these relationships for a model where both the landscape and the inherent structure mapping can be determined exactly.

A distribution of jammed states implies the existence of a J–line, as suggested by RMFT, rather than a particular J–point, but there are a number of interesting features in the landscape that can be connected to thermodynamic and dynamic properties of the fluid. In RMFT, ϕ_d represents the occupied volume fraction where the fluid begins to be trapped in the basins of long lasting glassy states. Configurations at ϕ_d map to ϕ_{th}, which terminates the J–line in the low ϕ_J limit. In this quasi–one dimensional hard disc model, ϕ_d was identified as the ϕ were the saddle point index becomes very low and the dynamics becomes activated. Dynamically, this is consistent with RMFT and MCT. However, the current work finds that the J–line extends well below ϕ_{th}. The ideal gas maps to the jammed states with ϕ_J^*, at the maximum of S_J, which marks the lowest ϕ_J accessible to the equilibrium fluid. If the fluid did sample states below ϕ_J^* it would be unable to satisfy the maximum entropy condition for equilibrium because $\partial S_J/\partial\phi_J > 0$ [128]. The inherent structure pressure would also become negative. From an operational perspective, the J–point was originally defined as the ϕ_J of jammed structures quenched from the ideal gas configurations, which in the current system is ϕ_J^*. While the jammed states below ϕ_J^* are inaccessible from a thermodynamic stand point, they may be formed through different compression protocols. Fluctuations in small systems will also allow these states to be observed. In general, the jamming phase diagram identified here looks similar to that proposed by Ciamarra et al. [105, 178] for a granular system, but here, a clear connection between the landscape and the equilibrium fluid was established.

The thermodynamic functions, C_p and P_{IS} both exhibit maxima as a function of ϕ that primarily result from the inflection in the S_c as the fluid moves toward the most dense state. The actual location of the maxima, and the inherent structure basins they are sampling, differ for each because the various thermodynamic functions are effected differently by the competition between the configurational and free volume contributions to the partition function. In particular, the coincidence between the location of the P_{IS} maximum and the $\phi_{J\,\mathrm{min}}$ appears fortuitous, rather than an indicator of a general thermodynamic relationship. For example, a binary system of non–additive hard rods exhibits a similar inherent structure landscape (see Chapter 2 and ref. [136]), but the maxima in the C_p and P_{IS} both occur at ϕ well above $\phi_{J\,\mathrm{min}}$ (Chapter 2), while the ideal gas configurations still maps to maximum in the distribution of the S_J.

Silica [119,120], silicon [121] and water [122–125] exhibit fragile–strong dynamical crossovers located at the C_p maximum associated with the Widom line while the KA BLJM system has also been shown to exhibit an FS crossover at the mode coupling temperature [126]. Mallance et al. [19] recently suggested an FS crossover temperature occurred in a broad range of glass forming liquids at temperatures below T_g. However, a subsequent analysis of some of the experimental data used in the Mallance et al. study showed that this was not the case [179]. This model clearly exhibits an FS crossover located at the C_p maximum as highlighted by both the curve fitting of a variety of different fragile behavior equations and by the derivative analysis shown in Fig. 3.25. Furthermore, it is been noted that the temperature of the C_p maximum provides a better, physically motivated, rescaling of the structural relaxation times for the various channel diameters than does an arbitrarily defined T_g.

Defects play an integral role in the dynamics of this quasi–one dimensional model and appear to establish a link between the dynamics and the thermodynamics, through the C_p maximum. In particular, neighboring defects are unstable and result in an irreversible local rearrangement of the particles, which appears to give rise to the super–Arrhenius dynamics of a fragile fluid. Once the defect concentration is low (the saddle point index is also low) the dynamics crosses over to the reversible hopping of defects between locally stable environments. Simulations of bulk materials have also shown that local soft modes are spatially correlated with the highly mobile particles connected to dynamic heterogeneities [180–182].

The particle rearrangements associated with defects provide a comprehensive picture for the structural relaxation dynamics of the current quasi–one dimensional hard disc model, but how important are defects to the question of structural relaxation in amorphous materials in general? Some systems with strong directional bonding interactions, like silica and water, are capable of forming random tetrahedral networks (RTN) of bonds. Recent simulation studies [125] of the ST2 model of water [183] have shown that the FS crossover can be described in terms of the concentration of defects in the network, while similar results have been obtained for network forming colloids [184] and nanoparticles [185]. The structural relaxation of a two dimensional random tiling model has also been described in terms of defect motion [186]. These studies suggest that understanding how defects effect structural relaxation may provide insight to the dynamics of amorphous systems.

As the local environments of the particles become less well defined, it becomes increasingly difficult to identify defects. For example, in the hard discs model considered here, the extreme confinement induces structure and ensures there are only four local packing environments. When the channel diameter increases beyond $H_d/\sigma = 1 + \sqrt{3/4}$, the discs can also contact their second nearest neighbors which increases the number of local environments to 32 [88]. Nevertheless, the concept of incompatibility between local environments remains. Some local particles arrangements cannot be combined to form a stable jammed structure and it would be expected the particles to spontaneously rearrange to form a more stable state.

3.8 Jamming Phase Diagram

The idea of jamming phase diagram was introduced with Liu and Nagel [89] and discussed in chapter 2 in section 2.7. Here, this idea will be extended to the system studied in this chapter. Figure 3.32 shows how the equilibrium fluid samples inherent structure landscape. Similar to granular systems, in systems with hard potential there is no internal pressure from the particles, but it is still necessary for it to do work against P_L if the system expands to sample less dense states. However, there are more low density basins than high density basins, so the balance between these two competing elements results in the "equilibrium" condition for the granular system. In the limit that $P_L h_0 \to \infty$, $S_c/Nk_\mathrm{B} \to 0$ as the system moves toward the most dense state with $\phi_J = 0.842$, while as $P_L h_0 \to 0$, the system samples the jammed states associated with the maximum in S_c where $\phi_J = 0.659$. If the pressures below zero would used, less dense packings would be found and the system enters the least dense jammed state with $\phi_J = 0.561$, and $S_c/Nk_\mathrm{B} \to 0$, as $P_L h_0 \to -\infty$. However, there is no attraction between hard particles that could sustain a negative pressure, suggesting the packings below the S_c maximum are thermodynamically inaccessible.

Figure 3.4 combines the jamming parameters for different channel diameters. The green area is the accessible jammed structures and the yellow region is the jammed states below ϕ_J^* which are not accessible from the equilibrium fluid. The data for the heat capacity maximum as well as the maximum of the inherent structure pressure are included in the graph. Unlike the 1d model, here, the $C_{p\,\mathrm{max}}$ line does not coincide with the data of ϕ_J^* but instead $P_{IS\,\mathrm{max}}$ coincides with the line of $\phi_{J\,\mathrm{min}}$.

3.9 Conclusion

In conclusion, a quasi–one dimensional system of hard discs confined between hard lines was studied to explore the relationship between the inherent structure landscape, the thermo-

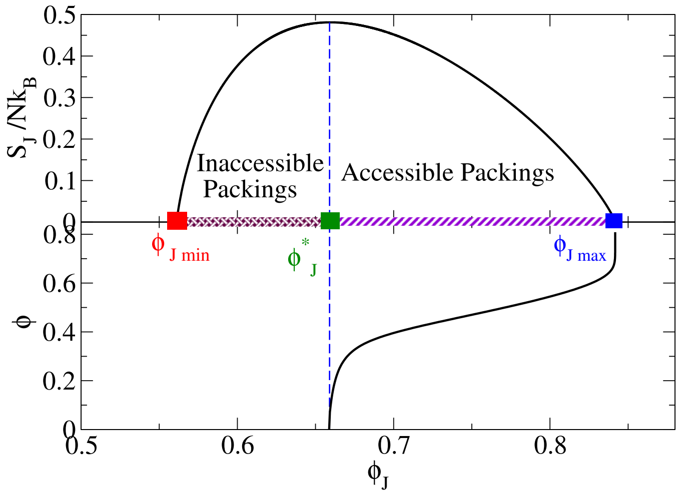

Figure 3.32: Distribution of inherent structures (top) and how the equilibrium fluid samples the inherent structures (bottom).

dynamics and the dynamics of the fluid. The transfer matrix method is used to obtain an exact description of the landscape, equation of state and provide a rigorous mapping of configurations of the equilibrium fluid to their local jammed structures. This allows to follow how the system samples the landscape as a function of occupied volume fraction, ϕ. Configurations of the ideal gas map to the maximum in the distribution of inherent structures, with a jamming volume fraction ϕ^*_J and sample more dense basins with increasing ϕ. This suggests low density jammed states are inaccessible from the equilibrium fluid. The configurational entropy decreases rapidly at intermediate ϕ before plateauing and going to zero as the most dense packing is approached. This leads to the appearance of a maximum in both the isobaric heat capacity and the inherent structure pressure. It is also shown that the system exhibits a crossover from fragile to strong fluid behavior, located at the heat capacity maximum. Structural relaxation in the fragile fluid are controlled by the presence of high order saddle points caused by neighboring defects that are unstable with respect to jamming and spontaneously rearrange to form a stable local environment. In the strong fluid, the defect concentration is low so defects do not interact and the relaxation occurs through the hopping of isolated defects between stable local packing environments.

The universal behavior of the transport properties of the supercooled liquids with respect to temperature is a well–studied subject, and considerable amount of research shows this universality, but all of the previous works were dependent on the fitting functions. In this work this universal behavior was proved by purely analytical approach. For water in confined geometry was proven that FS crossover happens at the point which C_p gets it maximum magnitude, in this confined system the same behavior was noticed. Based on the findings, the FS crossover temperature is an important property of the liquids and can be used instead of T_g in the well–known Angell plot to obtain universal behavior for the supercooled liquids.

Chapter 4

3d Hard Spheres in Confined Geometry

4.1 Overview

The previous chapter demonstrated the usefulness of using the inherent structure distribution to describe the thermodynamics of the fluid. It also highlighted the important role the defects play in determining the fragile and strong behavior of the dynamics. This chapter extends the approach to the study of a quasi–one–dimensional system of hard spheres, which is the three dimensional equivalent of the two dimensional hard disc system. The study is conducted over two channel diameter ranges. With H_d/σ less than $1+\sqrt{3/4}$, there is just a single inherent structure corresponding to the most dense jammed state and no stable defects. In the range, $1+\sqrt{3/4} > H_d/\sigma > 1.98$, the system has a helical chiral most dense packing and can form defects that result in the change of the chirality. The three dimensional geometry makes it difficult to obtain a complete analytical description of the landscape and the packing properties are examined in terms of defect crystals that consist of regularly spaced defects throughout the structure and for which some results can be developed. These analytical jammed packings are compared to the properties of the random amorphous packing formed in simulations. Finally, the fluid is shown to exhibit an orientational phase transition at intermediate densities that is driven by the collective packing properties of the spheres.

The chapter is organized as follows: Section 4.2 gives a brief introduction to hard spheres in confined geometries and the effect of defect in dynamics and thermodynamics. Section 4.2.1 introduces the model. Section 4.3 describes the analysis for fluid thermodynamics and dynamics when the channel diameter, H_d/σ, is less than $1+\sqrt{3/4}$ and Section 4.4 discuss the thermodynamics and dynamics when $1+\sqrt{3/4} > H_d/\sigma > 1.98$. Section 4.5 contains the discussion and the conclusions are described in Section 4.6.

4.2 Introduction

Studies of hard sphere packings in cylinders have focused on identifying the most dense configuration. Pickett et al. [187] used a simulated annealing method that included moves that allowed particle overlaps at high temperatures to search for the most dense packing over a range of channel diameters, $1 < H_d/\sigma < 2.15$. They found that with $H_d/\sigma < 1 + \sqrt{3/4}$, the most dense packing is an achiral zig–zag configuration that is the same as the most dense packing of hard discs, for the same range of channel diameters. In the range $1 + \sqrt{3/4} < H_d/\sigma < 1 + 4\sqrt{3}/7$, the most dense structure consists of a single helix, which then becomes a packing of two staggered helices in the range $1+4\sqrt{3}/7 < H_d/\sigma < 2$. At $H_d/\sigma = 2$ the packing consists of an achiral stacking of pairs of spheres. Mughal and Chan [188–190] developed an analytical approach that involved using a phyllotactic mapping of the particle positions in the cylinder onto packings of discs in two dimensions. This allowed them to examine the effect of introducing different types of particle translations in two dimensions, such as an affine transformation, on the types of possible structures in three dimensions. In all cases, they showed that the symmetrical packing structures were the most dense packing. Recent simulations studies using a sequential deposition approach also identified a new packing for wide channel diameters that involved a mixing of two staggered helices with another distinct helix instead of the three identical staggered helices [191]. Experimental studies have also observed the existence of such packing of spheres in microchannels, nanoparticles in block copolymer microdomains and fullerenes in nanotubes [192–199].

The most dense packing is only one of the inherent structures in the landscape paradigm and does not provide much information about the system's liquid state and the glassy structures associated with them. The complete landscape for hard discs confined in narrow channel with $H_d/\sigma < 1 + \sqrt{3/4}$ was calculated in Chapter 3 and [128] and for slightly wider channel in [88] where the packings were constructed by identifying different local structures, such as defects in the most dense configuration, that could be combined to form collectively jammed packings. As the channel becomes wider, the landscape becomes more complex because more disc–disc contacts are allowed. There appears to be no study of amorphous packings or defects in the quasi–one–dimensional hard sphere system.

The importance of the defects role on the dynamics in supercooled liquids was originally suggested by Glarum [200]. According to this view, the relaxation of an amorphous material occurs via excitation of defects. Since then, others have explored the role of defects on the properties of glass forming liquids [201, 202], but it remains a significant challenge to identify what a defect is in an amorphous system. Many have focused on the role of icosahedral structures in liquids because these do not pack to fill space and may lead to packing frustration [203, 204], but other structures may also be important. For example, a dodecagonal random square–triangle structure appears to play a role in the defect motion and structural relaxation of a two–dimensional binary mixture [186] while a variety of structural clusters have been observed in colloidal mixtures [205, 206]. The facilitated dynamic (FD) models [51, 56, 57, 207] introduce the idea that the dynamics in supercooled liquids occurs when excited regions induce mobility in neighboring regions but again, little is known about the identity of these excited regions. In these defect based approaches, the Adam–Gibbs model is irrelevant and dynamics of the system is not fully determined by the thermodynamics [208].

Defects also play an important role in the thermodynamics of hard particle systems and are a key ingredient in the KTHNY theory [209–211] that describes the phase behavior and melting in two dimensions. The two dimensional crystal is a close packed triangular packing with quasi–long range translational and long–range orientational order. At high densities, topological defects appear in the form of dislocations, consisting of pairs of 5– and 7–fold defects i.e. a 5–7–5–7 defect quartet. These become unbound, forming isolated 5–7 pairs as the crystal melts to a hexatic phase with short range translational order and quasi–long–order orientational order, via a continuous, second order transition. KTHNY theory then suggests that the hexatic phase should melt to the liquid by the unbinding of the dislocations in another continuous transition. However, there is strong evidence to suggests the hexatic to liquid transition is first order [212]. These transitions have been found to be valid in a wide range of 2d systems including hard discs [213, 214], melting in 2d active particles [215] and melting in quasi–2d [216].

The goal of this work is to explore the role of defects in the dynamics and thermodynamics in the quasi–one–dimensional hard sphere system by understanding the distribution of inherent structures.

4.2.1 Model Description

The model studied here consists of N three–dimensional (3d) hard spheres, with diameter σ, confined in a cylindrical narrow channel of length L with diameter of $1 < H_d/\sigma < 1.98$, where H_d is channel diameter (Fig. 4.1). The particle–particle and particle–wall interaction potentials are given by,

$$U(r_{ij}) = \begin{cases} 0 & r_{ij} \geqslant \sigma \\ \infty & r_{ij} < \sigma \end{cases}, \tag{4.1}$$

$$U_w(r_i) = \begin{cases} 0 & r_{xy} \leqslant |H_0/2| \\ \infty & \text{otherwise} \end{cases}, \tag{4.2}$$

respectively, where $r_{ij} = |\mathbf{r_j} - \mathbf{r_i}|$ is the distance between particles, r_{xy} is the component of the position vector for a particle perpendicular to the wall and H_0 is defined as $(H_d - \sigma)$. The volume accessible to the particles centers is $\pi L (H_0/2)^2$ and the occupied volume is $\phi = 2N\sigma^3/\left[3LH_d^2\right]$. The center of the cylinder is located at $x = y = 0$ and extends in the z direction. The periodic boundary condition is applied to the z coordinate. The system is studied in two different ranges of channel diameters. In the range of $1 < H_d/\sigma < 1 + \sqrt{3/4}$, where only the first neighbors contact for the spheres and then in the range $1 + \sqrt{3/4} < H_d/\sigma < 1.98$, where second neighbors contacts also exist.

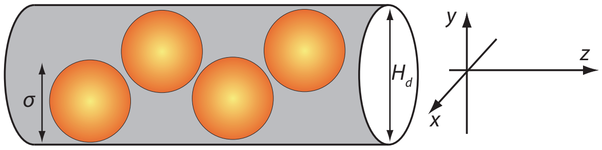

Figure 4.1: Schematic of spheres inside a narrow channel. x and y define the transverse directions and z describes the longitudinal direction along the channel axis. The central axis is taken as $x = y = 0$.

4.3 $1.0 < H_d/\sigma < 1 + \sqrt{3/4}$

In d dimensions, a spherical particle is locally jammed if it has at least $d+1$ rigid contacts arranged such that they are not all within the same hemisphere. However, the local jamming of all the particles in a structure is a necessary, but not sufficient, condition to ensure collective jamming because the concerted motion of a group of particles may allow the structure to collapse [27, 217]. The confinement of the present model prevents the spheres from passing each other, which eliminates the possibility of collective motions of particles unjamming the packings. With $1.0 < H_d/\sigma < 1 + \sqrt{3/4}$, each sphere can only interact with its nearest neighbors and the wall. This means each sphere can obtain a maximum of three contacts which is less that the required contacts for locally jammed structures. As a result, the system should only be able to form a single jammed structure corresponding to the most dense zig–zag structure, (see Fig. 4.2) with a maximum occupied volume fraction of:

$$\phi_J = \frac{2}{3H_d^2\sqrt{H_d\left(2\sigma - H_d\right)}}. \tag{4.3}$$

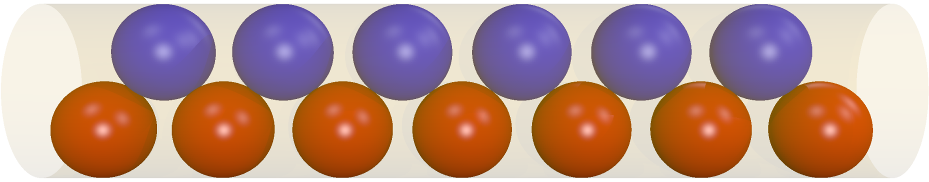

Figure 4.2: Single jammed state for $H_d/\sigma < 1 + \sqrt{3/4}$ ($H_d/\sigma = 1.80$). Two different colors are used to show the nature of the packings.

4.3.1 Thermodynamics of the Equilibrium Liquids

In this range of channel diameters only the nearest neighbors contacts are allowed, which makes it possible to take an analytical approach to the calculation of the thermodynamics properties of the system using the transfer matrix method. A detailed description of the transfer matrix method is given in Chapter 3 and refs [127,151,154], and here only the main features concerning its application to 3d will be included. When the x and y positions of the particles are fixed, the system can be represented as 1d mixture of rods with different contact lengths. This allows the integration over the z coordinates of the particles to be performed independently of the integration of the xy coordinates when solving the partition function. As a result, the solution to the partition function can be represented as an eigenvalues problem where the largest eigenvalue is used, since, at the thermodynamic limit ($N \to \infty$) the largest eigenvalue dominates. The partition function in the N, P_L, T ensemble is given in Eq. 3.10 and the kernel, K for this system is defined as:

$$K\left(y_1, y_2\right) = 2\int_0^{\pi} d\alpha \exp\left[-\beta P_L d\sigma\left(y_1, y_2, \alpha\right)\right], \tag{4.4}$$

with y_1 and y_2 being the y–coordinates of two adjacent spheres in contact. α is the angular separation between spheres centers in cylindrical coordinate space and $\sigma(y_1, y_2, \alpha)$ is the (dimensionless) projection of distances for adjacent spheres along the z–axis and it is a function of y_1, y_2 and α:

$$\sigma(y_1, y_2, \alpha) = \left\{1 - H_d^2 \left[y_1 + y_2 - 2(y_1 y_2)^{1/2} \cos\alpha\right]\right\}^{1/2}. \tag{4.5}$$

In the thermodynamic limit the largest eigenvalue dominates, which gives,

$$\int dy K(y_1, y) \psi(y) = \lambda \psi(y_1), \tag{4.6}$$

where ψ is an eigenfunction. This is solved numerically by constructing a mesh in the y–coordinate with unit size $\delta_y = (H_d - \sigma)/N_d$ and angular separation, α, with unit size $\delta_\alpha = \pi/N_d$ where N_d is the number of divisions. Here, $N_d = 500$ was used. Eq. 4.6 then becomes,

$$K(y_i, y_j) = \exp\left[-\beta P_L L_z(y_i, y_j)\right], \tag{4.7}$$

where $L_z(y_i, y_j) = \sqrt{[\sigma^2 - L_{y\alpha}(y_i, y_j)^2]}$ and $L_{y\alpha}(y_i, y_j) = \sigma(y_i, y_j, \alpha)\,\delta_\alpha$. The molar Gibbs free energy, g, is now given by,

$$\beta g = \ln\Lambda + \ln(\beta P_L) - \ln(\lambda), \tag{4.8}$$

and for a given pressure, the volume of the system can be obtained from,

$$V = (\partial g/\partial P_L)_{N,T}. \tag{4.9}$$

Fig. 4.3 shows the EOS obtained from this method for different channel widths as a function of occupied volume along with the simulation results. The figure shows a very good agreement between simulated and analytical results.

Isobaric Heat Capacity

The isobaric heat capacity is $C_p = (\partial H/\partial T)_P$. For hard spheres the enthalpy is $H = (3/2)Nk_\mathrm{B}T + PV$ and

$$C_p/Nk_\mathrm{B} = 1.5 + PV/Nk_\mathrm{B}T/\left(1 + d\ln\{PV/Nk_\mathrm{B}T\}/d\ln\{\phi\}\right), \tag{4.10}$$

Since the exact equation of state for our system is available, the heat capacity can be calculated. Fig. 4.4 shows the heat capacity for different values of the channel width. Similar

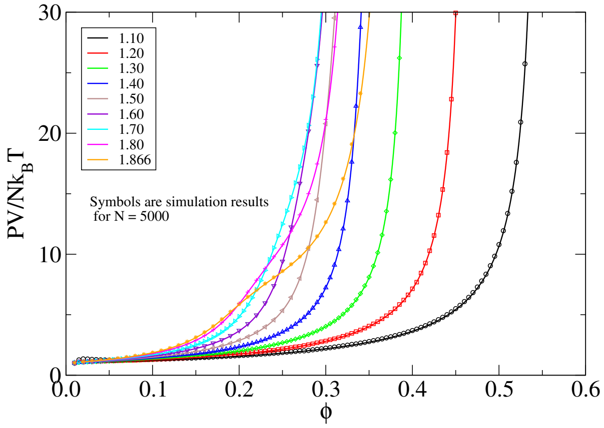

Figure 4.3: EOS for different values of channel widths as a function of density, ϕ.

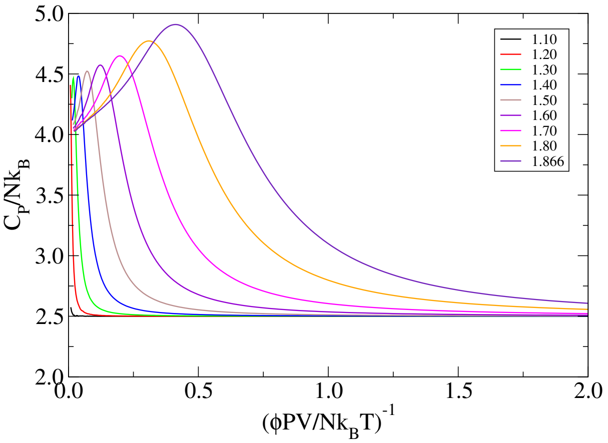

Figure 4.4: C_p/Nk_{B} as a function of $(\phi PV/Nk_{\mathrm{B}}T)^{-1}$ for different values of channel widths.

to 2d system of hard discs confined in a narrow channel, the system exhibits a maximum in the heat capacity. However, unlike the 2d case, where there was a number of different inherent structures, this system has only a single inherent structure. For the hard discs system, Chapter 3 provided a connection between the dynamics and the heat capacity maximum in the context of the distribution of inherent structures. This might suggest there is a different origin of the C_p maximum in the present system.

4.3.2 Simulation Methods

The model is characterized as having N identical particles and the event–driven molecular dynamics (EDMD) simulations [218] have used the canonical (N, V, T) ensemble, where V is the total volume of system and T is the temperature. All lengths will be in units of σ and the units of time in the simulation are $\sigma\sqrt{m/k_{\mathrm{B}}T}$, where k_{B} is Boltzmann's constant and m is the mass of the particles, which taken to be equal to unity.

To compare the results obtained from the exact method described above with the simulation, a system with $N = 10^4$ was used. At the start of each run, N particles are placed in a linear lattice with $\phi = 0.01$ and were assigned a random distribution of velocities that were scaled to give $k_{\mathrm{B}}T = 1$. Depending on the ϕ studied, $200N - 10^6N$ collisions were used to reach equilibrium and the equilibrium properties, like pressure and the dynamics properties, were measured over the next $400N - 10^7N$ collisions.

After collecting data for each density, the system was compressed to a higher density using a modified version of the Lubachevsky and Stillinger [76] (LS) algorithm that ensures H_d/σ remains constant as the diameter of the spheres are changed (L fixed). A compression rate of $ds = d\sigma/dt = 0.001$ was used. The EOS obtained from simulation matched exactly with the results from analytical approach (Fig. 4.3).

4.3.3 Relaxation Time

The dynamic properties of the system were measured in a system of hard spheres containing $N = 10^4$ particles starting from $\phi = 0.01$. Depending on the density, $400N - 10^6N$ collisions were used to reach equilibrium. Simulation lengths varied from $200N$ collisions at low densities up to 10^7N collisions at high densities, and 8.0×10^4 configurations were used at each ϕ to calculate the time averages.

The survival probability method used to study the dynamics of the hard discs model cannot be used here because there is only a single local environment. Therefore, the self–ISF will be used to measure the structural relaxation time for the system. The self–ISF measures the translational degrees of freedom for the system using,

$$F_s(\mathbf{k}, t) = \frac{1}{N} \left\langle \sum_j \exp\left[i\mathbf{k} \cdot (\mathbf{r}_{zj}(t) - \mathbf{r}_{zj}(0))\right] \right\rangle, \tag{4.11}$$

where $r_{zj}(t)$ denotes the z coordinates of the particle j and the angular brackets denotes an equilibrium ensemble average. The bracketed term is proportional to the probability of finding a particle at a distance $\mathbf{r}$ from the origin 0 at time t, given that a particle sits at the origin at time 0. The wave vectors $\mathbf{k}$ were defined along the z axis, as $\mathbf{k} = 2\pi n/L_z$ and integers n were chosen in the range $1 - 60$.

The self–ISF was calculated at the peak of the first maximum in the structure factor, $S(\mathbf{k})$ for each density. Figure 4.5 shows the structure factor for different densities as a function of $\mathbf{k}$. The first sharp peak of $S(\mathbf{k})$ reflects the existence of a dominant nearly regular arrangement of the particles in real space. Figure 4.6 shows that the $F(\mathbf{k}_{\text{max},}t)$ decays to zero suggesting the system behaves like an equilibrium fluid for all densities studied.

The relaxation time, τ_F, is defined via the condition,

$$F(\mathbf{k}_{max}, \tau) = 1/e, \tag{4.12}$$

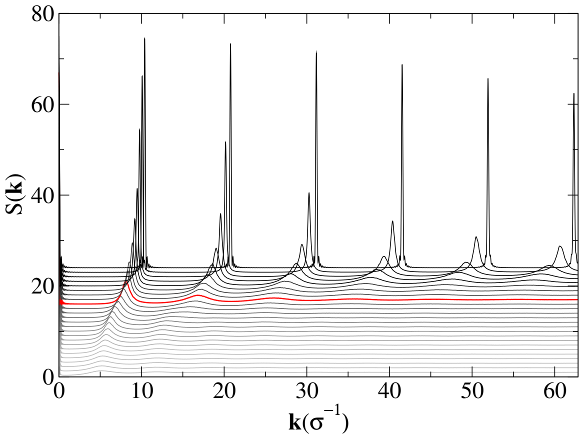

Figure 4.5: Structure factor $S(\mathbf{k})$ for all densities investigated. For clarity the individual curves have been displaced vertically by 1 with increasing ϕ. The red curve highlights the data for $\phi = 0.234$, corresponding to the ϕ of the C_p maximum.

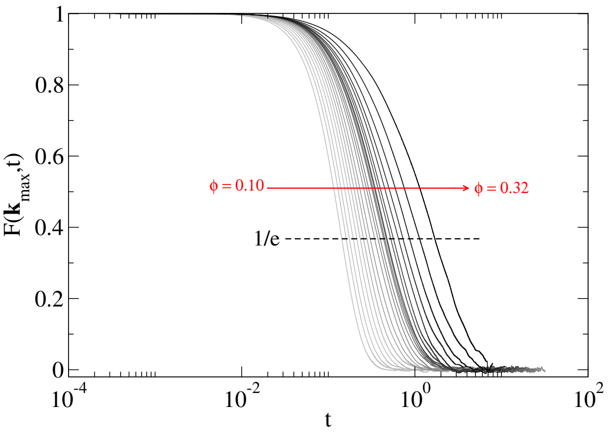

Figure 4.6: Time dependance of self–intermediate scattering function for $H_d = 1.80$ at different densities.

where $\mathbf{k}_{\text{max}}$ corresponds to the maximum of the structure factor, and it is the time that it takes the correlation function to decay to e^{-1} of its initial value (horizontal dashed line in Fig. 4.6). Figure 4.7 shows the Arrhenius plot for τ_F for the case of $H_d/\sigma = 1.80$. There is clearly a change in the dynamics of the system and this occurs at the heat capacity maximum of the system but the exact behavior is not clear.

In particular, τ_F does not exhibit a clear linear type behavior after the C_p maximum making it difficult to determine if the system exhibits a true fragile–strong crossover.

4.4 $1 + \sqrt{3/4} < H_d/\sigma < 1.98$

When the channel diameter becomes wider, the spheres are able to contact their second neighbors. As a result, a particle can have up to five contacts, including four particle–particle contacts and one particle–wall contact. This is more than the number of contacts required for local jamming which opens up the possibility that there are different local packing environments that can be combined to form a range of inherent structures.

It is known that for $1 + \sqrt{3/4} < H_d/\sigma < 1.98$, the most dense jammed structure is a single chiral helix [187–190]. Figure 4.8 shows the two possible enantiomers with the helix

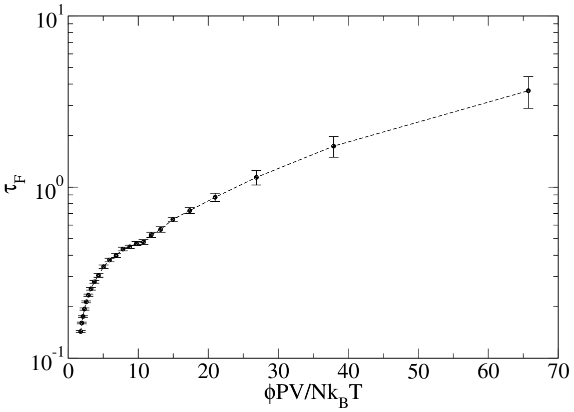

Figure 4.7: Arrhenius plot for the relaxation times obtained from self–intermediate scattering function for $H_d = 1.80$.

twisting in opposite directions. For the present purposes, the R– and S–enantiomers can be defined as relative assignments simply to name the two different structures.

4.4.1 Inherent Structure Landscape Description

In the following, a geometrical approach is developed to examine the nature of the jammed configurations and determine the distribution of the jammed states. The analysis will be carried out using a channel diameter of $H_d/\sigma = 1.95$, but the results are general for channel widths in the range of $1 + \sqrt{3/4} < H_d/\sigma < 1.98$.

Perfect Helix

Figure 4.9 shows the geometric construction used in two and three dimensional projections. The first particle is considered to be positioned at a fixed point in contact with the wall. The addition of the second sphere adds three unknown variables associated with the x, y, z position of the sphere center. There are two constraint equations, one requires particle one and two to be in contact at a distance σ and a second that requires particle two be in contact with the wall. Adding the third sphere will again add three unknowns but in this case there are also three equations because the particle contacts both particle one and two and the wall. As a result, there is always one equation less than the number of unknowns and the system of equations can't be solved analytically. To overcome this problem, a conditional approach

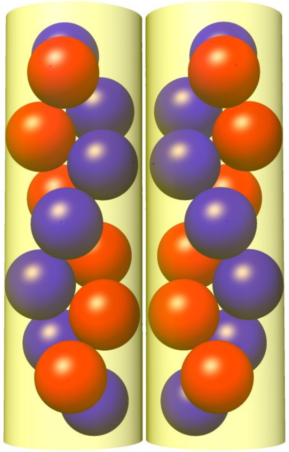

Figure 4.8: Two different enantiomers created because of the chiral nature of the structures. Two different colors are used to show the nature of the packings.

is taken to solve the position of the spheres as a function of the cylindrical angle between the first and the second spheres, α_1. The remaining geometric parameters are then functions of α_1 and the challenge becomes identifying the value of this angle that produces stable jammed states.

By considering that sphere one is in contact with sphere two and three and also sphere two is touching sphere three, the following sets of equations can be obtained from Pythagorean relation and trigonometric relations between parameters which are depicted in the sketch in Fig. 4.9,

$$\sigma^2 = a^2 + Z_1^2, \tag{4.13}$$

$$\sigma^2 = b^2 + Z_2^2, \tag{4.14}$$

$$\sigma^2 = c^2 + (Z_1 + Z_2)^2, \tag{4.15}$$

$$a = H_0 \sin(\alpha_1/2), \tag{4.16}$$

$$b = H_0 \sin(\alpha_2/2), \tag{4.17}$$

$$c = H_0 \sin(\alpha_3/2). \tag{4.18}$$

Here, a, b and c form the projected triangle that is horizontal to the channel axis, Z_1 and Z_2 are the vertical lengths that separate particles one and two, and two and three, respectively. α_1, α_2 and α_3 are the cylindrical angular separations between spheres. Expressions for Z_1 and Z_2 can be obtained by using Eqs. 4.16 and 4.17 in Eqs. 4.13 and 4.14 respectively.

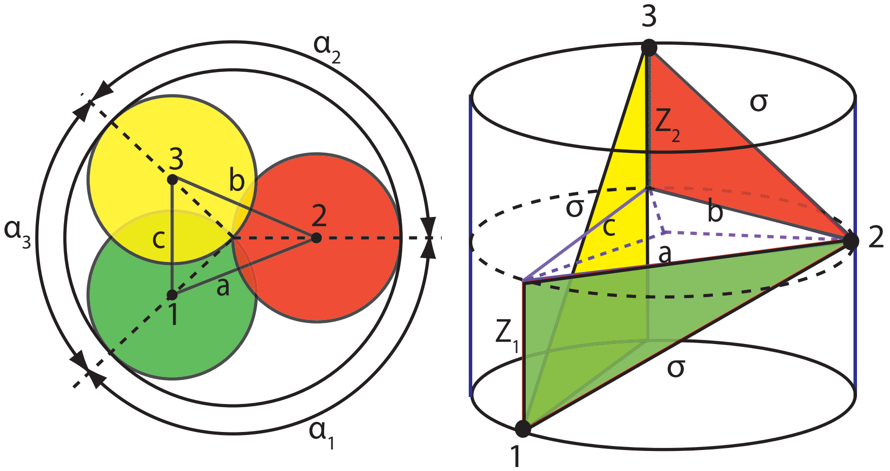

Figure 4.9: 3d and 2d illustration of three particles in contact with each other inside a cylinder.

Substituting the results into Eq. 4.15 and using the constraint, $\alpha_1 + \alpha_2 + \alpha_3 = 2\pi$ in Eq. 4.18 gives,

$$\begin{aligned} \sigma^2 = &\left(\sqrt{\sigma^2 - \frac{H_0^2}{2} + \frac{H_0^2}{2} \cos\left[\frac{\alpha_1}{2}\right]} + \sqrt{\sigma^2 - \frac{H_0^2}{2} + \frac{H_0^2}{2} \cos\left[\frac{\alpha_2}{2}\right]} \right)^2 \\ &- \frac{H_0^2}{2} \left(\cos\left[\alpha_1 + \alpha_2\right] - 1\right). \end{aligned} \tag{4.19}$$

This equation could not be solved analytically, therefore, it was solved numerically. Figure 4.10 shows the contour plot of the solutions. Among all of the contours shown, only the contour with $\sigma^2 = 1$ (shown in red) is relevant to the current problem. α_1 can take on values in the range 2.09564–4.18755. There are then two possible values of α_2 for a given value of α_1 and the smaller value was taken as the physically relevant solution by comparing the results with the geometries observed in the computer generated packings, which are described in detail later.

The solutions for α_1, and α_2 depend on the values of H_d/σ. As $H_d/\sigma \to 1 + \sqrt{3/4}$ the oval solution contour shrinks to a point with $\alpha_1 \to \pi$ so that when $H_d/\sigma = 1 + \sqrt{3/4}$ there is a single solution and the system recovers the zig–zag jammed configuration by $\alpha_1 = \alpha_2 = \pi$ (see section 4.3).

As noted eariler, the longitudinal lengths become functions of α_1 and α_2 and are given by,

$$Z_1^2 + \frac{H_0^2}{2} \left[1 - \cos \alpha_1\right] = \sigma^2, \tag{4.20}$$

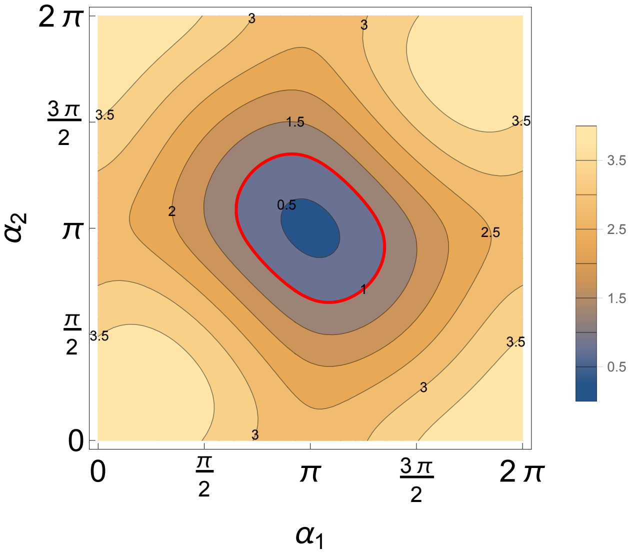

Figure 4.10: Contour plot of the solutions for eq. 4.19 as a function of α_1 and α_2 for the case of $H_d/\sigma = 1.95$.

$$Z_2^2 + \frac{H_0^2}{2}\left[1 - \cos\alpha_2\right] = \sigma^2. \tag{4.21}$$

Figure 4.11 shows Z_1 and Z_2 as a function of α_1, where physical value of α_2 has been used. The three particle system considered here only resembles a small section of the helix. With α_1 and α_2 fixed, the position of the next (fourth) particle is fully determined and is equal to α_1 which then requires the fifth particle to be located at α_2. As a result, a complete helix, with all particles maintaing four particle–particle contacts and one wall contact is formed by alternating spheres with increments of α_1, Z_1 and α_2, Z_2 in cylindrical coordinates. However, while all the particles satisfy the local jamming condition, they are not necessarily collectively jammed as α_1 can be freely varied. To find the most dense jammed structure it is necessary to minimize the total length of the jammed structure, or minimize the length per particle,

$$\frac{L}{N} = \frac{1}{2}\left(Z_1 + Z_2\right). \tag{4.22}$$

The solid line in Fig. 4.12 shows that L/N goes through a minimum when $\alpha_1 = 2.53784$, which is the symmetrical structure with $\alpha_1 = \alpha_2$. This suggests all the unsymmetrical configurations that satisfy the local jamming criteria are unstable with respect to a compression that causes a collective twisting of the helix until the symmetrical structure is obtained. The most dense perfect packing of the helix obtained here has a $\phi_J = 0.416404$, which is consistent with the simulations results obtained by Pickett, Mughal and Chan [187–190] .

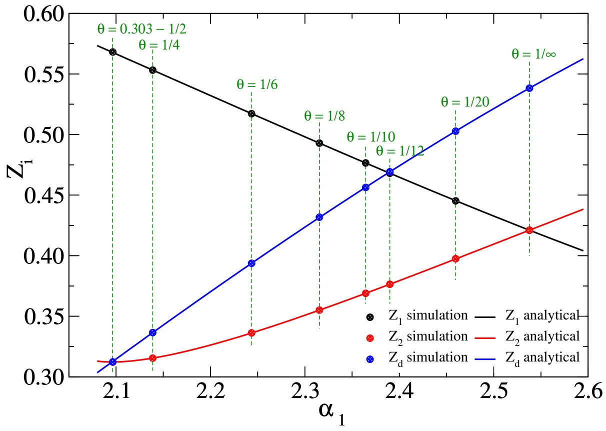

Figure 4.11: The vertical separations between particles (Z_1, Z_2 and Z_d) as a function of α_1.

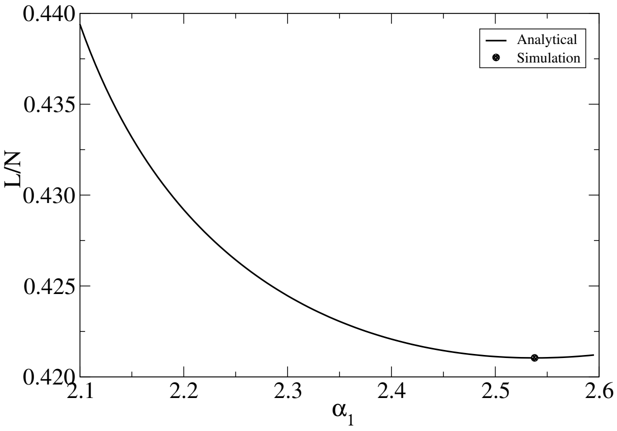

Figure 4.12: The length per particle for the jammed configurations as a function of α_1.

Defects and Defect Crystals

To generate new jammed structures, it is necessary to introduce topological defects into the perfect helix that change the local chirality of the structure by switching the direction of the twist. The geometric construction for the defect is described in Fig. 4.13. With particles one and two fixed as before (i.e. separated by α_1, Z_1), the third particle is placed at angle π and a distance Z_d. Particles two and three do not actually contact and they only become locally jammed once the fourth particle is added with an angle α_1, rotating in the opposite direction so that it establishes a contact with particle two. The defect particles, two and three, have three sphere–sphere contacts and one sphere–wall contact, while the remaining particles have the same structure associated with the perfect helix. The defect angle π replaces α_2 in the structure and Fig. 4.14 shows a comparison of the perfect and defect configurations. If the R and S notation is used to describe the chirality of local sections of the helix in a jammed structure, then a jammed structure containing defects can be described as a linear sequence of R and S where the defects form the interface between the different sections. In a system with periodic boundaries, defects must necessarily appear in pairs so that the chiralities at the boundary match. Figure 4.15 shows a section of a jammed packing containing a single defect in the center.

If it is assumed that the angle α_1 is the same on both sides of the defects, then it is

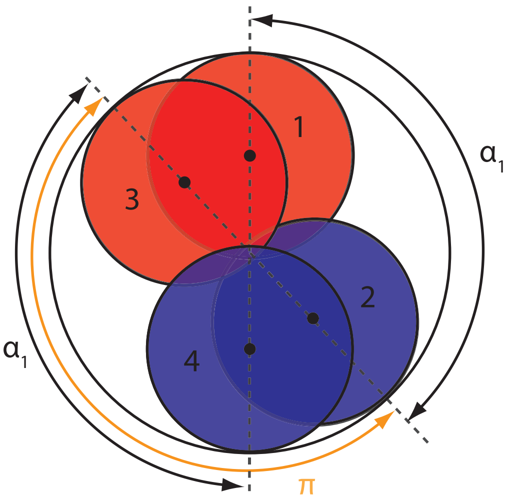

Figure 4.13: 2d illustration of four particles used to describe the geometry of a defect.

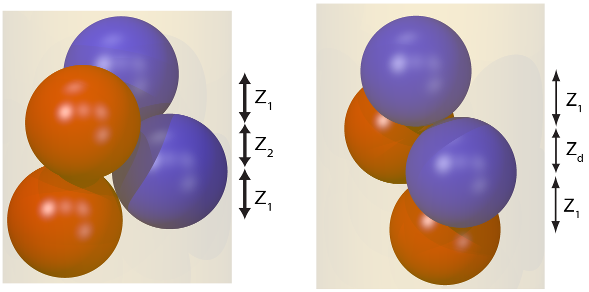

(a) **(b)**

Figure 4.14: Perfect packing tile (a) and defect type tile (b).

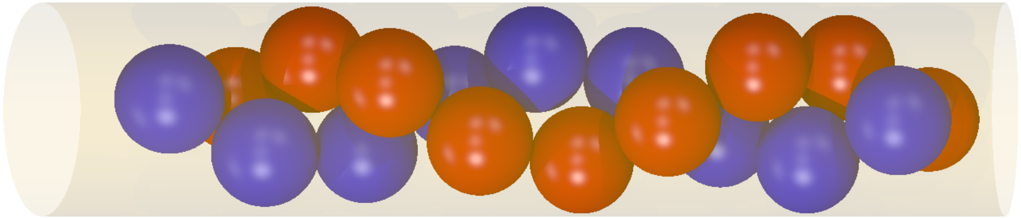

Figure 4.15: The defect type structures will be created when two jammed states with different local chiralities come into contact.

possible to show that,

$$Z_d = \sqrt{\sigma^2 - \frac{1}{2} H_0^2 \left(1 + \cos\alpha_1\right)} - Z_1. \tag{4.23}$$

Figure 4.11 shows that the defect length is longer that Z_2 so that the density of the structure decreases with the inclusion of defects. However, at $\alpha_1 = 2.09564$, $Z_d = Z_2$ and the two defect particles come into contact. It is not possible to move to lower values of α_1 without causing particle overlap.

The effect that the defects have on the global structure of the packing and on the packing density, ϕ_J, can be explored by constructing defect crystals that consist of alternating sections of R and S helices of the same length. By requiring the defects to be equally spaced, each section of helix can be expected to be identical in structure, except for its chirality, so that all the values of α_1 will be the same, which satisfies the assumptions of Eq. 4.23. Since Z_d simply replaces Z_2 when a defect is introduced, the length per particle in a defect crystal is given by,

$$\frac{L}{N} = \frac{1}{2} \left(Z_1 + Z_2\right) + \theta \left(Z_d - Z_2\right), \tag{4.24}$$

where θ is the fraction of defects. Figure 4.16 shows L/N as a function of α_1 for defects crystals with different θ. With $\theta = 0$, the structure is the perfect helix and the minimum appears at $\alpha_1 = 2.53784$ as expected. However, as θ increases, the value of α_1 that minimizes L/N moves to lower values. This means that the jammed structures containing defects are no longer symmetrical so that $\alpha_1 \neq \alpha_2$. It also suggests that the angles in the helical structure are determined by how far the defects are apart. This should be compared with the two dimensional case, where the presence of the defect had no influence on the properties of the most dense local packing environment (See Fig. 4.11 for the vertical lines that shows different defect fractions).

The packing density can be obtained using the following equation:

$$\phi_J = \frac{2N\sigma^3}{3H_d^2 L}, \tag{4.25}$$

where L/N is given from eq. 4.24. The packing fraction for ordered defects is dependent on the fraction of defects, θ, and the angular separation, α_1. Figure 4.17 shows a contour plot of packing fraction dependency on θ and α_1. At each defect fraction, the system finds the maximum packing fraction and samples that configuration at jammed packing (black line in the figure). When the defect fraction is above $\theta = 0.303$ the length of the defect state no

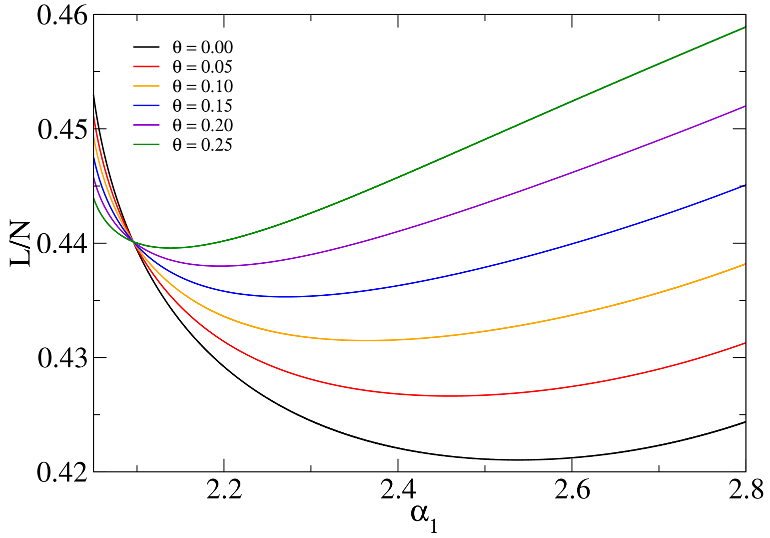

Figure 4.16: Horizontal particle separation in the defect state, Z_d at different values of angular separations α_1.

longer changes and all of the crystal configurations containing a defect fraction above that point will have the same density. Figure 4.18 shows ϕ_J for the ordered defect states as a function of defect fraction, θ.

Distribution of Jammed States

As described, the defect can replace any Z_2 in the structure. If there are N particles and M defects, it becomes a simple combinatorial problem of finding the number of ways of putting the M defects amongst the $N/2$ sites. Therefore, to count the number of jammed packings with a given defect fraction, the following equation can be used:

$$N_J\left(\phi_j\right) = \frac{(N/2)!}{M!\,(N/2-M)!}. \tag{4.26}$$

As a result, the entropy of the jammed configurations is given by:

$$S_J/Nk_{\mathrm{B}} = (1/N)\ln N_J\left(\phi_j\right) = (1/2)\ln(1/2) - \theta\ln\theta - (1/2-\theta)\ln(1/2-\theta)\,. \tag{4.27}$$

Here, S_J count the number of jammed packings at a given defect fraction. To calculate the maximum of the jammed structure entropy, derivative of the S_J/Nk_{B} calculated as,

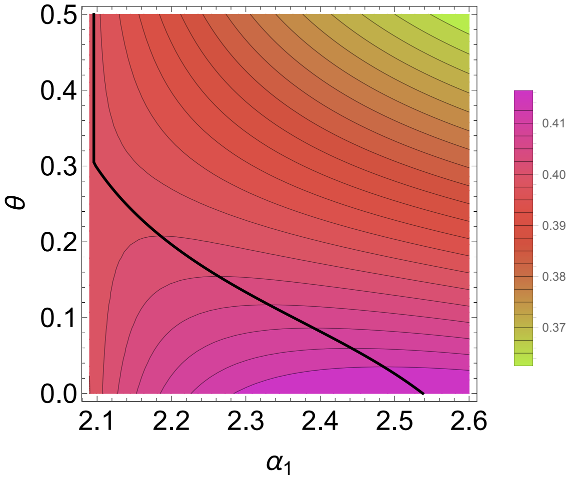

Figure 4.17: Contour plot of ϕ_J as a function of α_1 and θ for the case of $H_d/\sigma = 1.95$.

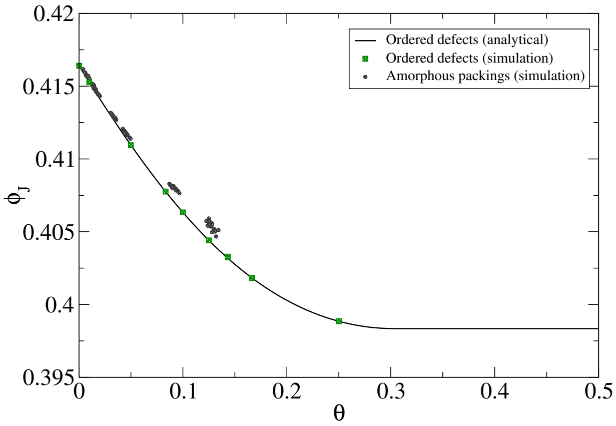

Figure 4.18: ϕ_J for the ordered defect configurations as a function of defect fraction, θ.

$$\frac{\partial S_J/Nk_{\mathrm{B}}}{\partial\theta} = \ln\left[\frac{1}{2} - \theta\right] - \ln\left[\theta\right], \tag{4.28}$$

and equating this to zero gives $\theta = 0.25$. Figure 4.19 shows S_J/Nk_{B} as a function of θ. This shows that the number of jammed packings go through a maximum at $\theta = 0.25$ and there are only single jammed structures at $\theta = 0$ and $\theta = 0.5$ as the most dense and least dense structures respectively. The configurations associated to these structures are depicted in Fig. 4.20. In this figure, "a" is the most dense packing with $\theta = 0$ which is the symmetric helical packing and "b" is the least jammed state with $\theta = 0.5$.

Molecular Dynamics Simulations of Jammed States

To confirm the analytical results described above, a series of MD simulations were also performed. A series of defect crystals, with a given θ were created by placing particles in increments of α_1, Z_1 and α_2, Z_2 and defects with π, Z_d ensuring the defects are equally spaced. Periodic boundaries were also used. These configurations were then decompressed slowly using MD until the particle rearrangements began.

Free volume equation of state [174, 219] is given by,

$$p = \frac{PV}{Nk_{\mathrm{B}}T} = \frac{1}{\delta} = \frac{d}{1 - \phi/\phi_J}, \tag{4.29}$$

requires that the system stays at a single inherent structure and the particles vibrate around

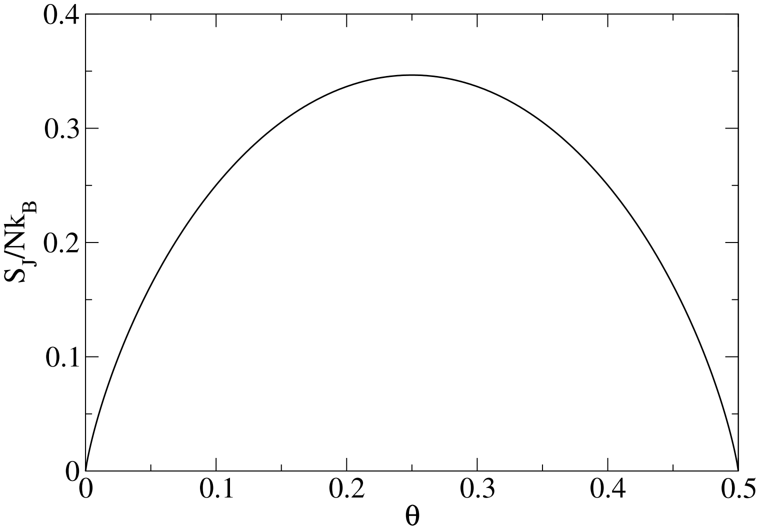

Figure 4.19: Distribution of jammed packings as a function of defect fraction.

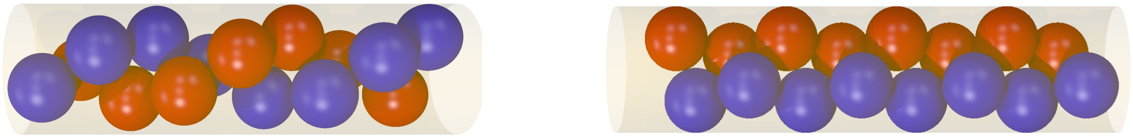

(a) **(b)**

Figure 4.20: Configuration with $\theta = 0$ (a) and configuration with $\theta = 0.5$.

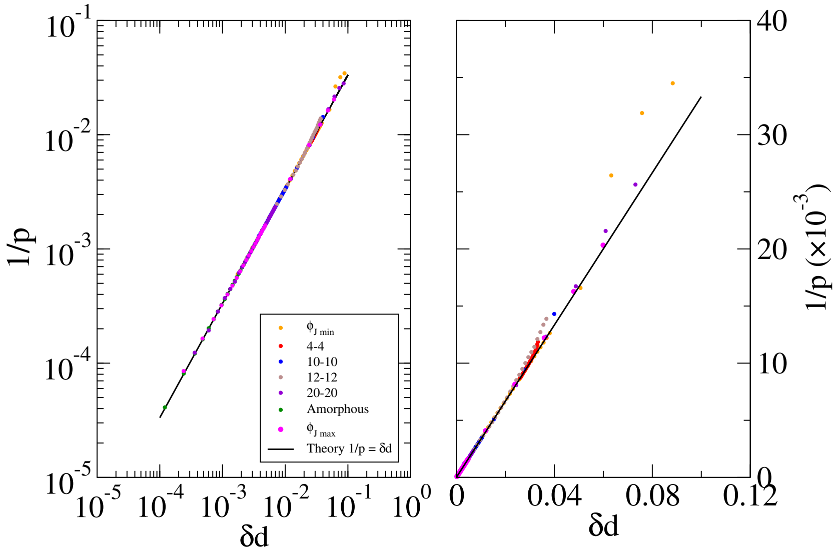

Figure 4.21: The Free Volume EOS for the systems of jammed states.

the lattice point associated with their position in the inherent structure.

The equation can be used to give an estimate of $\phi_J \simeq \phi/\left(1 - d/p\right)$ of the jamming density. Figure 4.21 confirms the validity of the free volume EOS for the jammed packings that were created using the geometrical approach for different ordered defect configurations in normal and log–log scale. The slope of the lines are consistent with dimensionality of the system and the jammed densities, ϕ_J, are consistent with the calculations.

To check the geometrical properties of the jammed configurations, a similar method was used. However, the configuration decompressed to lower densities was stopped before the system collapsed. The configurations were then compressed back to their jammed density until the pressure diverge. The final jammed configurations from MD simulations were used to measure the geometrical properties of the particles. Figure 4.22 shows the results obtained from geometrical approach and simulation. The solid lines show the results of the geometrical approach. The lengths are shown as a function of number of particles in the defect gaps, N_{PDG}. The small value of N_{PDG} means high defect fraction and vice versa. As described above, when the defect fraction is $\theta \geq 0.303$, the length of the defect can not increase and as a result Z_1, Z_2 and Z_d stay the same. The results from the simulation of ordered defects are

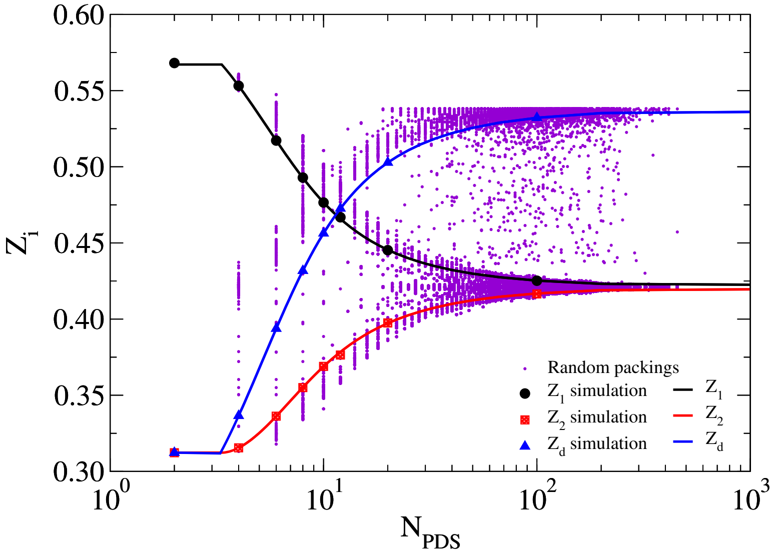

Figure 4.22: Length analysis for Z_1, Z_2 and Z_d as a function of number of particles in the gaps between defects, N_{PDG}. The solid lines are the results from geometrical approach, big symbols are the values from simulation of ordered jammed configurations and small symbols show the values for amorphous packings from simulations.

shown with big symbols in this figure and they matched with the geometrical results.

To study how the system explores the landscape and generates random packings, MD simulation was used to compress low density configurations to their jamming point, with different compression rates. The MD simulations started with $N = 10^4$ particles at low density, $\phi = 0.01$, and the system was compressed to its jammed configuration using the LS method with different compression rates in the range $d\sigma/dt = 0.0005 - 0.3$. At high compression rates the system falls out of equilibrium quickly and became jammed at lower densities. The process was repeated using 20 different initial starting configurations. It is should be noted that at very fast compression rates the LS method is not able to create jammed configurations. The free volume EOS method was used to check the stability of the jammed states. As the compression rate is decreased, the fluid remains in equilibrium longer and becomes trapped in a glass with a higher ϕ_J and if the system compressed infinitely slow $\phi_J \rightarrow \phi_{J\,\max}$. The jammed configurations obtained from this method are amorphous jammed packings and they do not contain any order in the position of the defects.

As discussed above, three different types of structures exist in the jammed states for

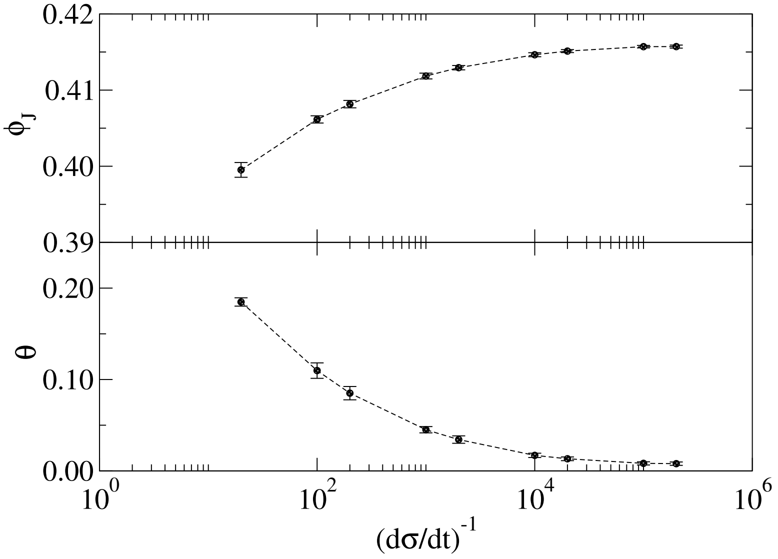

Figure 4.23: Jammed density of the system at different compression rates (top figure) and the defect fraction of the jammed states at different compression rates (bottom figure). The dashed lines are guides to the eye.

this system, locally R, S and the defect states. The main difference between these three configurations is their local chirality. R and S have opposite local chiralities and the defect state is achiral. The identity of the local configuration can be determined by considering the volume of the tetrahedron, Δ_{imnj}, formed by four consecutive particle centers along the channel, for atoms i, m, n, j, calculated using the position vectors relative to particle i. The planar geometry of the defect located between m and n means that $\Delta_{imnj} = 0$. On either side of the defect, the volumes take on opposite signs.

The fraction of defects at different compression rates is shown in Fig. 4.23 (bottom figure). As expected, at fast compression rates the system does not have enough time to eliminate defects and a high fraction of defects get trapped in the configuration. At low compression rates the system eliminates the defects to become jammed with higher density. The ϕ_J and θ for different compression rates are shown as black symbols in Fig. 4.18.

The length analysis for Z_1, Z_2 and Z_d can be obtained for these amorphous packings as a function of different defect separations. The results are shawn in Fig. 4.22 with small symbols. The values of Z_1 and Z_2 generally follow the ordered defect packings, but the values of Z_1 from amorphous packings are slightly higher than the ordered packings and in case of Z_2 are smaller than the ordered defects. The Z_d has higher values comparing to the ordered defects. This is not a surprise, since in the amorphous packings the two sides of the defect state are different. In the ordered defect structures, the defect separations are always the same.

Even though the analytical approach requires the number particles for separating defects to be even, in the amorphous jammed packings exhibit odd values of N_{PDG} at higher separations. This could be a sign of the limitation of the MD in generating perfect jammed states, or an indication of the existence of a new set of solutions for the jammed structures using odd N_{PDG}s.

4.4.2 The Equilibrium Fluid

The transfer matrix method can not be used for this range of channel diameters because of the second neighbor contacts. However, molecular dynamics simulations can be used to obtain the thermodynamics and dynamics properties of the system. In the following, a series of event driven MD simulations will be discussed.

Thermodynamics of the Equilibrium Fluid

The event driven MD simulations are carried out in the canonical ensemble (N, V, T), using $N = 10^4$. Simulations were started from a dilute configuration with $\phi = 0.01$. At each density, $(200 - 10^6)\, N$ number of collisions were used to reach equilibrium and $(400 - 10^7)\, N$ number of collisions were used to collect data. Then the system compressed using the LS scheme to the next density. The process was repeated using 20 different initial starting configurations. Figure 4.24 shows that the EOS obtained for the case of $H_d/\sigma = 1.95$ varies continuously and there is no signs of a first order phase transition for the system. Figure 4.25 shows the results obtained for C_p/Nk_{B} calculated using Eq. 4.10. The C_p exhibits two maxima. The first maximum, which is a broad peak, occurs at intermediate densities, is then followed by another sharp peak at higher densities, or lower temperatures.

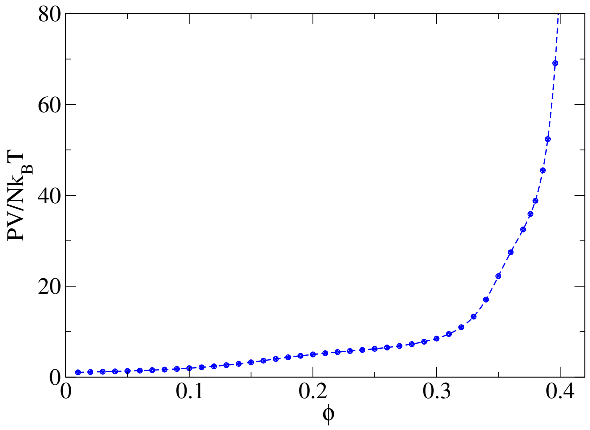

Figure 4.24: $PV/Nk_{\mathrm{B}}T$ versus ϕ for $H_d/\sigma = 1.95$. The dashed line is a guide to the eye.

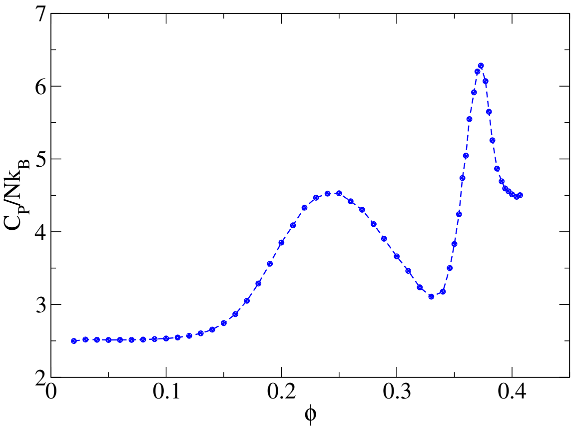

Figure 4.25: C_p/Nk_{B} versus ϕ for $H_d/\sigma = 1.95$. The dashed line is a guide to the eye.

Mapping Configurations to Inherent Structures

A method of identifying different chiralities in a configuration is described in Section 4.4.1. A similar method was used to map the equilibrium fluid configurations to their inherent structures. However, in the fluid state the defects do not necessarily adopt a perfect planar arrangement so that $\Delta_{imnj} \neq 0$. To overcome this, the product of two successive tetrahedron volumes, $\Delta_{imnj} \cdot \Delta_{mnjk} < 0$ indicates the presence of a defect since the volumes must change sign as the helix changes chirality. Tetrahedra with the same chirality give $\Delta_{imnj} \cdot \Delta_{mnjk} > 0$. Figure 4.26 shows θ as a function of ϕ for a system with $H_d/\sigma = 1.95$. The red symbols in this figure shows the measurements of the defect fraction in case of including unstable soft modes caused by neighboring defect, which are unstable into consideration. However, the local unstable modes associated with neighboring defects cannot be represented in the true inherent structures and should be eliminated. The results for the defect fractions without the soft modes are shown with black symbols in the figure. The ideal gas state of the system samples the inherent structures with defect fractions equal to the maximum of the inherent structure distribution ($\theta = 0.25$). θ initially remains constant at low densities before it decays to another plateau at intermediate densities. Finally, θ decays rapidly to zero at high densities.The system falls out of equilibrium at a density and becomes trapped at a glassy state with a fixed number of defects. The saddle point index, η, is shown at different densities in Fig. 4.27. The concentration of the saddles decreases and shows a plateau at

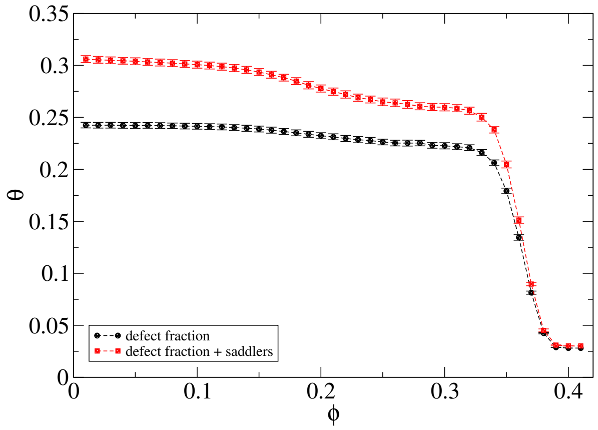

Figure 4.26: Fraction of defect states, θ, as a function of density, ϕ.

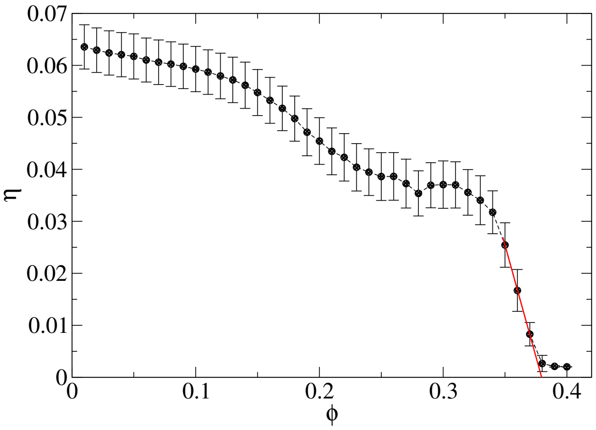

Figure 4.27: η as a function of ϕ. The solid line represents data measured from MD simulation. The dashed line is the linear extrapolation.

intermediate densities and finally vanishes at high densities. The linear extrapolation at high density would locate the position of $\phi_d \sim 0.38$. After this density, the defects become rare.

After ϕ_d the defects get isolated and the dynamics of the system will be dependent on the activated processes in the system. Figure 4.28 shows the space–time plots for the system at six different densities. The red and blue colors correspond to the local R and S chiralities respectively and the black color is the defect state. At low densities the two different local chiralities are mixed randomly. The defects move freely and constantly interact causing the color of a given particle to change rapidly with time as it moves from R to S helix configurations. At intermediate densities, where the first heat capacity maximum occurs, the the R and S sections increase in length but still the defects are not isolated. However, at the second C_p maximum, the system rapidly eliminate the defects, which leads to stable sections of R and S. After the C_p maximum, the defects are isolated and it takes long times for the defects to annihilate or create. When the system is trapped in a glassy structure the defects are almost stable.

4.4.3 Relaxation Time

To study the relationship between the packing landscape and the dynamics of the fluid, the structural relaxation times for the system were calculated over a range of ϕ, using two different methods. All simulations used $N = 10^4$ particles. Starting from $\phi = 0.01$, between

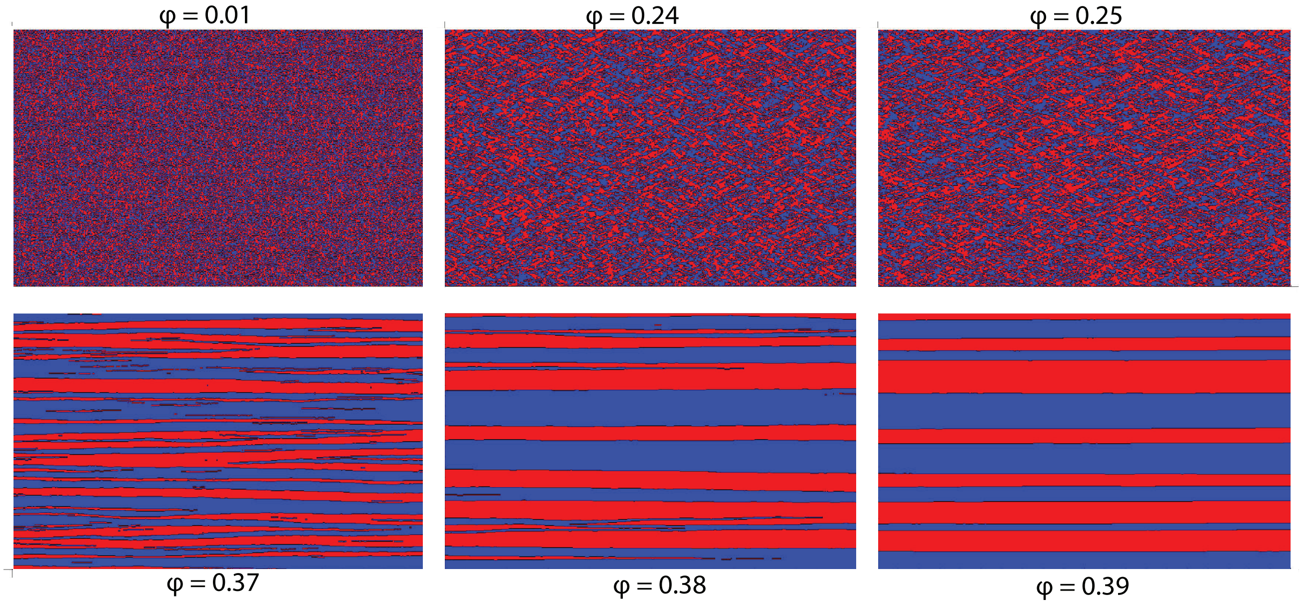

Figure 4.28: Representative trajectories in the system. The vertical axis is space measured in particle number, the horizontal one time. The six trajectories are for very low density, $\phi = 0.01$, before first heat capacity maximum, $\phi = 0.24$, after first heat capacity maximum, $\phi = 0.25$, before the second heat capacity maximum, $\phi = 0.37$, after the second heat capacity maximum, $\phi = 0.38$ and at glassy configuration, $\phi = 0.39$. Configurations with R local chirality are red, and configurations with S local chirality are blue and the defects are black.

$400N - 10^7N$ collisions were used to reach equilibrium, then relaxation times were measured with simulation lengths that varied from $200N$ up to 10^7N, depending on the occupied volume fraction. 8×10^4 equally spaced configurations were sampled at each ϕ.

Self–Intermediate Scattering Function

The details of the relaxation time measurement using self–ISF are given in section 3.6.3 and 4.3.3. For this channel diameter range the same approach was taken. Figure 4.29 shows the evolution of structure factor, $S(\mathbf{k})$, for the system at different densities. For the 2d narrow channels, the relaxation time of the system was related to the fragile–strong crossover which occurred at the heat capacity maximum. Therefore, the two densities of the heat capacity maximum are shown in red in the figure. The emergence of the first peak, at small $\mathbf{k}$, which corresponds to longer ranges reflects the growth in real space of the regular helical arrangements of the particles associated with the most dense packing. In particular, a rapid, but still continuous, shift of the peak to larger $\mathbf{k}$ at ϕ near the first C_p maximum.

The structural relaxation time for the system then was measured using the self–ISF method at the first maximum in $S\left(\mathbf{k}\right)$ (refer to section 4.3.3 for more details). The structural relaxation time, τ_F was measured when the self–ISF decays to e^{-1}. Figure 4.30 shows the τ_F for $H_d/\sigma = 1.95$ as a function of $\phi PV/Nk_\mathrm{B}T$. At high ϕ (equivalent to low temperatures) the system shows a linear increase in the relaxation time as $1/T$ which is characteristic behavior of the Arrhenius and "Strong" supercooled liquids. This dynamics behavior change happens at the C_p maximum. At low densities, however, because of the structural evolution of the system a decrease in the relaxation time occurs and the behavior is less clear. It is worthwhile to mention that this strange behavior corresponds to the first heat capacity maxima.

Survival Probability

Furthermore, the relaxation time was measured using the survival probability of the local environment of the particles in the inherent structure. The volume of tetrahedrons described earlier was used to identify the local environments in the configurations. The survival probability is an integrated relaxation time and defined as following [220]:

$$\tau = \int_0^\infty R\left(t\right) dt. \tag{4.30}$$

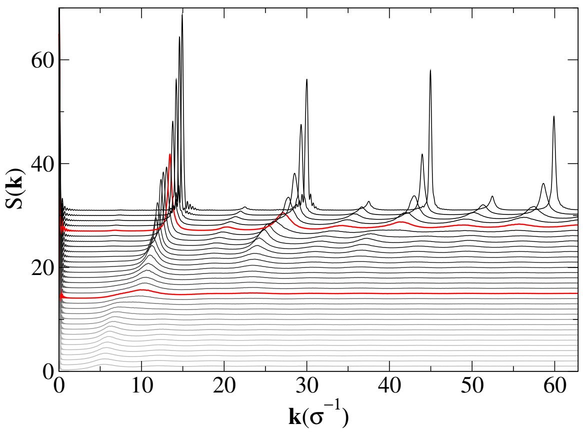

Figure 4.29: Structure factor $S(\mathbf{k})$ for all densities investigated. For clarity the individual curves have been displaced vertically by 1.

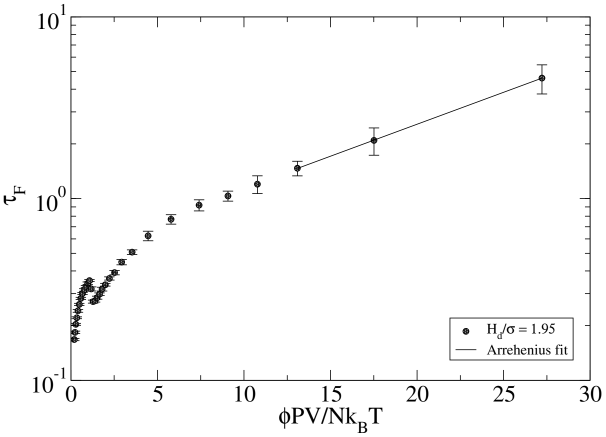

Figure 4.30: Arrhenius plot for the relaxation times obtained from self intermediate function for $H_d/\sigma = 1.95$.

Here, $R(t)$ is the fraction of unchanged configurations at time t with respect to their initial configurations at time $t = 0$. $R(t)$ decays in the same way as $F(\mathbf{k}, t)$, except in this case the behavior of the relaxation at different densities is more evident and does not contain the strange behavior.

Figure 4.31 shows the relaxation time measured using this method along with Arrhenius and parabolic [17,175] fits to the data. The Arrhenius equation fits the data at high densities and parabolic equation fits well when restricted to the data between two C_p maximum and gets worse when the whole data range used. This suggests the high density C_p maximum corresponds to the fragile–strong fluid crossover [127]. The fragility parameter [11] for the data was measured by applying the centered differences scheme to the relaxation data and Fig. 4.32 shows the results. At low densities, the fragility parameter, m_f, initially increases rapidly, before crossing over at the first C_p maximum to a linear increase that finally ends by a plateau at high densities, confirming the crossover to Arrhenius behavior. The crossover from super–Arrhenius behavior to Arrhenius behavior occurs at the second C_p maximum.

4.4.4 Orientational Order Parameter

The origin of the second heat capacity maximum for this system was determined to be the fragile–strong crossover, but the origin of the first heat capacity maxima still remains unsolved. The defect fraction as a function of density does not show a significant change by

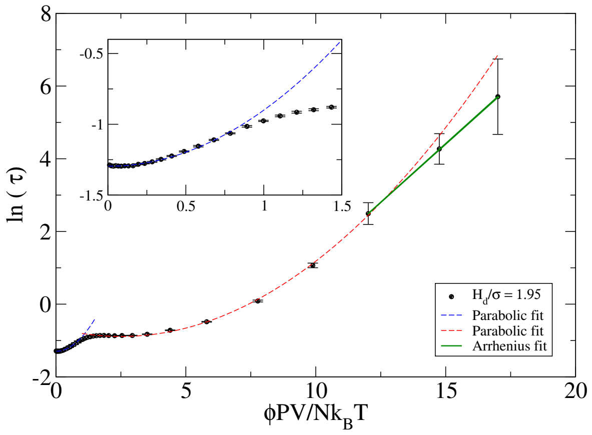

Figure 4.31: Arrhenius plot for the relaxation times for $H_d = 1.95$. The dashed lines represent parabolic equation fits to the data in the fragile region. The solid line is the Arrhenius fit to the strong fluid region.

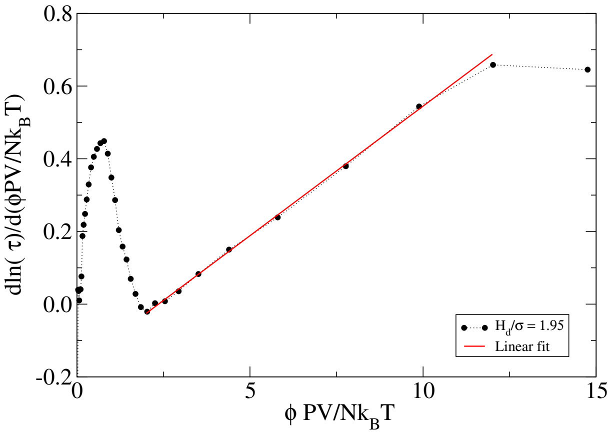

Figure 4.32: The derivation of the logarithmic relaxation time τ is plotted against $1/T$ for $H_d = 1.95$.

passing the first C_p maximum, even though it plateaus. Therefore, since the system creates helical packing at the jammed density, the orientational order for the system is measured. Using the local orientational bond order ψ_6. This quantity was first introduced by Nelson and Halperin [221] to study the order of 2d systems. For this range of channel diameters, the helical structures are created by equilateral triangle that are wrapped into the cylinder which represents the hexagonal packings of the jammed configurations in 2d hard discs and makes it possible to use ψ_6. It is given by [213, 222],

$$\psi_{6j} = \exp\left[6i\theta_{ijk}\right], \tag{4.31}$$

where θ_{ijk} is the angle of the bond between particle i and its neighbors j and k. $\psi_6 = \langle\psi_{6j}\rangle$, where the average is over all the particles configurations. Figure 4.33 shows that the local orientational order around a particle increases as a function of ϕ for different system sizes. The subsystem analysis method [223, 224] was applied to obtain the data for different system sizes. ψ_6 has a finite value less than unity at low densities and increases as the densities increases toward the jammed packing.

To characterize the long range orientational order, the correlation function,

$$g_6(\mathbf{r}) = \left\langle \psi^*_{6j}\psi_{6k} \right\rangle, \tag{4.32}$$

was measured, where $\mathbf{r} = |z_j - z_k|$ is the separation between particle j and k in the $z-$

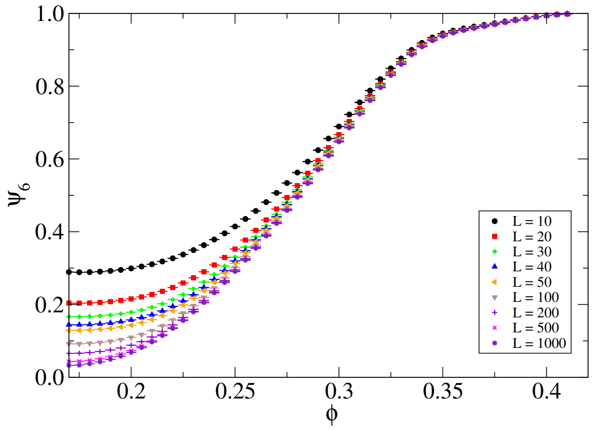

Figure 4.33: Orientational order parameter ψ_6 as a function of density at different system sizes.

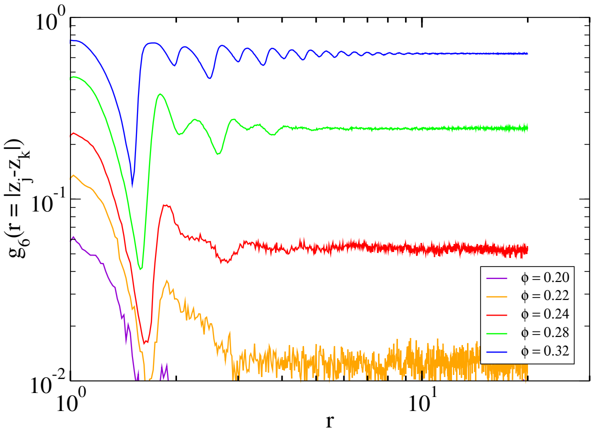

Figure 4.34: Orientational correlation function $g_6\left(z\right)$ as a function of **r** at different densities.

coordinate. Figure 4.34 shows that the orientational correlation function $g_6\left(z\right)$ persists over long ranges and exhibits a long–range order, however, at low densities this decays rapidly.

Bond orientational order susceptibility [225] is calculated to characterize the fluctuations in orientational order,

$$\chi_6\left(L\right) = V\left\langle\left|\psi_6\right|^2\right\rangle - \left\langle\left|\psi_6\right|\right\rangle^2, \tag{4.33}$$

where $\langle.\rangle$ represents the time average. This equation gives the value of the susceptibility in a finite system size, L, but the susceptibility in the thermodynamic limit $\chi_6\left(\infty\right)$ has more importance. However, an estimate of $\chi_6\left(\infty\right)$ can be obtained using finite size scaling and measuring the $\chi_6\left(L\right)$ at different system sizes and extrapolating $L \to \infty$ [223]. Figure 4.35 shows the $\chi_6\left(L\right)$ as a function of density for different system sizes. It can be seen that $\chi_6\left(L\right)$ increases with increasing subsystem sizes. The data for the largest subsystem size is subject to a considerable scatter because the statistics deteriorate as the subsystems become larger [226]. Therefore, these data will not be included in the extrapolation procedure. The susceptibility divergence has been used previously to identify 2d melting phase transitions in simulations [226–229] and experiments [230]. The orientational crossover is consistent with recent experimental study [192] on the thermoresponsive microgel particles.

The finite size scaling [223,231–235] can be used to obtain an estimate of the susceptibility $\chi_6\left(\infty\right)$ in the thermodynamic limit. This can be done by extrapolating the peak heights $\chi_{6(\max)}$ of the distributions shown in Fig. 4.35 with respect to the system size. The power

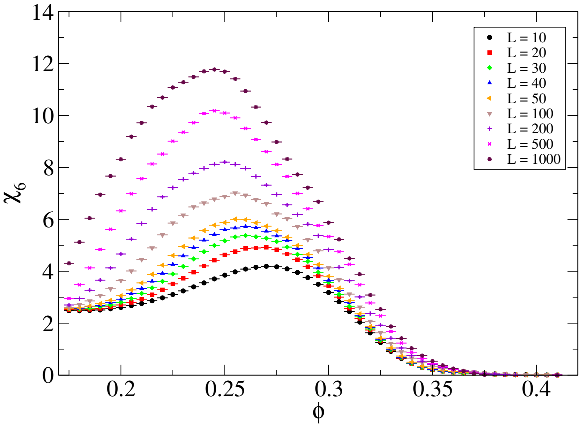

Figure 4.35: Orientational order susceptibility χ_6 as a function of density at different system sizes.

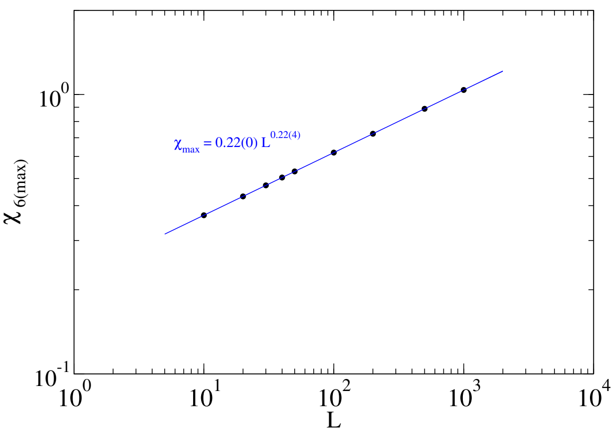

Figure 4.36: Finite size scaling of χ_{max} as a function of different system sizes.

law fit to the peak heights [112, 236] using,

$$\chi_{6(\max)}(L) = cL^z, \tag{4.34}$$

where, $\chi_{6(\max)}(L)$ is the maximum value of the susceptibility for different subsystem sizes and c is a constant value and z is the correlation length critical exponent. Figure 4.36 shows data obtained along with the power law fit and demonstrates that the peak height approaches its limiting asymptotic value as a power law in L.

To find the transition density, the power law fit to the position of the susceptibility maxima is obtained using the following equation,

$$\phi_c(L) = \phi_c(\infty) - cL^{-1/\nu}, \tag{4.35}$$

where $\phi_c(L)$ is the critical (transition) density at subsystem size L and $\phi_c(\infty)$ is the critical density at thermodynamics limit ($L \to \infty$) and c and ν are constant parameters. Figure 4.37 shows the result of density at the peaks positions as a function of subsystems length. Equation 4.35 fits the data well and the critical density is calculated to be $\phi = 0.24(0)$. Figure 4.38 shows the linear fit for the data in Fig. 4.37.

This analysis suggests the existence of a higher order orientational transition in the system at a density which is consistent with the first heat capacity maximum.

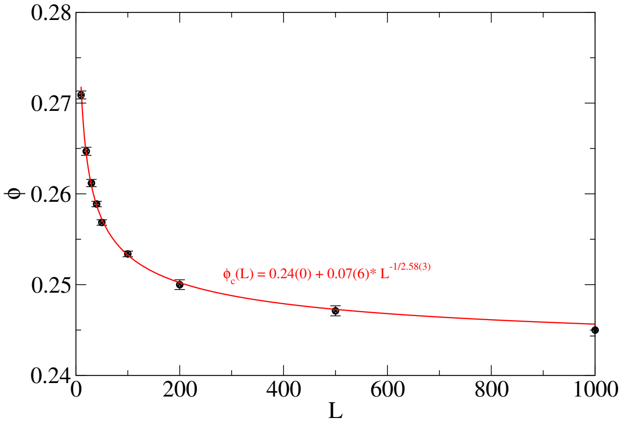

Figure 4.37: Density of the peak in the orientational order susceptibility, χ_6, as function of system size.

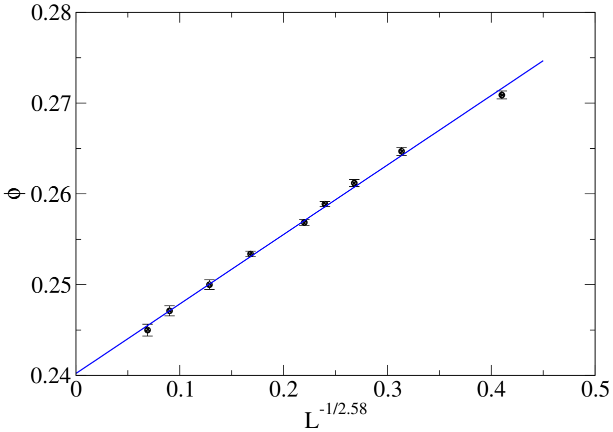

Figure 4.38: Linear scaling of the position of the peak in the orientational order susceptibility.

4.5 Discussion

The physical picture that arises from the current work is very similar to that of the 2d hard discs confined in a narrow channel. However, in this model the orientational order transition arises from the helical nature of the jammed structures. The defect states are playing a major role in the dynamics and thermodynamics of the current model.

The melting mechanism of a bulk two–dimensional hard disc system involves two steps: first at high densities, the system undergoes a continuous phase transition from a crystal with quasi–long–range positional order and long–range orientational order, to the hexatic phase with quasi long range orientational order and positional disorder; the second phase transition happens from hexatic phase to liquid phase with no order in their position and orientation. However, it has been shown that in one-dimensional equilibrium system with short range interaction, phase transitions do not occur. Because the thermal fluctuation in the 1d system destroys any long range order [237, 238]. If a system has long range interactions it can have phase transition [239–248]. For example, the Ising model with long–range Hamiltonian decaying with distance as $J(r) \sim r^{-1-\sigma}$ has been well studied and it has been demonstrated that the system orders at low temperatures [242, 246].

The question then arises: How does a quasi–one–dimensional hard sphere system exhibit a phase transition? As shown in Fig. 4.22, it is the distance that separates the two defects at the end of a section of helix that determines the distances, Z_1, Z_2, Z_d and angles α_1, α_2 for that section, in the jammed configurations. In the fluid, particles in a section of helix vibrate around these positions until the defect moves causing them to adopt the new inherent structure positions associated with the new defect separation. This results in an effective long range interaction between the defects that arise out of the collective properties of the system. Since this interaction is long ranged, the restrictions of van Hove and Landau no longer apply, which means this quasi–one dimensional model can exhibit a phase transition, even though pair interaction is short ranged. This is the same entropic driving force [249] that causes the bulk hard sphere system to freeze [63]. However, the entropic advantage to having defects in the quasi–one–dimensional system prevents the formation of a solid phase. As a result, the system forms an orientationally ordered fluid containing defects, similar in nature to the hexatic phase except that the defects are never bound.

The system at low densities contains a high concentration of defects and shows a super–Arrhenius behavior, which suggest it is a fragile fluid. After the phase transition, the orientationally ordered fluid remains fragile while there are a large number of defects. At high densities, the concentration of defects decreases the the fluid exhibits strong fluid, Arrhenius behavior. Different systems [119–125, 127] have been shown to exhibit a fragile–strong crossover located at the C_p maximum and the current model also provides another example.

To construct the full jamming phase diagram for the system, the compression study is carried out over the range of channel diameters $1 < H_d/\sigma < 1.98$. When the system is compressed slowly, it stays in equilibrium longer and samples deeper basins before becoming jammed at a density that is close to $\phi_{J\,\max}$, but when the system is compressed rapidly, it falls out of equilibrium quickly and the jammed density is lower. As stated above, when the system is restricted below $H_d/\sigma < 1 + \sqrt{3/4}$ there is only a single inherent structure for the system and regardless of how fast or slow the system is compressed, it ends up with the same jammed density. However, above $H_d/\sigma > 1 + \sqrt{3/4}$, the system has multiple inherent structures with a distribution of jammed densities and depending on the compression rate the system ends up being in a different basins having a different density.

The positions of the C_p maxima are also shown in the Fig. 4.39 for different values of the channel diameter. At very narrow channels ($H_d/\sigma < 1 + \sqrt{3/4}$) there is only a single maximum but at wider channels, the second maximum appears. The C_p maximum at higher

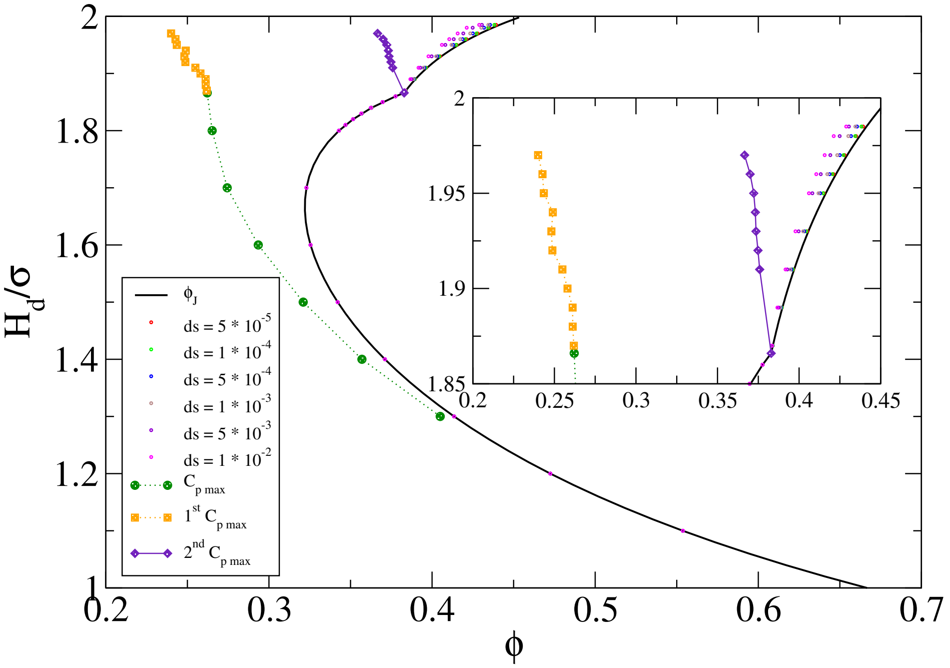

Figure 4.39: Jammed densities obtained for different values of channel diameters using deferent compression rates. The solid line shows the analytical results for $\phi_{J\,\max}$. The values of C_p maxima at different values of channel diameters are also included (refer to text for more details).

densities and wider channels corresponds to the fragile–strong crossover that results from the existence of multiple inherent structures and the effect defects have only dynamics. However, the first heat capacity maximum in the system corresponds to the orientational order transition in the system. The heat capacity maximum in the narrow channels appears to be a correlated to the orientational order transition in the wider channels since they terminate at the same point.

4.6 Conclusion

In Chapter 3, a complete inherent structure landscape for system of hard discs confined in a narrow channel was introduced and the connection between the dynamics and the thermodynamics explored. This section included an extension of this idea to 3d and a more complicated system. Two different cases were studied and the connection of thermodynamics and dynamics explored.

The complete inherent structure landscape of the system was studied analytically and numerically, and the connection of it to the fluid phase explored. The helix pitch and the packing density of the jammed structures varies with the number and distribution of the defects. It was shown that the system exhibits a continuous phase transition from an isotropic fluid to a translationally disordered, but orientationally ordered helical fluid at intermediate densities.

The system exhibits heat capacity maxima and the origin of them were connected to the continuous phase transition and fragile–strong crossover phenomena.

CHAPTER 5

DIFFUSION IN CONFINED GEOMETRY

5.1 Overview

In Chapter 3 the detailed description of the thermodynamics of hard discs confined in narrow channel was discussed and the relaxation time of the system was measured. In this chapter, the dynamics of the same system will be studied using the mean squared displacement and the diffusion coefficient will be calculated. A connection between the dynamics and thermodynamics in context of the diffusion coefficient will be explored. In addition, scaling of the dynamics behavior of the system will be highlighted using an effective diameter concept. Section 5.2 gives a brief introduction to the diffusion in confined geometries. Section 5.3 describes the simulation techniques used to measure the diffusion coefficient. Section 5.4 discusses the transport properties in one dimensional systems and highlights the excess entropy scaling approach. Finally, Section 5.5 describes the conclusions.

5.2 Introduction

With recent advances in nanotechnology and the ability to produce nano–materials, there is considerable interest in understanding the transport of fluids inside them. Fluids in highly confined systems such as carbon nanotubes, zeolites and ion channels in biological membranes often follow single–file diffusion (SFD) in which particles cannot pass each other and the diffusion is constrained in one dimension. The transport coefficients (D) of a fluid can be calculated from the long time behavior of the mean squared displacement (MSD) which is generally given by the Einstein relation:

$$\left\langle (x(t) - x(0))^2 \right\rangle_{\mathrm{SFD}} \propto \alpha l (Dt)^{\gamma}, \tag{5.1}$$

where α depends upon the distribution of jumps in the basic motion, and l is the "free volume" along the x axis per particle and γ is a variable [250]. In bulk fluids and single file systems exhibiting deterministic dynamics (normal SFD), γ is equal to 2 in short time limits due to ballistic motion. In the long time limit, γ becomes equal to 1 and $\langle \Delta x^2(t) \rangle = 2D_x t$. In a single file system experiencing Brownian motion (anomalous SFD), the MSD increase is linear in t for very short times $\gamma = 1$ and in the long time limit the MSD becomes proportional to the square root of time, $\langle \Delta x^2(t) \rangle = 2F_x t^{1/2}$, where the mobility factor F replaces the diffusion coefficient. The current study focuses on case of normal diffusion.

One of the challenging tasks in the field of condensed matter is to find a relationship between the transport coefficients of a fluid and its equilibrium thermodynamics properties. Rosenfeld [251] proposed a relation between the transport coefficient of dense fluids and the internal excess entropy (s^{ex}) that was later expanded to consider dilute fluids [252]. Dzugutov [253] used molecular dynamics simulations to suggest a relationship between the structure of a fluid and the equilibrium rate of atomic diffusion. He proposed that the normalized diffusion coefficient D^* (which is defined as $D^* = D\Gamma_{\mathrm{E}}^{-1}\sigma^2$, where Γ_{E} is an effective Enskog inter–particle frequency) is proportional to the exponential of the excess entropy. Bretonnet [254] has tried to expand Dzugutov's work by proposing a semi–empirical expression for the D of simple fluids over a large range of density. Mittal et.al. [255] have tested a relationship between the structure, entropy and diffusivity for two dimensional (2d) and one dimensional channels and have studied the effect of confinement on dynamics. Also, Truskett *et al.* [256–261] introduced an excess entropy scaling by considering the spatial density distribution for confined systems.

Based on the previous studies, wider channels and bulk systems exhibit, a one–to–one relationship between the diffusivity and the excess entropy over a broad range of thermodynamic conditions, but highly confined channels exhibit noticeable deviation from bulk behavior [262]. Instead of mapping the behaviors of narrow channels into bulk systems, the strategy employed in this study is to use the purely one dimensional system as a reference where the exact analytical solution for the diffusivity is known.

5.3 Simulation Methods

Here a system of two-dimensional hard discs of diameter, σ, confined between parallel hard lines separated by a distance H_d is considered. The channel length in the longitudinal direction is L and the two ends obey periodic boundary conditions. All lengths will be in units of σ. The model is characterized as having $N = 30000$ identical particles and we have used event–driven molecular dynamics (EDMD) simulations [218] in the canonical (N, V, T) ensemble where V is the total volume of system and T is the temperature. Units of time in the simulation are $\sigma\sqrt{m/k_{\mathrm{B}}T}$, where k_{B} is the Boltzmann constant and m is the mass of a particle which is set to unity.

At the start of each run, N particles were placed in a linear lattice with a packing fraction $\phi = 0.1$ ($\phi = N\pi\sigma^2/4V$) and were assigned a random distribution of velocities that were scaled to give $k_{\mathrm{B}}T = 1$. At each ϕ studied, $200N$ collisions were used to reach equilibrium and the diffusion coefficient, D, was measured in the next $400N$ collisions. During this time, the particles coordinates were saved 80 times, separated by $5N$ collisions. After collecting data for each density, the system was compressed to a higher density using a modified version of the Lubachevsky and Stillinger [76] (LS) algorithm that ensures H_d/σ remains constant as the diameter of the discs is changed (L fixed). A compression rate of $ds = d\sigma/dt = 0.001$ was used.

5.4 Results and Discussion

5.4.1 Transport in One Dimensional Systems

The self–diffusivity of the fluid was obtained by fitting the long–time behavior of the average mean–squared displacement (MSD) in the longitudinal direction of the channel (z axis) for the particles into the Einstein equation (eq. 5.1). Figure 5.1 shows MSD as a function of time for the case in which $H_d/\sigma = 1.1$ at different densities (starting from $\phi = 0.1$ up to $\phi = 0.5$ with steps of 0.02). One of the difficulties associated with finding D in narrow channel is finding the correct place to extract it from the MSD plot. As it is clear from figure 5.2, γ changes as a function of time. It is essential to find a place in which the slope is equal to unity. Here, channel widths of $1.1 < H_d/\sigma < 1 + \sqrt{3/4}$ were studied to ensure that only

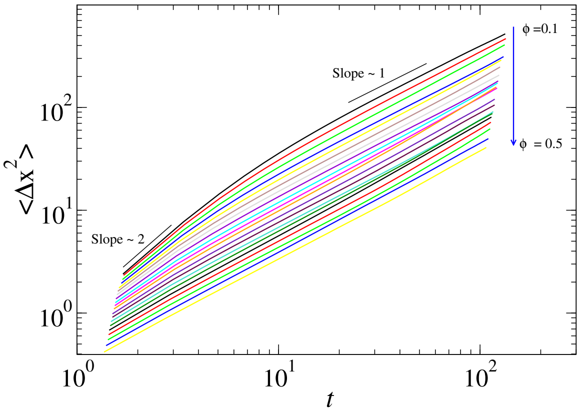

Figure 5.1: The MSD along the direction of the pore axis, as a function of t for $H_d = 1.1$ at different densities. The short line segments have slopes as indicated and are included as a guide to the eye.

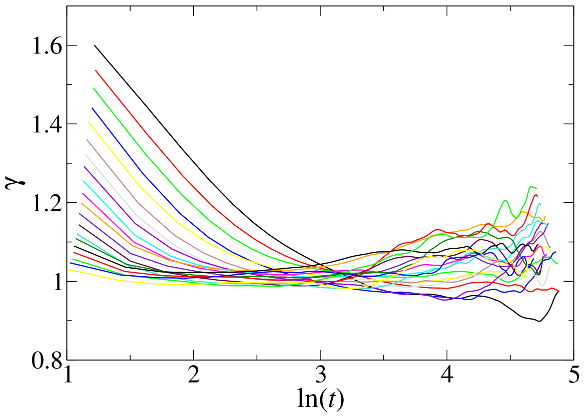

Figure 5.2: Slopes for MSD lines obtained using central difference method as a function of t for $H_d = 1.1$ at different densities.

nearest neighbor can interact. This also prevents the particles from passing each other.

One of the challenging features associated with dynamics is how it is connected into thermodynamics. Figure 5.3 shows the diffusion coefficient for the system at different values of the channel width. In general, as the system increases pressure and becomes more dense and the diffusion coefficient decreases. Necessarily, $D \to 0$ as $PV/Nk_\mathrm{B}T \to \infty$. But interestingly, the plateau in the EOS (see Fig. 3.5), which signifies a continuous structural transition from a linear to more zig–zag fluid structure, is mirrored in the plots of the diffusion coefficient. This suggest a strong connection between thermodynamics, structure and dynamics.

The exact equation for diffusion of particles in a purely one dimensional (1d) systems has been solved by Jepsen [263] and is given by:

$$\frac{D}{\sigma} = \frac{(1-\phi)}{\phi\,(2\pi\beta m)^{1/2}}, \tag{5.2}$$

where β is $[k_\mathrm{B}T]^{-1}$. Here $\phi = N\sigma/L$ $(V = L)$ in purely 1d.

For purely 1d systems, the exact EOS is $PV/Nk_\mathrm{B}T = \phi/\left(1-\phi\right)$, so the pressure diverges as close packed at $\phi = 1$ is approached. A similar scaling in quasi 1d would be

$$\frac{D}{\sigma} = \frac{(\phi_J-\phi)}{\phi\,(2\pi\beta m)^{1/2}}, \tag{5.3}$$

where ϕ_J is the jammed density that system samples at each density, which is given based

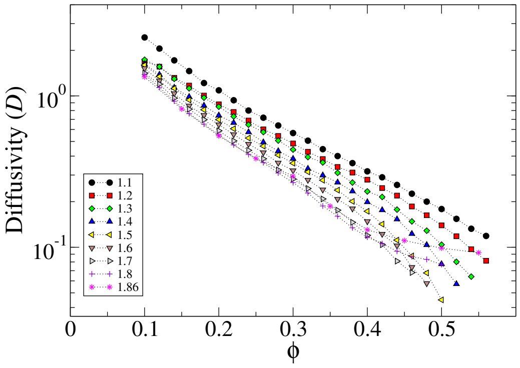

Figure 5.3: Diffusivity, D, vs. occupied volume fraction, ϕ, for various values of channel width, symbols are simulation data.

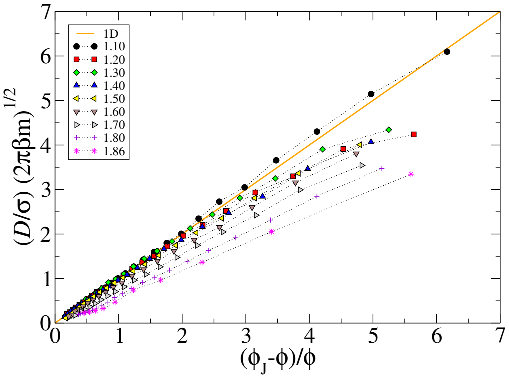

Figure 5.4: Rescaled diffusivity data using Eq. 5.3 for different values of channel diameter.

on the defect mole fraction as,

$$\phi_J = \frac{\pi}{4H_d\left(\theta + (1-\theta)\sqrt{H_d\left(2\sigma - H_d\right)}\right)}. \tag{5.4}$$

Figure 5.4 shows the predictions of Eq. 5.3, by where Eq. 5.4 has been used and the values of θ were obtained from the theory and simulations described in sections 3.5.1 and 3.6.1.

The exact EOS for the quasi–1d system was solved by Kofke and Post [151] using a transition matrix approach and was described in section 3.5.1 of this thesis.

In a sense, this is equivalent to projecting system to on 1d and finding the average diameter σ_N that maximize the entropy at a given density of the fluid (Fig. 5.5). Therefore, σ_N can be extracted from EOS and used instead of σ in Eq. 5.2:

$$\sigma_{\mathrm{N}} = \frac{1}{N}\sum_{i}^{N}\sigma_{\mathrm{i}}, \tag{5.5}$$

and the effective occupied volume fraction can be defined as:

$$\phi_{\mathrm{eff}} = \frac{N\sigma_{\mathrm{N}}}{L}. \tag{5.6}$$

To obtain an expression for ϕ_{eff}, it is assumed that the 1d EOS will hold, giving,

$$PV/Nk_{\mathrm{B}}T = \frac{1}{1-\phi_{\mathrm{eff}}}, \tag{5.7}$$

then ϕ_{eff} can be written as:

$$\phi_{\mathrm{eff}} = \frac{PV/Nk_{\mathrm{B}}T - 1}{PV/Nk_{\mathrm{B}}T}, \tag{5.8}$$

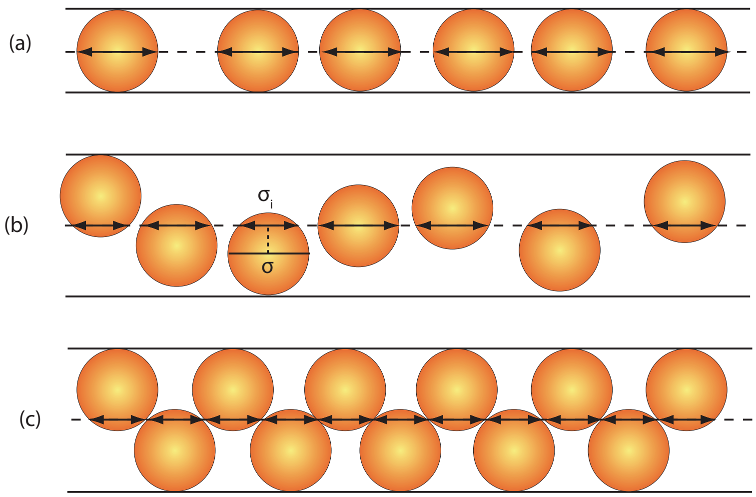

Figure 5.5: Effective diameter in a system of: purely 1d system $\sigma_{\text{eff}} = \sigma_i$ (a), system with $H_d/\sigma = 1.8$ in low density and a broad distribution of diameters (b), and system with $H_d/\sigma = 1.8$ at high density with narrow distribution of diameter.

by substituting eq. 5.6 into 5.2, the diffusion coefficient can be obtained:

$$\frac{D}{\sigma_{\text{N}}} = \frac{(1-\phi_{\text{eff}})}{\phi_{\text{eff}}(2\pi\beta m)^{1/2}}. \tag{5.9}$$

This final equation can be used to calculate the diffusion coefficient at different values of channel width. Figure 5.6 shows eq. 5.9 by using simulated data for the diffusion coefficient at different values of channel width compared to exact analytical results for 1d system. The plot shows that the collapse of the data is very good at high densities but it is not perfect at lower densities. This suggests ϕ_{eff} provides a good thermodynamic connection through the equation of state, to 1d diffusion. The deviation at low densities may be related to a broad distribution of effective diameters at low densities, which the average effective diameter extracted from EOS is not accurate.

5.4.2 Excess Entropy Scaling

As discussed before, earlier studies provided evidence that the scaling laws could indeed adequately describe the behavior of the dense, equilibrium fluid. Rosenfeld scaling predicts an approximate relationship, $D_{\text{R}} \approx 0.58 \exp(As^{\text{ex}})$, between the reduced diffusion coefficient, $D_{\text{R}} = DT^{-1/2}\rho^{1/3}$ (ρ is number density), and the excess entropy per particle, s^{ex}, for dense equilibrium fluid. The parameter A is a constant number for different model fluids. Dzugutov's scaling is given by $D_{\text{D}} \approx 0.078 \exp(s^{\text{ex}})$, and it relates a slightly different reduced

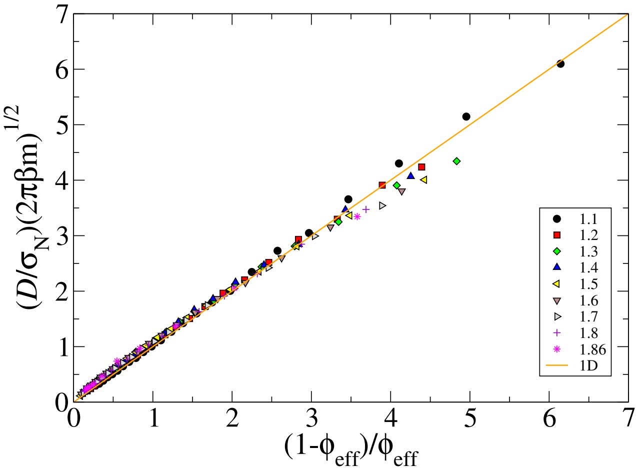

Figure 5.6: Scaled self–diffusion coefficient data using modified Jepson equation (eq. 5.8) for various values of channel widths.

self–diffusivity, $D_{\mathrm{D}} = D\rho^{2/3}\Gamma_{\mathrm{E}}^{-1}$, to the excess entropy per particle.

The excess entropy calculated for each channel diameter from it's equation of state using,

$$s^{\mathrm{ex}} = \int_0^{\phi_J} \frac{PV/Nk_{\mathrm{B}}T - 1}{\phi} \mathrm{d}\phi. \tag{5.10}$$

In addition, for a purely one dimensional system, the excess entropy with respect to the ideal gas can be obtained from:

$$s^{\mathrm{ex}} = \ln(1-\phi), \tag{5.11}$$

and from Eqs. 5.9 and 5.11, the diffusion coefficient based on the excess entropy for quasi one dimensional system can be express as:

$$D = \left(\sigma_N/\phi_{\mathrm{eff}}\right)\left(2\pi\beta m\right)^{-1/2}\exp\left(s^{\mathrm{ex}}\right). \tag{5.12}$$

This gives an equation connecting excess entropy to the diffusion coefficient. Figures 5.7 and 5.8 illustrate the variation of diffusion coefficients for different values of channel widths as a function of the excess entropy obtained from the two different methods calculated from Eqs. 5.10 and 5.11 respectively.

5.5 Conclusion

Simulations for dimensionless transport coefficients of fluids have a proven relationship with excess entropy, for bulk and wide channels. This study has presented evidence that the

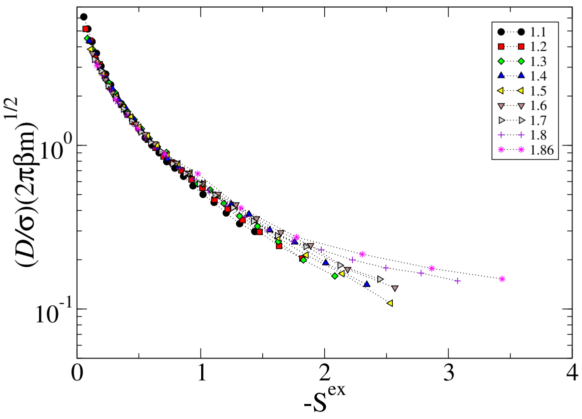

Figure 5.7: Scaled self–diffusion coefficient data versus negative excess entropy calculated from integration over equilibrium liquid EOS for various values of channel widths.

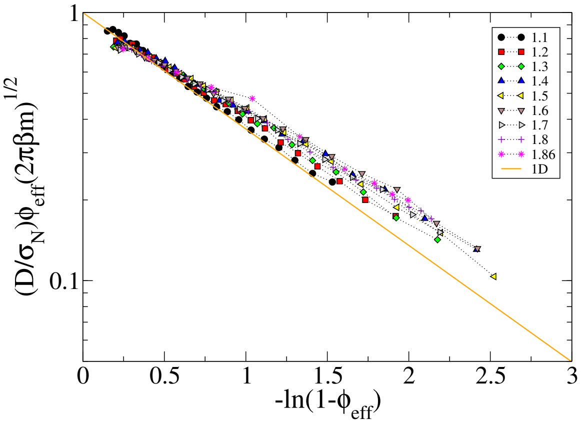

Figure 5.8: Scaled self–diffusion coefficient data versus negative excess entropy calculated using eq. 5.11 for various values of channel widths.

diffusion coefficient of highly confined systems (quasi–one dimensional) can be mapped onto the exact expression for a purely 1d through a scaling approach of the particle size that is obtained from the EOS. It has been found that the diffusivity of highly confined hard sphere systems as a function of effective diameter can collapse onto single line for a wide range of densities. The results shows the connection between dynamic behavior of this system into thermodynamic over a wide range of systems conditions.

Chapter 6

Conclusions and Outlook

6.1 Discussion

Bernal's [70] construction of random close packing (RCP) using ball bearing hard spheres highlighted the role particle packing may play in understanding the structure of liquids. Subsequent work on jamming phenomena [105,217,264,265] has shown that the ways particles pack together to form mechanically stable structures has important implications for the properties of fluids, glasses and athermal granular materials. In particular, the jamming phase diagram [89, 111, 112, 266] was introduced to establish a connection between the jamming in thermal and athermal systems. Packing problems have also found applications in computer science [267] and information theory [268].

Inherent structures [26, 110] provide an ideal framework that connects the properties of the equilibrium fluid with packings of particles by mapping every configuration of the equilibrium fluid to a mechanically stable structure. In a system with potential energy, an inherent structure is a local potential energy minimum obtained by quenching the system using a steepest descent or conjugate gradient energy minimization. In a hard particle system, a configuration is ideally mapped to its inherent structure by continually expanding the particles, moving them apart on contact, until they becomes collectively jammed [27] in a local maximum density maximum. Configurations that map to the same inherent structure are then grouped together in basins of attraction to form the jamming or packing landscape consisting of local density maxima separated by saddle points.

The thermodynamics and dynamics of the system are then described in terms of how the system moves around this high dimensionality landscape [4, 23]. For example, the Adam–Gibbs relation [29] suggests the slow down observed in the dynamics of supercooled fluids is related to the decrease in the number of accessible of inherent structure basins, N_J, through the configurational entropy, $S_c/Nk_{\mathrm{B}} = \ln N_J$. The landscape approach accounts for the possibility of an ideal glass transition to occur if N_J becomes sub–exponential so that $S_c/Nk_{\mathrm{B}} \to 0$. Unfortunately, the inherent structure mapping process for hard particles is difficult to implement for even small numbers of particles [110]. Computer simulation has been used extensively to investigate the distribution of inherent structures, but different compression protocols often lead to different conclusions for both hard disc mixtures [71–73] and hard spheres [74, 111]. While the density of RCP is highly reproducible, relationships between structure and the density of jammed packing suggest randomness is ill defined and it has been proposed that it should be replaced by the concept of a maximally jammed state [75]. Similarly, the existence of a continuous distribution of jammed states, from disordered packings through to the ordered crystal, in a model of hard discs mixtures appears to rule out the possibility of an ideal glass transition [73].

Replica mean field theory [95,96] (RMFT) provides a theoretical approach to understanding jamming in hard particles. Configurations of the fluid at ϕ are mapped to a jammed occupied volume fraction ϕ_J by considering a local cage–size parameter that momentarily traps the particle and is systematically taken to zero size under a series of mean field constraints. This effectively models the immobilization of a particle due to caging by its local neighbors and suggests there is a very narrow distribution of jammed structures in three dimensional hard spheres, which is consistent with recent simulations [106, 107].

RMFT introduced the distribution of jammed densities instead of single jammed point a (J–point) to the JPD by suggesting the existence of J–line. Also, it provided some interesting features that connect the thermodynamics of the systems to its dynamics. ϕ_d represents a density where the fluids begins to fall out of equilibrium and gets trapped in a inherent structure with density of ϕ_{th}. Despite the success of RMFT in predicting the existence of J–line, however, using quasi–one–dimensional systems in 2d and 3d, the current work suggests a more comprehensive picture regarding the inherent structure landscape. The complete distribution of inherent structures calculated for non–additive hard rods in Chapter 2, and for hard discs and hard spheres confined in narrow channel in Chapters 3 and 4 respectively. Based on the mapping techniques used, equilibrium liquids mapped to their inherent structures and finds that the equilibrium fluid cannot sample the entire inherent structure description and provides evidence of the extension of a J–line well below ϕ_{th}. For all of the systems studied, it is found that the ideal gas maps to the inherent structure with ϕ_J^* at the maximum of configurational entropy. The jammed states below this point exist, however, the equilibrium fluid cannot map to these structures due to maximum entropy condition. All of the inherent structures above ϕ_J^* are accessible from equilibrium fluid and depending on the compression rate system will map to one of the basins. At an infinitely slow compression rate, system maps to the inherent structure with the maximum density available, $\phi_{J\,\max}$. In addition, the inherent structure with the lowest density is located in the inaccessible region with $\phi_{J\,\min}$.

The dynamics of these systems is also of great interest. The dynamics of supercooled liquids is usually classified as being fragile or strong, depending on the temperature dependence of the structural relaxation time, or viscosity. However, in some systems, such as silica, silicon and water a dynamical crossover from fragile to strong behavior has been observed at a finite temperature. The crossover in these systems is located at the Widom line, which is characterized by a maximum in the response functions such as the heat capacity. There is considerable debate concerning the thermodynamic origin of the Widom line in the network forming systems. In particular, there is strong evidence to suggest some models of water exhibit a liquid–liquid phase transition between high and low density liquids. This would imply the existence of a critical point that could give rise to the thermodynamic behavior associated with the Widom line. However, the existence of a critical point is not a thermodynamic necessity for the existence of the heat capacity maximum. There is no underlying critical point associated with the fragile–strong crossover observed in the systems studied here. Furthermore, the simplicity of the hard sphere models suggest FS crossovers is more common that previously thought.

The facilitated dynamics paradigm suggests that relaxation and particle motion is driven by local microscopic dynamical rules rather than any underlying thermodynamics [57]. A key ingredient of FD is the presence of kinetically mobile regions that are able to influence the motion of neighboring regions, leading to the formation of chains of mobile particles in space–time. In addition, the theory argues that directed particle motion plays an important role. If a kinetically mobile region can activate or deactivate a neighboring region independent of any previous motion, it is considered to be directionally independent. Then the system behaves like a strong fluid and $\ln \tau \approx -\ln C_{FD}$, where C_{FD} is the concentration of kinetically excited regions. The expectation that structural relaxation in a fragile fluid is cooperative is captured by having directional correlation between the successive movement of particles in the kinetically excited regions. A FS crossover is predicted to occur when elements of both mechanisms are present in the system. While FD models have been parametrized to fit experimental data, only recently have there been efforts to identify the kinetically excited regions at a microscopic level [269, 270], and most studies of FD have focused on spin models where the dynamic rules are included by construction.

The current thesis suggest that the local packing environments of particles, along with the way they interact, may serve as the important microscopic ingredients in the FD paradigm and points to a new analysis that can be explored in higher dimensions. In the case of hard particles, it may be useful to identify local packing structures or local tilings in the jammed inherent structures [88] as defects. In particular, if neighboring defects are unstable the resulting irreversible local rearrangement of the particles could give rise to the direction motion thought to be responsible for the super–Arrhenius dynamics of a fragile fluid. Once the defect concentration is low (the saddle point index is also low) the dynamics crosses over to the reversible hopping of defects between locally stable environments. Simulations of bulk materials have also shown that local soft modes are spatially correlated with the highly mobile particles connected to dynamic heterogeneities [180–182].

The melting transition of two dimensional systems is described using KTHNY theory and it is consist of two–stage scenario. First the solid undergoes a continuous transition into a hexatic phase with quasi–long–range orientational order, then another continuous transition drives hexatic phase to disordered liquid phase. The dissociation of dislocation pairs (defects) plays a critical role in these transitions. It is generally accepted that quasi–one–dimensional systems with short range interactions cannot exhibit a phase transition. However, the work of this thesis shows that the system of hard spheres confined in a channel with $1 + \sqrt{3/4} < H_d/\sigma < 1.98$ exhibits a high order continuous transition from a disordered fluid to a translationally disordered, but orientationally ordered fluid with increasing density. The phase transition is entropically driven as system increases its vibrational entropy by sampling basins on the inherent structure landscape with a larger ϕ_J which, in this model, also results in increasing the orientational correlation. This is the same entropic driving force [249] that causes the bulk hard sphere system to freeze [63]. However, the configurational entropic advantage to having defects in the quasi–one–dimensional system prevents the formation of a solid phase. As a result, the system forms an orientationally ordered fluid containing defects, similar in nature to the hexatic phase except that the defects are never bound.

However, it is important to note that this work does not invalidate the results of van Hove and Landau. Their work is valid for systems with short range interactions. While the particle–particle interactions of the hard sphere system are short ranged, it is the collective entropic interactions that control the angles of rotation in the helix are determined on length scales associated with the separation of the defects, which can be long. This suggests that arguments of van Hove and Landau are not applicable in this case.

6.2 Conclusions

This thesis explored many unique aspects related to the dynamics and thermodynamics of confined geometries. Systems of two– and three–dimensional hard particles under an extreme confinement were studied. These systems were confined such that the first–order phase transition was avoided and can be used to study the fluid and glassy behavior of the systems. Thermodynamics and dynamics of these quasi–one dimensional systems were studied extensively using both analytical and numerical approaches and the following are some of the key findings.

6.2.1 Inherent Structure Landscape

The phase behavior of amorphous solid matter (jammed matter) is much less understood than its liquid and crystalline counterparts. Recently big advances in understanding jammed matter comes from the so called replica mean field theory (RMFT) of glasses postulated by Giorgio Parisi and co–workers [46,62,96,100,271]. Using a quasi one dimensional glass former, in this thesis, it is proposed that RMFT predicts only a partial phase diagram of jammed matter. A method of mapping a configuration of the equilibrium fluid to its inherent structure was developed and the distribution of jammed structure obtained. The full phase diagram of a system of hard discs and hard spheres was calculated in Chapters 3 and 4, respectively, and shows that large parts of the phase diagram are thermodynamically inaccessible or out of the purview of RMFT approximations. This work has shown the limitations of RMFT and the need for a more general theory of jammed matter. In addition, the important parts of this phase behavior, with its replica counterpart, was identified which clarify the various regimes predicted by replica theory and mode coupling theory in this exact model. However, the findings show that some predictions of RMFT, such as the glass closed pack structure do not exist in this exact model. In addition, this work leads to the surprising conclusion that the J–point is thermodynamically related, through inherent structure landscape, to the ideal gas rather than the glass transition.

6.2.2 Fragile–Strong Crossover

For over a decade now, fragility has been identified as a crucial issue regarding the glass forming ability of a liquid. This has resulted in a large body of research work focussing on the unclear origin and mechanism underlying fragility. For the systems studied in this thesis, dynamical properties were also measured using numerical methods. Chapter 3 demonstrates that in a system containing two–dimensional hard discs confined in a narrow channel, two distinct dynamical regimes are observed. At low densities, the system shows fragile behavior and at higher densities the dynamics of the system follows strong glass former behavior. Therefore, this change in dynamics of the system is identified as a fragile–strong crossover. Chapter 4 studied the dynamics in a hard sphere system confined in a narrow tube, for a tube with diameter range $1 + \sqrt{3/4} < H_d/\sigma < 1.98$, a similar crossover was identified. The crossover density was determined to be associated with the isobaric heat capacity maximum.

Using both computational and analytic methods it can be concluded that the dynamical crossover has a geometric origin, namely unstable dynamical modes arising out of defect dynamics. This work suggests that the local packing environments of particles, along with the way they interact, may serve as the important microscopic ingredients in the FD paradigm and points to a new analysis that can be explored in higher dimensions. These findings along with some other studies [125,183–185] strongly suggest local packing and particle geometries may play an important role in the dynamics of fluids in general.

6.2.3 Orientational Order Phase Transition

In hard spheres confined in a narrow channel system the fluid exhibits a phase transition from an isotropic fluid to an orientationally ordered fluid. Topological defects disrupt the translational order, but not the orientational order. The global packing constraints determine the helical angle of the inherent structures sampled by the fluid.

6.3 Future Outlook

The findings from this thesis have given rise to many new questions that should be addressed through future study. With all these predictions, further investigation is required to make a reliable comparison with the properties of bulk systems. The confined systems studied in this thesis were restricted in such a way that avoids a first–order phase transition in the system and were able to study the fluid and glassy phases. However, in bulk systems the true first–order phase transition exists and they go through a transition from a fluid to a crystal phase. The following addresses some of the future work that relates to the materials covered here.

6.3.1 Inherent Structure Landscape in Wider Channels

Extending the area of study to a wider channel will be interesting and can provide solutions to some of the unsolved problems in the field of soft and condensed matter. At wider channels, the landscape of the system is not just limited to the glassy materials and also the crystal state(s) exist, which make this model more similar to the bulk system.

Figure 6.1 shows the EOS of the system with $H_d/\sigma = 2.4$. As can be seen from this figure, the system goes shows a sign of a first order phase transition at $\phi \sim 0.45$. However, the heat capacity of the system (Fig. 6.2), apart from the discontinuity at this transition point, also includes two additional peaks. Understanding the origin of these peaks could provide informations about a more general phenomena at bulk systems.

Numerical simulations and experiments by Anikeenko and coworkers [74, 81] for equal–sized hard spheres inside a box have found that at the random close packing limit the system undergoes a structural reorganization and most of the particles are arranged in "quasiregular tetrahedra". Aste [272] also proposed tracking tetrahedra as a method for understanding particle pickings. It may be possible to use the tetrahedra formed by jammed particles in the confined channels, in combination with the transfer matrix method, to develop a complete description of the inherent structure distribution in these quasi–one–dimensional systems. By finding tile sets it will allow to use the transfer matrix method to construct the exact partition function for all the jammed states, and derive thermodynamics properties for glassy structure. Once the complete description of the inherent structure is known, molecular dynamics can be used to explore the landscape for the system, which is related to the dynamics of the dense fluid.

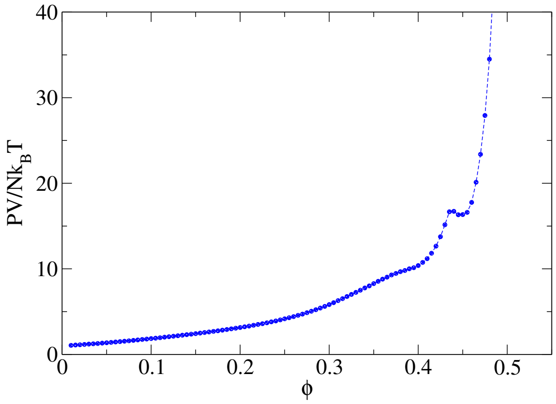

Figure 6.1: EOS for channel with $H_d/\sigma = 2.4$ as a function of density.

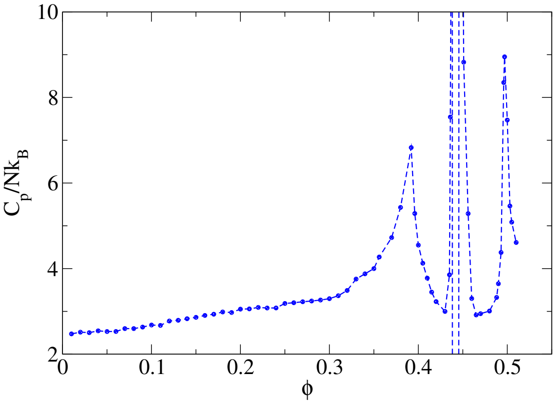

Figure 6.2: C_p for channel with $H_d/\sigma = 2.4$ as a function of density.

6.3.2 Theoretical Studies in Confined Geometry

Theoretical approaches to glass transition and jamming transition is described in Section 1.3. One of the successful theoretical approaches is MCT, which has been used extensively to study the slow complex dynamics of bulk systems [6, 10, 20] as well as confined systems [273, 274]. Many aspects of MCT have been confirmed by experiments and numerical studies, however many details regarding the rearranging of the local cages and CRR are not obvious. The models that have been described in this thesis, provide a reliable system to apply these theoretical approaches and test the validity of the approach and may discover some new features as well. The single input to MCT is the structure factor of the system, which for these models, is available analytically [153].

References

[1] R. Zallen, *The Physics of Amorphous Solids (Wiley Classics Library)*, Wiley-Interscience (1998).

[2] J. Crowe, J. Carpenter, and L. Crowe, "The role of vitrification in anhydrobiosis", *Annu Rev Physiol* **60**(1), pp. 73–103 (1998).

[3] L. Greer, "Metallic glasses", *Science* **267**(5206), pp. 1947–1953 (1995).

[4] P. G Debenedetti and F. H Stillinger, "Supercooled liquids and the glass transition", *Nature* **410**(6825), pp. 259–267 (2001).

[5] R. Johnston, "World's slowest-moving drop caught on camera at last", *Nature* (2013).

[6] W. Götze, "Complex Dynamics of Glass-Forming Liquids: A Mode-Coupling Theory" (2008).

[7] F. Mezei, W. Knaak, and B. Farago, "Neutron spin echo study of dynamic correlations near the liquid-glass transition", *Phys Rev Lett* **58**, pp. 571–574 (1987).

[8] J. P. Hansen and I. R. McDonald, *Theory of Simple Liquids*, Elsevier Science (2006).

[9] S. R Elliott, "The origin of the first sharp diffraction peak in the structure factor of covalent glasses and liquids", *J Phys Condens Matter* **4**, pp. 7661 (1992).

[10] D. R Reichman and P. Charbonneau, "Mode-coupling theory", *J. Stat. Mech* (2005).

[11] C. A. Angell, "Relaxation in liquids, polymers and plastic crystals - strong/fragile patterns and problems", *J Non-Cryst Solids* **131**, pp. 13 (1991).

[12] H. Vogel, "The law of the relation between the viscosity of liquids and the temperature", *Physikalische Zeitschrift* **22**, pp. 645 (1921).

[13] G.S Fulcher, "Analysis of Recent Measurements of the Viscosity of Glasses", *J Am Ceram Soc* **8**, pp. 339–355 (1925).

[14] G. Tammann and W. Hesse, "Die Abhängigkeit der Viscosität von der Temperatur bie unterkühlten Flüssigkeiten", *Zeitschrift für anorganische und allgemeine Chemie* **156**, pp. 245–257 (1926).

[15] I. Avramov, "Viscosity in disordered media", *J Non Cryst Solids* **351**(40-42), pp. 3163–3173 (2005).

[16] I. Avramov and A. Milchev, "Effect of disorder on diffusion and viscosity in condensed systems", *J Non Cryst Solids* **104**(2-3), pp. 253–260 (1988).

[17] Y. Elmatad, D. Chandler, and J. Garrahan, “Corresponding states of structural glass formers”, *J Phys Chem B* **113**(16), pp. 5563–5567 (2009).

[18] P. Taborek, R. N Kleiman, and D. J Bishop, “Power-law behavior in the viscosity of supercooled liquids”, *Phys Rev B Condens Matter* **34**, pp. 1835 (1986).

[19] F. Mallamace, C. Branca, C. Corsaro, N. Leone, J. Spooren, S.-H Chen, and H. E Stanley, “Transport properties of glass-forming liquids suggest that dynamic crossover temperature is as important as the glass transition temperature”, *Proc Natl Acad Sci USA* **107**(52), pp. 22457–22462 (2010).

[20] W. Gotze and L. Sjogren, “Relaxation processes in supercooled liquids”, *Rep Prog Phys* (1992).

[21] R. Speedy, “The entropy of a glass”, *Mol Phys* **80**(5), pp. 1105–1120 (1993).

[22] W. Kauzmann, “The nature of the glassy state and the behavior of liquids at low temperatures.”, *Chem Rev* **43**(2), pp. 219–256 (1948).

[23] P Debenedetti, *Metastable Liquids*, Princeton University Press (1996).

[24] A. Clarke and H. Jónsson, “Structural changes accompanying densification of random hard–sphere packings”, *Phys Rev E* **47**(6), pp. 3975–3984 (1993).

[25] M. Goldstein, “Viscous liquids and the glass transition: A potential energy barrier picture”, *J Chem Phys* **51**(9), pp. 3728–3739 (1969).

[26] F. Stillinger and Th. Weber, “Hidden structure in liquids”, *Phys Rev A* **25**(2), pp. 978–989 (1982).

[27] S. Torquato and F. H Stillinger, “Multiplicity of generation, selection, and classification procedures for jammed hard-particle packings”, *J Phys Chem B* **105**(47), pp. 11849–11853 (2001).

[28] F. Sciortino, “Potential energy landscape description of supercooled liquids and glasses”, *J Stat Mech* **05**, pp. 015 (2005).

[29] G. Adam and J. Gibbs, “On the temperature dependence of cooperative relaxation properties in glass-forming liquids”, *J Chem Phys* **43**(1), pp. 139–146 (1965).

[30] R. J Greet and D. Turnbull, “Test of Adam-Gibbs Liquid Viscosity Model with o-Terphenyl Specific-Heat Data”, *J Chem Phys* **47**, pp. 2185–2190 (1967).

[31] R. Richert and C. A Angell, “Dynamics of glass-forming liquids. V. On the link between molecular dynamics and configurational entropy”, *J Chem Phys* **108**, pp. 9016 (1998).

[32] R. J. Speedy, “The hard sphere glass transition”, *Mol Phys* **95**, pp. 169 (1998).

[33] S. Sastry, “The relationship between fragility, configurational entropy and the potential energy landscape of glass-forming liquids”, *Nature* **409**, pp. 164 (2001).

[34] A. Scala, F. W Starr, E. La Nave, F. Sciortino, and H. E Stanley, “Configurational entropy and diffusivity of supercooled water”, *Nature* **406**, pp. 166 (2000).

[35] C. M Roland, S. Capaccioli, M. Lucchesi, and R. Casalini, "Adam-Gibbs model for the supercooled dynamics in the ortho-terphenyl ortho-phenylphenol mixture.", *J Chem Phys* **120**(22), pp. 10640–10646 (2004).

[36] S. Mossa, E. La Nave, H. E Stanley, C. Donati, F. Sciortino, and P. Tartaglia, "Dynamics and configurational entropy in the Lewis-Wahnström model for supercooled orthoterphenyl", *Phys Rev E* **65**, pp. 41205 (2002).

[37] G. P Johari, "Contributions to the entropy of a glass and liquid, and the dielectric relaxation time", *J Chem Phys* **112**, pp. 7518 (2000).

[38] F. W Starr, J. F Douglas, and S. Sastry, "The relationship of dynamical heterogeneity to the adam-gibbs and random first-order transition theories of glass formation", *J Chem Phys* **138**(12) (2013).

[39] Sh. Sengupta, S. Karmakar, Ch. Dasgupta, and S. Sastry, "Adam-Gibbs Relation for Glass-Forming Liquids in Two, Three, and Four Dimensions", *Phys Rev Lett* **109**(9), pp. 095705 (2012).

[40] S. Sastry, P. G Debenedetti, and F. H Stillinger, "Signatures of distinct dynamical regimes in the energy landscape of a glass-forming liquid", *Nature* **393**(6685), pp. 554–557 (1998).

[41] W. Kob, S. Roldán-Vargas, and L. Berthier, "Non-monotonic temperature evolution of dynamic correlations in glass-forming liquids", *Nat Phys* **8**, pp. 164 (2012).

[42] T. R Kirkpatrick and D. Thirumalai, "Dynamics of the structural glass transition and the p-spin-interaction spin-glass model", *Phys Rev Lett* **58**, pp. 2091 (1987).

[43] T.R. Kirkpatrick and P. G Wolynes, "Connections between some kinetic and equilibrium theories of the glass transition", *Phys Rev A Gen Phys* **35**, pp. 3072 (1987).

[44] V. Lubchenko and P. G Wolynes, "Theory of Structural Glasses and Supercooled Liquids", *Annu Rev Phys Chem* **58**(1), pp. 235–266 (2007).

[45] G. Biroli and J. Bouchaud, *The Random First-Order Transition Theory of Glasses: A Critical Assessment* , pp. 31–113, John Wiley & Sons, Inc. (2012).

[46] M. Mézard and G. Parisi, *Glasses and Replicas* , pp. 151–191, John Wiley & Sons, Inc. (2012).

[47] T. R Kirkpatrick and D. Thirumalai, "Comparison between dynamical theories and metastable states in regular and glassy mean-field spin models with underlying first-order-like phase transitions", *Phys Rev A Gen Phys* **37**(1), pp. 4439–4448 (1988).

[48] T. R Kirkpatrick and D. Thirumalai, "Mean-field soft-spin Potts glass model: Statics and dynamics", *Phys Rev B Condens Matter* **37**(1), pp. 5342–5350 (1988).

[49] T. R Kirkpatrick and P. G Wolynes, "Stable and metastable states in mean-field Potts and structural glasses", *Phys Rev B Condens Matter* **36**(1), pp. 8552–8564 (1987).

[50] J. Jäckle and S. Eisinger, "A hierarchically constrained kinetic ising model", *Zeitschrift für Physik B Condensed Matter* **84**, pp. 115 (1991).

[51] G. H Fredrickson and H. C Andersen, “Kinetic ising model of the glass transition”, *Phys Rev Lett* **53**, pp. 1244 (1984).

[52] W. Kob and H. C Andersen, “Kinetic lattice-gas model of cage effects in high-density liquids and a test of mode-coupling theory of the ideal-glass transition”, *Phys Rev E* **48**, pp. 4364 (1993).

[53] S. Glotzer, “Spatially heterogeneous dynamics in liquids: insights from simulation”, *J Non Cryst Solids* **274**, pp. 342 (2000).

[54] T. B Schrøder, S. Sastry, J. C Dyre, and S. C Glotzer, “Crossover to potential energy landscape dominated dynamics in a model glass-forming liquid”, *J Chem Phys* **112**, pp. 9834 (2000).

[55] C. Donati, S. C Glotzer, P. H Poole, W. Kob, and S. J Plimpton, “Spatial correlations of mobility and immobility in a glass-forming lennard-jones liquid”, *Phys Rev E* **60**, pp. 3107 (1999).

[56] J. P Garrahan and D. Chandler, “Geometrical explanation and scaling of dynamical heterogeneities in glass forming systems”, *Phys Rev Lett* **89**, pp. 35704 (2002).

[57] J. P Garrahan and D. Chandler, “Coarse-grained microscopic model of glass formers.”, *Proc Natl Acad Sci USA* **100**(17), pp. 9710–9714 (2003).

[58] M. Merolle, J. P Garrahan, and D. Chandler, “Space-time thermodynamics of the glass transition”, *Proc Natl Acad Sci USA* **102**, pp. 10837 (2005).

[59] D. Chandler and J. P Garrahan, “Thermodynamics of coarse-grained models of supercooled liquids.”, *J Chem Phys* **123**(4), pp. 044511–044511 (2005).

[60] D. Chandler and J. P Garrahan, “Dynamics on the Way to Forming Glass: Bubbles in Space-Time”, *Annu Rev Phys Chem* **61**, pp. 191–217 (2010).

[61] F.S. Stillinger and P.G. Debenedetti, “Glass transition thermodynamics and kinetics”, *Annu Rev Condens Matter Phys* **4**, pp. 263 (2013).

[62] G. Parisi and F. Zamponi, “A replica approach to glassy hard spheres”, *J Stat Mech* **2009**(03), pp. P03026 (2009).

[63] B.J. Alder and T.E. Wainwright, “Phase transition for a hard sphere system”, *J Chem Phys* **27**, pp. 1208 (1957).

[64] E.G. Noya, Carlos Vega, and Enrique de Miguel, “Determination of the melting point of hard spheres from direct coexistence simulation methods”, *J Chem Phys* **128**(15), pp. 154507 (2008).

[65] F. Stillinger, “Exponential multiplicity of inherent structures”, *Phys Rev E* **59**(1), pp. 48–51 (1999).

[66] J. Kepler, *The Six-cornered snowflake: Strena, seu de Nive sexangula*, Clarendon press (1966).

[67] T. C. Hales, “A proof of the kepler conjecture”, *Ann. of Math. (2)* **162**(3), pp. 1065–1185 (2005).

[68] W. Barlow, "Probable nature of the internal symmetry of crystals", *Nature* **29**, pp. 186 (1883).

[69] T. Aste and D. Weaire, *The pursuit of perfect packing*, IOP publishing (2000).

[70] J. D Bernal and J. Mason, "Packing of spheres: co-ordination of randomly packed spheres", *Nature* **188**, pp. 910–911 (1960).

[71] R. J Speedy, "Configurational entropy and diffusion in a hard disc fluid", *J Chem Phys* **114**, pp. 9069 (2001).

[72] N. Xu, J. Blawzdziewicz, and C. O'Hern, "Random close packing revisited: Ways to pack frictionless disks", *Phys Rev E* **71**(6), pp. 061306 (2005).

[73] A. Donev, F. H Stillinger, and S. Torquato, "Do Binary Hard Disks Exhibit an Ideal Glass Transition?", *Phys Rev Lett* **96**(22), pp. 225502 (2006).

[74] A. V Anikeenko, N. N Medvedev, and T. Aste, "Structural and entropic insights into the nature of the random-close-packing limit", *Phys Rev E* **77**(3), pp. 031101 (2008).

[75] S. Torquato, T. M Truskett, and P. G Debenedetti, "Is Random Close Packing of Spheres Well Defined?", *Phys Rev Lett* **84**(10), pp. 2064–2067 (2000).

[76] B. D Lubachevskyv and F. H Stillinger, "Geometric properties of random disk packings", *J Stat Phys* **60**, pp. 561–583 (1990).

[77] A. Donev, S. Torquato, and F. Stillinger, "Neighbor list collision-driven molecular dynamics simulation for nonspherical hard particles. i. algorithmic details", *J Comput Phys* **202**(2), pp. 737–764 (2005).

[78] A. Donev, S. Torquato, F.H. Stillinger, and R. Connelly, "A linear programming algorithm to test for jamming in hard-sphere packings", *J Comput Phys* **197**(1), pp. 139 – 166 (2004).

[79] A. Donev, R. Connelly, F.H. Stillinger, and S. Torquato, "Underconstrained jammed packings of nonspherical hard particles: Ellipses and ellipsoids", *Phys Rev E* **75**, pp. 51304 (2007).

[80] M. Skoge, A. Donev, F. H Stillinger, and S. Torquato, "Packing hyperspheres in high-dimensional euclidean spaces", *Phys Rev E* **74**(4), pp. 041127 (2006).

[81] A. Anikeenko and N. Medvedev, "Structure of hard sphere packings near bernal density", *J Struct Chem* **50**(4), pp. 761–768 (2009).

[82] R. K Bowles and R. Speedy, "Five discs in a box", *Physica A* **262**(1-2), pp. 76–87 (1999).

[83] N. N. Arkus, V. N. Manoharan, and M. P. Brenner, "Minimal energy clusters of hard spheres with short range attractions.", *Phys Rev Lett* **103**(11), pp. 118303–118303 (2009).

[84] N. Arkus, V. N. Manoharan, and M. P. Brenner, "Deriving Finite Sphere Packings", *SIAM J Discrete Math* **25**, pp. 1860–1901 (2011).

[85] G. Meng, N. Arkus, M. P. Brenner, and V. N. Manoharan, "The Free–Energy Landscape of Clusters of Attractive Hard Spheres", *Science* **327**, pp. 560 (2010).

[86] R. K Bowles and I. Saika-Voivod, "Landscapes, dynamic heterogeneity, and kinetic facilitation in a simple off-lattice model", *Phys Rev E* **73**(1), pp. 011503 (2006).

[87] Ashwin S S. and R. Bowles, "A tiling approach to counting inherent structures in hard potential systems", *J Non Cryst Solids* (2009).

[88] Ashwin S S and R. K Bowles, "Complete Jamming Landscape of Confined Hard Discs", *Phys Rev Lett* **102**, pp. 235701 (2009).

[89] A. J Liu and S. R Nagel, "Nonlinear dynamics - Jamming is not just cool any more", *Nature* **396**(6706), pp. 21–22 (1998).

[90] V. Trappe, V. Prasad, L. Cipelletti, P. N Segre, and D. A Weitz, "Jamming phase diagram for attractive particles", *Nature* **411**(6839), pp. 772–775 (2001).

[91] At. Ikeda, L. Berthier, and G. Biroli, "Dynamic criticality at the jamming transition.", *J Chem Phys* **138**(12), pp. 12A507–12A507 (2013).

[92] C. Coulais, R. P Behringer, and O. Dauchot, "The Jamming point street-lamp in the world of granular media", *arXiv* (2013).

[93] J. A Drocco, M. B Hastings, C. J Reichhardt, and C. Reichhardt, "Multiscaling at Point J: Jamming is a Critical Phenomenon", *Phys Rev Lett* **95**(8), pp. 88001 (2005).

[94] R. Mari, F. Krzakala, and J. Kurchan, "Jamming versus Glass Transitions", *Phys Rev Lett* **103**(2), pp. 025701 (2009).

[95] G. Parisi and F. Zamponi, "The ideal glass transition of hard spheres.", *J Chem Phys* **123**(14), pp. 144501 (2005).

[96] G. Parisi and F. Zamponi, "Mean-field theory of hard sphere glasses and jamming", *Rev Mod Phys* **82**(1), pp. 789–845 (2010).

[97] L. Berthier, H. Jacquin, and F. Zamponi, "Microscopic theory of the jamming transition of harmonic spheres", *Phys Rev E* **84**(5) (2011).

[98] H. Jacquin, L. Berthier, and F. Zamponi, "Microscopic mean-field theory of the jamming transition", *Phys Rev Lett* **106**(13), pp. 135702 (2011).

[99] L. Berthier, H. Jacquin, and F. Zamponi, "Can the jamming transition be described using equilibrium statistical mechanics?", *J Stat Mech* **2011**(1), pp. 004 (2011).

[100] I. Biazzo, F. Caltagirone, G. Parisi, and F. Zamponi, "Theory of Amorphous Packings of Binary Mixtures of Hard Spheres", *Phys Rev Lett* **102**(19), pp. 195701 (2009).

[101] F. Zamponi, "Some recent theoretical results on amorphous packings of hard spheres", *Philos Mag* **87**(3-5), pp. 485–495 (2007).

[102] M. Mezard and G. Parisi, "A first-principle computation of the thermodynamics of glasses", *J Chem Phys* (1999).

[103] M. Mezard and G. Parisi, “Thermodynamics of glasses: A first principles computation”, *Phys Rev Lett* **82**(4), pp. 747–750 (1999).

[104] F. Krzakala and J. Kurchan, “Landscape analysis of constraint satisfaction problems”, *Phys Rev E* **76**, pp. 21122 (2007).

[105] M. Pica Ciamarra, A. Coniglio, and A. De Candia, “Disordered jammed packings of frictionless spheres”, *Soft Matter* **6**(13), pp. 2975 (2010).

[106] P. Chaudhuri, L. Berthier, and S. Sastry, “Jamming Transitions in Amorphous Packings of Frictionless Spheres Occur over a Continuous Range of Volume Fractions”, *Phys Rev Lett* **104**(16), pp. 165701 (2010).

[107] C. F Schreck, C. S O’Hern, and L. E Silbert, “Tuning jammed frictionless disk packings from isostatic to hyperstatic.”, *Phys Rev E* **84**(1 Pt 1), pp. 011305 (2011).

[108] C. Austen Angell, “Entropy and fragility in supercooling liquids”, *J Res Natl Inst Stand Technol* **102**(2), pp. 171–185 (1997).

[109] M. Goldstein, “Viscous liquids and the glass transition: A potential energy barrier picture”, *J Chem Phys* **51**(9), pp. 3728–3739 (1969).

[110] F. H Stillinger, E. A DiMarzio, and R. L Kornegay, “Systematic Approach to Explanation of the Rigid Disk Phase Transition”, *J Chem Phys* **40**(6), pp. 1564–1576 (1964).

[111] C. S O’Hern, S. A Langer, A. J Liu, and S. R Nagel, “Random packings of frictionless particles”, *Phys Rev Lett* **88**(7), pp. 075507 (2002).

[112] C. S O’Hern, L. E Silbert, A. J Liu, and S. R Nagel, “Jamming at zero temperature and zero applied stress: The epitome of disorder”, *Phys Rev E* **68**(1), pp. 011306 (2003).

[113] T.M. Truskett, P.G. Debenedetti, and S. Torquato, “Thermodynamic implications of confinement for a waterlike fluid”, *J Chem Phys* **114**, pp. 2401 (2001).

[114] Y. Jiao, F. H. Stillinger, and S. Torquato, “Nonuniversality of density and disorder in jammed sphere packings”, *J Appl Phys* **109**, pp. 3508 (2011).

[115] A. Cavagna, “Fragile vs. strong liquids: A saddles-ruled scenario”, *Europhys Lett* **53**, pp. 490 (2001).

[116] S. Franz and M. A Virasoro, “Quasi-equilibrium interpretation of ageing dynamics”, *J. Phys. A: Math. Gen.* **33**, pp. 891 (2000).

[117] A. Cavagna, I. Giardina, and G. Parisi, “Stationary points of the thouless-anderson-palmer free energy”, *Phys Rev B Condens Matter Phys* **57**, pp. 1123612 (1998).

[118] J. Kurchan and L. Laloux, “Phase space geometry and slow dynamics”, *J. Phys. A: Math. Gen.* **29**, pp. 1929 (1996).

[119] I. Saika-Voivod, P. H Poole, and F. Sciortino, “Fragile-to-strong transition and polyamorphism in the energy landscape of liquid silica”, *Nature* **412**(6846), pp. 514–517 (2001).

[120] I. Saika-Voivod, F. Sciortino, and P. H Poole, “Free energy and configurational entropy of liquid silica: Fragile-to-strong crossover and polyamorphism”, *Phys Rev E* **69**(4), pp. 41503 (2004).

[121] S. Sastry and C. A Angell, “Liquid–liquid phase transition in supercooled silicon”, *Nat Mater* **2**(11), pp. 739–743 (2003).

[122] L. Xu, P. Kumar, S. V Buldyrev, S. H Chen, P. H Poole, F. Sciortino, and H. E Stanley, “Relation between the Widom line and the dynamic crossover in systems with a liquid-liquid phase transition”, *Proc Natl Acad Sci USA* **102**(46), pp. 16558–16562 (2005).

[123] H. E Stanley, P. Kumar, G. Franzese, L. Xu, Z. Yan, M. G Mazza, S. V Buldyrev, S. H Chen, and F. Mallamace, “Liquid polyamorphism: Possible relation to the anomalous behaviour of water”, *Eur Phys J-Spec Top* **161**, pp. 1–17 (2008).

[124] C. A Angell, “Insights into Phases of Liquid Water from Study of Its Unusual Glass-Forming Properties”, *Science* **319**(5863), pp. 582–587 (2008).

[125] P. H Poole, S. R Becker, F. Sciortino, and F. W Starr, “Dynamical Behavior Near a Liquid–Liquid Phase Transition in Simulations of Supercooled Water”, *J Phys Chem B* **115**(48), pp. 14176–14183 (2011).

[126] Ashwin S S and S. Sastry, “Low-temperature behaviour of the Kob Andersen binary mixture”, *J Phys Condens Matter* **15**(11), pp. S1253–S1258 (2003).

[127] M. Zaeifi Yamchi, Ashwin S S., and R. K Bowles, “Fragile-strong fluid crossover and universal relaxation times in a confined hard-disk fluid”, *Phys Rev Lett* **109**, pp. 225701 (2012).

[128] Ashwin S S., M. Zaeifi Yamchi, and R. K. Bowles, “Inherent structure landscape connection between liquids, granular materials, and the jamming phase diagram”, *Phys Rev Lett* **110**, pp. 145701 (2013).

[129] M Zaeifi Yamchi, Ashwin S S, and R. K Bowles, “The inherent structures, fluids, glasses and jamming: Insights from quasi-one-dimensional hard disks”.

[130] I. Prigogine, *The Molecular Theory of Solutions*, North-Holland Publishing Company,; New York (1957).

[131] J. K Percus, “Equilibrium state of a classical fluid of hard rods in an external field”, *J Stat Phys* **15**(6), pp. 505–511 (1976).

[132] J. K Percus, “One-dimensional classical fluid with nearest-neighbor interaction in arbitrary external field”, *J Stat Phys* **28**(1), pp. 67–81 (1982).

[133] R. Roth, R. Evans, and A. A Louis, “Theory of asymmetric nonadditive binary hard–sphere mixtures”, *Phys Rev E* (2001).

[134] M. Heying and D. S. Corti, “The one-dimensional fully non-additive binary hard rod mixture: exact thermophysical properties”, *Fluid Phase Equilib* **220**(1), pp. 83–101 (2004).

[135] M. Schmidt, "Fundamental measure density functional theory for nonadditive hard-core mixtures: The one-dimensional case", *Phys Rev E* **76**(3), pp. 31202 (2007).

[136] R. K. Bowles, "A thermodynamic description of the glass transition: an exact one-dimensional example", *Physica A* **275**, pp. 217 – 228 (2000).

[137] L. Tonks, "The Complete Equation of State of One, Two and Three-Dimensional Gases of Hard Elastic Spheres", *Physical Review* **50**, pp. 955 (1936).

[138] G. Rutkai and T. Csányi, É.and Kristóf, "Prediction of adsorption and separation of water–alcohol mixtures with zeolite NaA", *Microporous and Mesoporous Materials* **114**(1-3), pp. 455–464 (2008).

[139] B. Smit, "Simulating the adsorption isotherms of methane, ethane, and propane in the zeolite silicalite", *J Phys Chem* (1995).

[140] R. Evans, "Fluids adsorbed in narrow pores: phase equilibria and structure", *J Phys-Condens Mat* **2**(46), pp. 8989–9007 (1990).

[141] P. M König, R. Roth, and K. Mecke, "Morphological Thermodynamics of Fluids: Shape Dependence of Free Energies", *Phys Rev Lett* **93**(16), pp. 160601 (2004).

[142] J. A Given, "On the thermodynamics of fluids adsorbed in porous media", *J Chem Phys* **102**(7), pp. 2934–2945 (1995).

[143] R. L Smith, C. J Demers, and S. D Collins, "Microfluidic device for the combinatorial application and maintenance of dynamically imposed diffusional gradients", *Microfluidics and Nanofluidics* **9**(4-5), pp. 613–622 (2010).

[144] M. B Romanowsky, M. Heymann, A. R Abate, A. T Krummel, S. Fraden, and D. A Weitz, "Functional patterning of PDMS microfluidic devices using integrated chemomasks", *Lab Chip* **10**(12), pp. 1521–1524 (2010).

[145] R. Allen, S. Melchionna, and J.-P Hansen, "Intermittent Permeation of Cylindrical Nanopores by Water", *Phys Rev Lett* **89**(1), pp. 175502 (2002).

[146] G. Hummer, J. C Rasaiah, and J. P Noworyta, "Water conduction through the hydrophobic channel of a carbon nanotube", *Nature* **414**(6860), pp. 188–190 (2001).

[147] H. Kyakuno, K. Matsuda, H. Yahiro, Y. Inami, T. Fukuoka, Y. Miyata, K. Yanagi, Y. Maniwa, H. Kataura, T. Saito, M. Yumura, and S. Iijima, "Confined water inside single-walled carbon nanotubes: global phase diagram and effect of finite length.", *J Chem Phys* **134**(24), pp. 244501 (2011).

[148] M. Majumder, N. Chopra, and B. J Hinds, "Mass Transport through Carbon Nanotube Membranes in Three Different Regimes: Ionic Diffusion and Gas and Liquid Flow", *Acs Nano* **5**(5), pp. 3867–3877 (2011).

[149] D. Boda, W. Nonner, D. Henderson, B. Eisenberg, and D. Gillespie, "Volume Exclusion in Calcium Selective Channels", *Biophysical Journal* **94**(9), pp. 3486–3496 (2008).

[150] B. Hille, *Ion channels of excitable membranes*, Sinauer (2001).

[151] D. A Kofke and A. J Post, "Hard particles in narrow pores. transfermatrix solution and the periodic narrow box", *J Chem Phys* **98**, pp. 4853 (1993).

[152] P. Gurin and S. Varga, "Pair correlation functions of two- and three-dimensional hard-core fluids confined into narrow pores: Exact results from transfer-matrix method", *J Chem Phys* **139**, pp. 244708 (2013).

[153] S. Varga, G. Balló, and P. Gurin, "Structural properties of hard disks in a narrow tube", *J Stat Mech* **2011**(11), pp. P11006 (2011).

[154] M. J Godfrey and M. A Moore, "Static and dynamical properties of a hard-disk fluid confined to a narrow channel", *Phys Rev E* **89**(3), pp. 032111 (2014).

[155] K. K Mon and J. K Percus, "Hard-sphere fluids in very narrow cylindrical pores", *J Chem Phys* **112**, pp. 3457 (2000).

[156] K. K Mon and J. K Percus, "Soluble stochastic dynamics of quasi-one-dimensional single-file fluid self-diffusion", *J Chem Phys* **122**(21), pp. 214503 (2005).

[157] K K Mon and J K Percus, "Pore-size dependence of quasi-one-dimensional single-file diffusion mobility", *J Phy Chem C* **111**(43), pp. 15995–15997 (2007).

[158] K. K Mon and J. K Percus, "Hopping times of two hard disks diffusing in a channel", *J Chem Phys* **125**, pp. 244704 (2006).

[159] K. K Mon and J. K Percus, "Molecular dynamics simulation of anomalous self-diffusion for single-file fluids", *J Chem Phys* **119**, pp. 3343 (2003).

[160] K. K Mon and Jerome K Percus, "Hopping time of a hard disk fluid in a narrow channel", *J Chem Phys* **127**, pp. 4702 (2007).

[161] K. K Mon and Jerome K Percus, "Self-diffusion of fluids in narrow cylindrical pores", *J Chem Phys* **117**, pp. 2289 (2002).

[162] C. D Ball, N. D MacWilliam, Jerome K Percus, and Richard K Bowles, "Normal and anomalous diffusion in highly confined hard disk fluid mixtures", *J Chem Phys* **130**, pp. 4504 (2009).

[163] S. F Edwards and D. V Grinev, "Statistical mechanics of vibration-induced compaction of powders", *Phys Rev E* **58**(4), pp. 4758–4762 (1998).

[164] R. K Bowles and Ashwin S S, "Edwards entropy and compactivity in a model of granular matter", *Phys Rev E* **83**(3), pp. 031302 (2011).

[165] R. M Irastorza, C. M Carlevaro, and L. A Pugnaloni, "Exact predictions from the Edwards ensemble versus realistic simulations of tapped narrow two-dimensional granular columns", *J Stat Mech* **2013**(12), pp. P12012 (2013).

[166] N. Gundlach, M.l Karbach, D. Liu, and G. Müller, "Jammed disks in a narrow channel: criticality and ordering tendencies", *J Stat Mech* **04**, pp. 018 (2013).

[167] J. A Barker, "Statistical Mechanics of Almost One-dimensional Systems", *Aust J Chem* **15**(2), pp. 127 (1962).

[168] F. Sciortino and P. Tartaglia, "Harmonic Dynamics in Supercooled Liquids: The Case of Water", *Phys Rev Lett* **78**(12), pp. 2385–2388 (1997).

[169] C. Donati, F. Sciortino, and P. Tartaglia, "Role of Unstable Directions in the Equilibrium and Aging Dynamics of Supercooled Liquids", *Phys Rev Lett* **85**(7), pp. 1464–1467 (2000).

[170] L. Angelani, R. Di Leonardo, G. Ruocco, A. Scala, and F. Sciortino, "Saddles in the Energy Landscape Probed by Supercooled Liquids", *Phys Rev Lett* **85**(25), pp. 5356–5359 (2000).

[171] K. Broderix, K. K Bhattacharya, A. Cavagna, A. Zippelius, and I. Giardina, "Energy Landscape of a Lennard-Jones Liquid: Statistics of Stationary Points", *Phys Rev Lett* **85**(2), pp. 5360–5363 (2000).

[172] W. Kob, "Testing mode-coupling theory for a supercooled binary Lennard-Jones mixture I: The van Hove correlation function", *Phys Rev E* **51**(5), pp. 4626–4641 (1995).

[173] M. S Shell, P. G Debenedetti, E. La Nave, and F. Sciortino, "Energy landscapes, ideal glasses, and their equation of state", *J Chem Phys* **118**(19), pp. 8821–8830 (2003).

[174] Z. W Salsburg and W. W Wood, "Equation of State of Classical Hard Spheres at High Density", *J Chem Phys* **37**, pp. 798 (1962).

[175] Y. S. Elmatad, D. Chandler, and J. P. Garrahan, "Corresponding States of Structural Glass Formers. II", *J Phys Chem B* **114**(51), pp. 17113–17119 (2010).

[176] Sh. Sengupta, S. Karmakar, Ch. Dasgupta, and S. Sastry, "Breakdown of the Stokes-Einstein relation in two, three, and four dimensions", *J Chem Phys* **138**(12), pp. 12A548 (2013).

[177] T. Kirkpatrick, D. Thirumalai, and P. Wolynes, "Scaling concepts for the dynamics of viscous liquids near an ideal glassy state", *Phys Rev A* **40**(2), pp. 1045–1054 (1989).

[178] M. P Ciamarra and A. Coniglio, "Random very loose packings", *Phys Rev Lett* **101**(12), pp. 128001 (2008).

[179] Z. Chen, C. A Angell, and R. Richert, "On the dynamics of liquids in their viscous regime approaching the glass transition", *Eur Phys J E* **35**(7), pp. 65 (2012).

[180] A. Widmer-Cooper, H. Perry, P. Harrowell, and D. R Reichman, "Irreversible reorganization in a supercooled liquid originates from localized soft modes", *Nat Phys* **4**(9), pp. 711–715 (2008).

[181] A. Widmer-Cooper and P. Harrowell, "Central role of thermal collective strain in the relaxation of structure in a supercooled liquid", *Phys Rev E* **80**(6), pp. 061501 (2009).

[182] M. D Ediger and P. Harrowell, "Perspective: Supercooled liquids and glasses", *J Chem Phys* **137**(8), pp. 080901–080901–15 (2012).

[183] F. H Stillinger and A. Rahman, "Improved simulation of liquid water by molecular dynamics", *J Chem Phys* **60**(4), pp. 1545–1557 (1974).

[184] C. De Michele, S. Gabrielli, P. Tartaglia, and F. Sciortino, “Dynamics in the presence of attractive patchy interactions”, *J Phys Chem B* **110**(15), pp. 8064–8079 (2006).

[185] F. W Starr and F. Sciortino, “Model for assembly and gelation of four-armed DNA dendrimers”, *J Phys-Condens Mat* **18**(26), pp. L347–L353 (2006).

[186] E. Tondl, M. Ramsay, P. Harrowell, and A. Widmer-Cooper, “Defect-mediated relaxation in the random tiling phase of a binary mixture: Birth, death and mobility of an atomic zipper”, *J. Chem. Phys.* **140**(10), pp. 104503 (2014).

[187] G. T Pickett, M. Gross, and H. Okuyama, “Spontaneous chirality in simple systems”, *Phys Rev Lett* **85**, pp. 3652 (2000).

[188] A. Mughal, H. K Chan, and D. Weaire, “Phyllotactic description of hard sphere packing in cylindrical channels”, *Phys Rev Lett* **106**, pp. 115704 (2011).

[189] H. K Chan, D. Weaire, S. Hutzler, and A. Mughal, “Dense packings of spheres in cylinders: Simulations”, *Phys Rev E* **85**(5), pp. 051305 (2012).

[190] H. K Chan, “Densest columnar structures of hard spheres from sequential deposition”, *Phys Rev E* **84**, pp. 50302 (2011).

[191] H. K Chan, “A hybrid helical structure of hard sphere packing from sequential deposition”, *Philos Mag* (ahead-of-print), pp. 1–13 (2013).

[192] M. A Lohr, A. M Alsayed, B. G Chen, Z. Zhang, R. D Kamien, and A. G Yodh, “Helical packings and phase transformations of soft spheres in cylinders”, *Phys Rev E* **81**, pp. 40401 (2010).

[193] L. Jiang, J. W J de Folter, J. Huang, A. P Philipse, W. K Kegel, and A. V Petukhov, “Helical colloidal sphere structures through thermo-reversible co-assembly with molecular microtubes”, *Angew Chem Int Ed Engl* **52**(12), pp. 3364–8 (2013).

[194] A. Sanwaria, S.and Horechyy, D. Wolf, Ch.-Y Chu, H. L Chen, P. Formanek, M. Stamm, R. Srivastava, and B. Nandan, “Helical packing of nanoparticles confined in cylindrical domains of a self-assembled block copolymer structure”, *Angew Chem Int Ed Engl* (2014).

[195] G. D Scott and D. M Kilgour, “The density of random close packing of spheres”, *J Phys D Appl Phys* **2**, pp. 863 (1969).

[196] Mi. Tymczenko, L. F. Marsal, T. Trifonov, I. Rodriguez, F. Ramiro-Manzano, J. Pallares, A. Rodriguez, R.n Alcubilla, and F. Meseguer, “Colloidal crystal wires”, *Adv Mater* **20**(12), pp. 2315–2318 (2008).

[197] S. A Vanapalli, C. R Iacovella, K. E Sung, D. Mukhija, J. M Millunchick, M. A Burns, S. C Glotzer, and M. J Solomon, “Fluidic assembly and packing of microspheres in confined channels”, *Langmuir* **24**(7), pp. 3661–3670 (2008).

[198] A. N Khlobystov, D. A Britz, A. Ardavan, and G. A Briggs, “Observation of ordered phases of fullerenes in carbon nanotubes”, *Phys Rev Lett* **92**, pp. 245507 (2004).

[199] T. Y. Yin and Y. Xia, “Self-assembly of spherical colloids into helical chains with well-controlled handedness”, *J Am Chem Soc* **125**(8), pp. 2048–9 (2003).

[200] S. H Glarum, "Dielectric relaxation of isoamyl bromide", *J Chem Phys* **33**, pp. 639 (1960).

[201] P. Bordewijk, "Defect-diffusion models of dielectric relaxation", *Chem Phys Lett* **32**(3), pp. 592 – 596 (1975).

[202] J. T Bendler and M. F Shlesinger, "Defect-diffusion models of relaxation", *J Mol Liq* **36**(0), pp. 37 – 46 (1987).

[203] H. Tanaka, "General view of a liquid-liquid phase transition", *Physical review. E, Statistical physics, plasmas, fluids, and related interdisciplinary topics* **62**(5), pp. 6968–6976 (2000).

[204] M. Leocmach and H. Russo, J.and Tanaka, "Importance of many-body correlations in glass transition: an example from polydisperse hard spheres.", *J Chem Phys* **138**(12), pp. 12A536–12A536 (2013).

[205] A. Malins, J. Eggers, H. Tanaka, and C. P Royall, "Lifetimes and lengthscales of structural motifs in a model glassformer", *Faraday Discuss* **167**, pp. 405–423 (2013).

[206] C. P. Royall and S. R Williams, "The role of local structure in dynamical arrest", *arXiv.org* (2014).

[207] G. Biroli, Bouchaud J.-P, and G. Tarjus, "Are defect models consistent with the entropy and specific heat of glass formers?", *J Chem Phys* **123**(4), pp. 044510 (2005).

[208] L. Berthier and J. P Garrahan, "Real space origin of temperature crossovers in supercooled liquids", *Phys Rev E* **68**, pp. 41201 (2003).

[209] K. J Strandburg, "Two-dimensional melting", *Rev Mod Phys* **60**(1), pp. 161–207 (1988).

[210] U. Gasser, "Crystallization in three- and two-dimensional colloidal suspensions", *J Phys Condens Matter* **21**(20), pp. 203101 (2009).

[211] U. Gasser, C. Eisenmann, G. Maret, and P. Keim, "Melting of crystals in two dimensions", *Chemphyschem* **11**(5), pp. 963–970 (2010).

[212] K. Binder, S. Sengupta, and P. Nielaba, "The liquid-solid transition of hard discs: First-order transition or Kosterlitz-Thouless-Halperin-Nelson-Young scenario?", *J Phys Condens Matter* **14**(9), pp. 2323–2333 (2002).

[213] T. Terao and T. Nakayama, "Crystallization in quasi-two-dimensional colloidal systems at an air-water interface", *Phys Rev E* **60**, pp. 7157 (1999).

[214] Z. Wang, A. M Alsayed, A. G Yodh, and Y. Han, "Two-dimensional freezing criteria for crystallizing colloidal monolayers", *J Chem Phys* **132**, pp. 4501 (2010).

[215] C. A Weber, C. Bock, and E. Frey, "Defect-mediated phase transitions in active soft matter", *Phys Rev Lett* **112**, pp. 168301 (2014).

[216] W. Qi, A. P Gantapara, and M. Dijkstra, "Two-stage melting induced by dislocations and grain boundaries in monolayers of hard spheres", *Soft Matter* **10**(30), pp. 5449–57 (2014).

[217] S. Torquato and F. H Stillinger, "Jammed hard-particle packings: From kepler to bernal and beyond", *Rev Mod Phys* **82**, pp. 2633 (2010).

[218] B. J Alder and T. E Wainwright, "Studies in molecular dynamics. ii. behavior of a small number of elastic spheres", *J Chem Phys* **33**, pp. 1439 (1960).

[219] A. Donev, S. Torquato, and F. H Stillinger, "Pair correlation function characteristics of nearly jammed disordered and ordered hard-sphere packings", *Phys Rev E* **71**, pp. 011105 (2005).

[220] F. Ritort and P. Sollich, "Glassy dynamics of kinetically constrained models", *Adv Phys* **52**(4), pp. 219–342 (2003).

[221] D. R Nelson and B. I Halperin, "Dislocation-mediated melting in two dimensions", *Phys Rev B Condens Matter* **19**, pp. 2457 (1979).

[222] M. S. S Challa, D. P Landau, and K. Binder, "Finite-size effects at temperature-driven first-order transitions", *Phys Rev B Condens Matter* **34**, pp. 1841 (1986).

[223] K. Binder, "Finite size scaling analysis of ising model block distribution functions", *Zeitschrift für Physik B Condensed Matter* **43**, pp. 119 (1981).

[224] K. Binder, "Finite size effects at phase transitions", In H. Gausterer and C.B. Lang, editors, *Computational Methods in Field Theory* volume 409 of *Lecture Notes in Physics* , pp. 59–125. Springer Berlin Heidelberg (1992).

[225] K. J. Strandburg, J. A Zollweg, and G. V Chester, "Bond-angular order in two-dimensional lennard-jones and hard-disk systems", *Phys Rev B Condens Matter* **30**, pp. 2755 (1984).

[226] H. Weber, D. Marx, and K. Binder, "Melting transition in two dimensions: A finite-size scaling analysis of bond-orientational order in hard disks", *Phys Rev B Condens Matter* **51**, pp. 83510 (1995).

[227] H. Weber and D. Marx, "Two-dimensional melting approached via finite-size scaling of bond-orientational order", *Europhys Lett* **27**, pp. 593 (1994).

[228] R. Zangi and S. A Rice, "Phase transitions in a quasi-two-dimensional system", *Phys Rev E* **58**, pp. 7529 (1998).

[229] W.-K Qi, Z. Wang, Y. Han, and Y. Chen, "Melting in two-dimensional yukawa systems: A brownian dynamics simulation", *J Chem Phys* **133**, pp. 4508 (2010).

[230] Y. Han, N. Y Ha, A. M Alsayed, and A. G Yodh, "Melting of two-dimensional tunable-diameter colloidal crystals", *Phys Rev E* **77**, pp. 41406 (2008).

[231] K. Binder and W. Kob, *Glassy Materials and Disordered Solids: An Introduction to Their Statistical Mechanics*, World Scientific (2011).

[232] M. Rovere, D. W Heermann, and K. Binder, "The gas-liquid transition of the two-dimensional lennard-jones fluid", *J Phys Condens Matter* **2**, pp. 7009 (1990).

[233] D. Marx, P. Nielaba, and K. Binder, "Path-integral monte carlo study of a model adsorbate with internal quantum states", *Phys Rev B Condens Matter* **47**, pp. 7788 (1993).

[234] D. Marx, P. Nielaba, and K. Binder, "Phase transitions in two-dimensional fluids with internal quantum states", *Phys Rev Lett* **67**, pp. 3124 (1991).

[235] M. Rovere, D. W Hermann, and K. Binder, "Block density distribution function analysis of two-dimensional lennard-jones fluids", *Europhys Lett* **6**, pp. 585 (1988).

[236] D. Vågberg, D. Valdez-Balderas, M. A Moore, P. Olsson, and S. Teitel, "Finite-size scaling at the jamming transition: Corrections to scaling and the correlation-length critical exponent", *Phys Rev E* **83**, pp. 30303 (2011).

[237] L. van Hove, "Sur L'intégrale de Configuration Pour Les Systèmes De Particules À Une Dimension", *Physica* **16**(2), pp. 137–143 (1950).

[238] L. D Landau and E. M Lifshitz, *Statistical physics*, Butterworth-Heinemann (1980).

[239] C. Kittel, "Theory of antiferroelectric crystals", *Phys Rev* **82**, pp. 729 (1951).

[240] T. L Hill, "Phase transition in a one-dimensional system", *Proc Natl Acad Sci USA* **57**(2), pp. 227–32 (1967).

[241] T. L Hill and G. M White, "Phase transition in a one-dimensional system, ii", *Proc Natl Acad Sci USA* **58**(2), pp. 454–61 (1967).

[242] F. J Dyson, "Existence of a phase-transition in a one-dimensional Ising ferromagnet", *Commun Math Phys* **12**(2), pp. 91–107 (1969).

[243] M. Fisher, Sh.-K Ma, and B. Nickel, "Critical Exponents for Long-Range Interactions", *Phys Rev Lett* **29**(14), pp. 917–920 (1972).

[244] R. Dickman and T. Tomé, "First-order phase transition in a one-dimensional nonequilibrium model", *Phys Rev A* **44**, pp. 4833 (1991).

[245] M. R Evans, "Phase Transitions in One-Dimensional Nonequilibrium Systems", *Braz J Phys* **30**(1), pp. 42–57 (2000).

[246] K. Uzelac and Z. Glumac, "The critical behaviour of the long-range Potts chain from the largest cluster probability distribution", *Physica A* **314**(1), pp. 448–453 (2002).

[247] I. L Aleiner, B. L Altshuler, and G. V Shlyapnikov, "A finite–temperature phase transition for disordered weakly interacting bosons in one dimension", *Nat Phys* **6**, pp. 900 (2010).

[248] A. Bar and D. Mukamel, "Mixed-order phase transition in a one-dimensional model", *Phys Rev Lett* **112**(1), pp. 015701 (2014).

[249] D. Frenkel and B. Smit, *Understanding Molecular Simulation: From Algorithms to Applications*, Computational science series. Elsevier Science (2001).

[250] D. G Levitt, "Dynamics of a single-file pore: Non-fickian behavior", *Phys Rev A* **8**, pp. 3050 (1973).

[251] Y. Rosenfeld, "Relation between the transport coefficients and the internal entropy of simple systems", *Phys Rev A Gen Phys* **15**, pp. 2545 (1977).

[252] Y. Rosenfeld, "A quasi-universal scaling law for atomic transport in simple fluids", *J Phys Condens Matter* **11**, pp. 5415 (1999).

[253] M. Dzugutov, "A universal scaling law for atomic diffusion in condensed matter", *Nature* **381**, pp. 137 (1996).

[254] J. L Bretonnet, "Self-diffusion coefficient of dense fluids from the pair correlation function", *J Chem Phys* **117**, pp. 9370 (2002).

[255] J. Mittal, J. R Errington, and T. M Truskett, "Quantitative link between single-particle dynamics and static structure of supercooled liquids", *J Phys Chem B* **110**(37), pp. 18147–18150 (2006).

[256] J. Mittal, J. R Errington, and T. M Truskett, "Thermodynamics predicts how confinement modifies the dynamics of the equilibrium hard-sphere fluid", *Phys Rev Lett* **96**, pp. 177804 (2006).

[257] J. Mittal, J. R Errington, and T. M Truskett, "Relationships between self-diffusivity, packing fraction, and excess entropy in simple bulk and confined fluids", *J Phys Chem B* **111**(34), pp. 10054–10063 (2007).

[258] R. Chopra, T. M Truskett, and J. R Errington, "On the use of excess entropy scaling to describe single-molecule and collective dynamic properties of hydrocarbon isomer fluids", *J Phys Chem B* **114**(49), pp. 16487–16493 (2010).

[259] J. R Errington, T. M Truskett, and J. Mittal, "Excess-entropy-based anomalies for a waterlike fluid", *J Chem Phys* **125**, pp. 4502 (2006).

[260] M.J Pond, J. R Errington, and T. M Truskett, "Communication: Generalizing rosenfeld's excess-entropy scaling to predict long-time diffusivity in dense fluids of brownian particles: From hard to ultrasoft interactions", *J Chem Phys* **134**, pp. 1101 (2011).

[261] J. Mittal, J. R Errington, and T. M Truskett, "Relationship between thermodynamics and dynamics of supercooled liquids", *J Chem Phys* **125**, pp. 6102 (2006).

[262] J. Mittal, J. R Errington, and T. M Truskett, "Does confining the hard-sphere fluid between hard walls change its average properties?", *J Chem Phys* **126**, pp. 4708 (2007).

[263] D. W Jepsen, "Dynamics of a simple many-body system of hard rods", *J Math Phys* **6**, pp. 405 (1965).

[264] A. Coniglio, A. Fierro, H.J. Herrmann, and M. Nicodem, editors, *Unifying Concepts in Granular Media and Glasses: From the Statistical Mechanics of Granular Media to the Theory of Jamming*, Elsevier, Amsterdam (2004).

[265] M. van Hecke, "Jamming of soft particles: geometry, mechanics, scaling and isostaticity", *J Phys-Condens Mat* **22**(3), pp. 033101 (2009).

[266] Th. K Haxton, M. Schmiedeberg, and A. J Liu, "Universal jamming phase diagram in the hard-sphere limit", *Phys Rev E* **83**(3), pp. – (2011).

[267] M. Mezard and A. Montanari, *Information, Physics, and Computation*, Oxford University Press, Inc. (2009).

[268] C. A. Rogers, *Packing and covering*, Cambridge University Press Cambridge (1964).

[269] A. S Keys, L.O Hedges, J. P Garrahan, S. C Glotzer, and D. Chandler, "Excitations are localized and relaxation is hierarchical in glass-forming liquids", *Phys. Rev. X* **1**, pp. 21013 (2011).

[270] D. M Sussman and K. S Schweizer, "Space-time correlated two-particle hopping in glassy fluids: Structural relaxation, irreversibility, decoupling, and facilitation", *Phys Rev E* **85**, pp. 61504 (2012).

[271] P. Charbonneau, J. Kurchan, G. Parisi, P. Urbani, and F. Zamponi, "Fractal free energy landscapes in structural glasses.", *Nat Commun* **5**, pp. 3725–3725 (2014).

[272] T. Aste, "Volume fluctuations and geometrical constraints in granular packs", *Phys Rev Lett* **96**, pp. 18002 (2006).

[273] S. Lang, Vi. Boţan, M. Oettel, D. Hajnal, Th. Franosch, and R. Schilling, "Glass transition in confined geometry.", *Phys Rev Lett* **105**(12), pp. 125701–125701 (2010).

[274] S. Mandal, S. Lang, M. Gross, M. Oettel, D. Raabe, Th. Franosch, and F. Varnik, "Multiple reentrant glass transitions in confined hard-sphere glasses", *Nat Commun* **5** (2014).